Semi- and Dileptonic Top Pair Decays
at the ATLAS Experiment

vorgelegt von

Raphael Mameghani

geboren in Neuss

Zusammenfassung

Der Large Hadron Collider, welcher 2008 in Betrieb gehen wird, lässt sich als "Top-Fabrik" bezeichnen, da Top-Antitop-Paare ($t\bar{t}$) mit einem Wirkungsquerschnitt von circa 830 pb bei einer instantanen Luminosität von $10^{33}\,\mathrm{cm}^{-2}\mathrm{s}^{-1}$ während des ersten Jahres produziert werden. Mit einer Wahrscheinlichkeit von etwa 30% zerfallen die Top-Paare semileptonisch in einen Endzustand mit vier Jets, einem Lepton (Elektron oder Myon) sowie zugehörigem Neutrino. Weitere 5% der $t\bar{t}$-Ereignisse zerfallen dileptonisch. Hierbei setzt sich die Signatur des Endzustandes aus zwei Jets, zwei Leptonen und zwei Neutrinos zusammen.

In der vorliegenden Arbeit wurde die Genauigkeit einer Messung des $t\bar{t}$-Wirkungsquerschnitts am ATLAS-Experiment sowohl im semileptonischen als auch im dileptonischen Kanal mittels schnittbasierter Analysen abgeschätzt, welche für die ersten gemessenen Daten optimiert wurden. Die Analyse im semileptonischen Kanal konzentrierte sich insbesondere auf Studien zum Untergrund durch QCD-Ereignisse mit Leptonen entweder aus semileptonischen Hadronzerfällen oder von Hadronen welche durch das Kalorimeter fälschlich als Elektronen rekonstruiert wurden. Für die ersten $10\,\mathrm{fb}^{-1}$ bei einer angenommenen Fehlidentifikations-Wahrscheinlichkeit von 10^{-3} lässt sich für den Wirkungsquerschnitt mal Verzeigungsverhältnis eine Genauigkeit von

$$\Delta\left(\sigma_{t\bar{t}}\cdot B(t\bar{t}\to bq\bar{q}'\,\bar{b}\ell\bar{\nu})\right) = \pm 0.5(\mathrm{stat}) \pm 30.4(\mathrm{syst}) \pm 24.0(\mathrm{lumi})\,\mathrm{pb}$$

abschätzen, was einer relativen Präzision von 16% für den aus der Theorie erwarteten Zentralwert von etwa 240 pb entspricht. Die Analyse im dileptonischen Kanal erreicht einen Messfehler von

$$\Delta\left(\sigma_{t\bar{t}}\cdot B(t\bar{t}\to b\bar{\ell}\nu\,\bar{b}\ell\bar{\nu})\right) = \pm 0.2(\mathrm{stat}) \pm 2.5(\mathrm{syst}) \pm 2.6(\mathrm{lumi})\,\mathrm{pb}$$

bzw. etwa 10% relative Genauigkeit für die Erwartung von 38 pb für den Wirkungsquerschnitt mal dem Verzeigungsverhältnis. Die Unsicherheiten im semileptonischen sowie im dileptonischen Kanal sollten sich im Zuge des Fortschritts, welcher für die Bestimmung der Luminosität und die Kenntnis der Untergründe durch Vergleiche mit gemessenen Daten erwartet wird, verbessern.

Eine Messung des Wirkungsquerschnitt-Verhältnisses zwischen dileptonischem und semileptonischem Kanal ist empfindlich auf Szenarien für neue Phänomene mit konkurrierenden Top-Zerfällen wie beispielsweise in ein geladenes Higgs-Boson. Es konnte abgeschätzt werden, dass ein solches Verhältnis mit einer Präzision von

$$\frac{\Delta R_{\ell\ell/\ell}}{R_{\ell\ell/\ell}} = \pm 0.7\%(\mathrm{stat}) \pm 7.7\%(\mathrm{sys}) \pm 3.1\%(\mathrm{lumi})$$

im ersten Jahr von ATLAS messbar sein sollte. Obwohl sich systematische Fehler in solch einem Verhältnis teilweise aufheben bleibt somit dennoch eine Gesamtunsicherheit von 8% bestehen, da die Untergründe nur aufgrund theoretischer Voraussagen abgeschätzt werden konnten. Auch dieses sollte sich verbessern, sobald Vergleiche mit gemessenen Daten möglich sind.

Abstract

The Large Hadron Collider, starting in 2008, will be a "top factory" as top-antitop ($t\bar{t}$) pairs will be produced with a cross section of about 830 pb at an instantaneous luminosity of $10^{33}\,\mathrm{cm}^{-2}\mathrm{s}^{-1}$ during the first year. With about 30% probability top pairs decay semileptonically into a final state with four jets, lepton (electron or muon) and respective neutrino. For another 5% of the $t\bar{t}$ events a dileptonic decay is expected. Here the final state signature is composed of two jets, two leptons and two neutrinos.

In this thesis the precision for a $t\bar{t}$ cross section measurement at the ATLAS experiment in the semileptonic and dileptonic channels with cut based analyses, applicable to the first data, was estimated. The analysis of the semileptonic decay focused especially on the study of background from QCD events either with leptons from semileptonic hadron decays or from hadrons falsely identified as electrons by the calorimeter. For the first $10\,\mathrm{fb}^{-1}$ and assuming a fake electron probability of 10^{-3} a precision for the cross section times the branching ratio of

$$\Delta\left(\sigma_{t\bar{t}} \cdot B(t\bar{t} \to bq\bar{q}'\,\bar{b}\ell\bar{\nu})\right) = \pm 0.5(\text{stat}) \pm 30.4(\text{syst}) \pm 24.0(\text{lumi})\,\mathrm{pb}$$

has been estimated, corresponding to a relative precision of 16% for the theoretically predicted cross section times branching ratio of about 240 pb. The analysis in the dileptonic channel achieves a precision of

$$\Delta\left(\sigma_{t\bar{t}} \cdot B(t\bar{t} \to b\bar{\ell}\nu\,\bar{b}\ell\bar{\nu})\right) = \pm 0.2(\text{stat}) \pm 2.5(\text{syst}) \pm 2.6(\text{lumi})\,\mathrm{pb}$$

which translates into a relative error of 10% for the cross section times branching ratio of around 38 pb. The errors for both the semileptonic and the dileptonic channel are expected to improve as progress is made on the luminosity determination and the knowledge of the backgrounds from comparisons with measured data.

A measurement of the cross-section ratio between the dileptonic and semileptonic channel is sensitive to scenarios of new phenomena with competitive top quark decay modes such as decays involving a charged Higgs boson. It has been estimated that such a ratio should be measurable with a relative precision of

$$\frac{\Delta R_{\ell\ell/\ell}}{R_{\ell\ell/\ell}} = \pm 0.7\%(\text{stat}) \pm 7.7\%(\text{sys}) \pm 3.1\%(\text{lumi})$$

during the first year of ATLAS data-taking. Even though the systematic errors partially cancel in such a ratio the total uncertainty is still around 8% as the background estimates rely on theoretical predictions. This should also improve as soon as the models can be tested against measured data.

Contents

Part I

Top Physics with ATLAS at the Large Hadron Collider

Chapter 1

Introduction

Elementary particle physics is the science investigating the basic constituents of matter and their interactions. Besides experiments with cosmic rays, particle accelerators emerged as the tool par excellence to discover and create new components of matter, allowing for detailed studies of their properties and interplay. The next experiment following a line of famous predecessors will be the Large Hadron Collider at CERN near Geneva where proton-proton collisions are scheduled to start before the end of 2008. With a centre-of-mass energy of 14 TeV and a final instantaneous luminosity of $10^{34}\,\mathrm{cm}^{-2}\mathrm{s}^{-1}$ the achievements of the LHC will outshine those of other experiments and the gate to particles at the TeV scale, as predicted for a large range of supersymmetric scenarios, will be opened.

But before setting off for new horizons the measurements of the previous experiments have to be repeated and the theoretical extrapolations to the LHC collision energies must be confirmed and determined as precisely as possible. Eventually all these Standard Model events are the haystack to be looked at for the needles of new physics. A background of particular interest will be events involving top quarks whose decay products are highly energetic and hence difficult to disentangle from signs of new physics. A precise knowledge of the number of top quark events and the topology of the decay products will be crucial for many future analyses.

The measurement of top quark properties is a worthwhile aim, because not all properties could be resolved definitively at the Tevatron, which was until now the only collider where the top quark could be created. As about eight million top pairs are expected to be produced during the first nominal year of the LHC at each collision point, making it a top factory, precise measurements will be hoped for.

This thesis treats the determination of the top pair production cross section for two different decay modes, semileptonic and dileptonic decays, by means of robust, cut based analyses. For the prediction to be as realistic as possible at the moment the full ATLAS detector simulation was used as far as feasible.

According to the Standard Model semileptonic decays should occur about six times more often than dileptonic events. A measured deviation from this expectation would be a sign of unknown processes, as explained in the last chapter of this thesis where the precision for such a ratio measurement is estimated.

1.1   Conventions

Throughout this thesis so-called "natural units" will be used, i.e.

$$\hbar \equiv 1 \qquad \text{and} \qquad c \equiv 1 \tag{1.1}$$

In addition charges will be given as multiple of the absolute value of the electron charge.

Furthermore the term cross section does not necessarily refer to the original cross section but may also include the branching ratio of a certain decay mode or include phase space limitations.

Chapter 2

Top Physics at Proton-Proton Colliders

2.1 The Standard Model of Particle Physics

The so-called Standard Model of particle physics describes the observed elementary particles and all their fundamental interactions except gravity. In this picture matter is composed of spin $1/2$ particles named fermions and the interactions are mediated by spin one field quanta, so-called bosons.

2.1.1 Fermions

Fermions as spin $1/2$ particles obey Pauli's exclusion principle and therefore have matter qualities. The Standard Model knows twelve such fundamental fermions plus their antiparticles. Six of the fermions are known as quarks (up, down, strange, charm, bottom and top) and are subject to both the electroweak and strong interaction. The remaining six fermions are referred to as leptons (electron, muon, tau and respective neutrinos). Leptons, in contrast to quarks, undergo only the electroweak interaction. In the electroweak theory quarks as well as leptons are arranged in three pairs, also called generations or families (see Table 2.1). Only the fermions of the first family are stable and can be found in ordinary atoms – up and down quarks compose the nucleons and the electrons fill the shell. Particles of the other two generations with their higher masses are unstable but can be produced for a short time in highly energetic particle collisions.

2.1.2 Bosons

So-called gauge bosons as spin one particles are the field quanta of the fundamental interactions. As such particles they couple to fermions carrying the relevant charge or quantum number and serve as mediator particles. Due to the local gauge invariance of the fields involved the corresponding quantum numbers are conserved according to Noether's theorem. In total the gauge fields of the Standard Model have a $\mathrm{U}(1) \otimes \mathrm{SU}(2) \otimes \mathrm{SU}(3)$ symmetry.

Table 2.2 summarises the Standard Model: four different kinds of gauge bosons have been observed. The photon is responsible for the electromagnetic force between charged particles. It is massless, the force has an infinite range and is described by quantum electrodynamics. The vector bosons $W^{\pm}$ and Z transmit the weak interaction. The reach of this force is limited due to the

Quarks						
Generation	**Flavour**	**Symbol**	**Charge [e]**	**Mass [GeV]**		
1	up	u	$+ 2/3$	0.00225	$\pm$	0.00075
	down	d	$- 1/3$	0.005	$\pm$	0.002
2	charm	c	$+ 2/3$	1.25	$\pm$	0.09
	strange	s	$- 1/3$	0.095	$\pm$	0.025
3	top	t	$+ 2/3$	174.2	$\pm$	3.3
	bottom	b	$- 1/3$	4.2	$\pm$	0.07

Leptons				
Generation	**Lepton**	**Symbol**	**Charge [e]**	**Mass [GeV]**
1	electron	e	-1	$511 \cdot 10^{-6}$
	electron neutrino	ν_e	0	$< 2.2 \cdot 10^{-9}$
2	muon	μ	-1	$105.7 \cdot 10^{-3}$
	muon neutrino	ν_μ	0	$< 170 \cdot 10^{-6}$
3	tau	τ	-1	1.777
	tau neutrino	ν_τ	0	$< 15.5 \cdot 10^{-3}$

Table 2.1: The three generations of quarks and leptons in the Standard Model. Only the first generation is stable and constitutes ordinary matter. The masses are taken from [1].

	Electromagnetism	**Weak Force**	**Strong Force**
Range [m]	∞	$\ll 10^{-16}$	$10^{-15} - 10^{-16}$
Strength	$1/137$	$1.02 \cdot 10^{-5}$	≈ 1
Affected Particles	charged particles	all fermions	quarks
Gauge Boson	photon (γ)	vector bosons ($W^\pm$ & Z)	gluon (g)
Mass [GeV]	0	$\approx 10^2$	0

Table 2.2: Properties of elementary forces and respective mediating gauge bosons in the Standard Model.

non-zero masses of the vector bosons. The weak interaction involving the $W^\pm$ bosons acts on weak isospin doublets of left-handed fermions. Furthermore the $W^\pm$ is electrically charged and hence couples to the photon, too. The electrically neutral Z boson couples to both left- and right-handed particles. In a unified theory all three gauge bosons together with the photon can be combined to a single electroweak force.

Gluons, the remaining gauge bosons, couple to particles with a quantum number called colour charge and mediate the strong interaction between quarks. In spite of being massless gluons cover a short range only. This is comprehensible given that gluons carry an effective colour charge themselves and interact with each other directly. The theory of colour charge interaction is referred to as quantum chromodynamics (see Section 2.2).

In Figure 2.1 the fundamental fermion-boson interactions are illustrated by means of Feynman
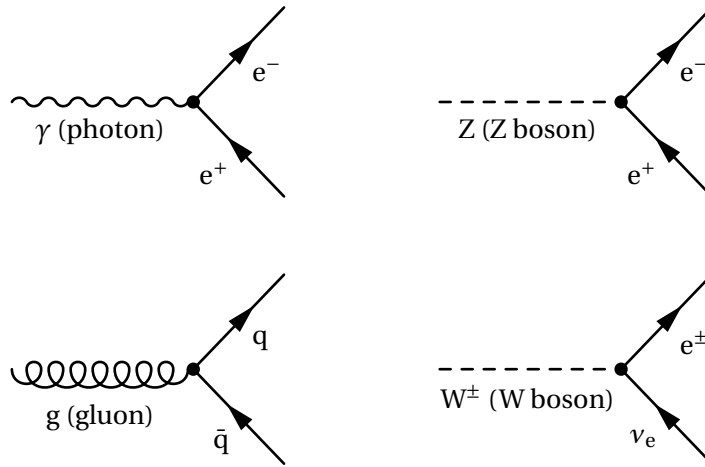
Figure 2.1: Feynman diagrams of the fundamental fermion-boson couplings in perturbation theory.

diagrams – the standard visualisation for perturbative calculations of particle reactions. These show interaction vertices of particles in a space-time coordinate frame (space axis vertical).

2.1.3 The Higgs Boson

Massive gauge bosons, as observed in collision experiments, contradict the principle of gauge invariance[1], the fundamental concept of gauge theories. A possible but experimentally still unconfirmed solution for this problem is the Higgs mechanism [2] which postulates an additional symmetry breaking background field with its Higgs boson coupling to the W and Z bosons causing an effective mass. Assuming Yukawa couplings the Higgs bosons could also explain the fermion masses. As no Higgs particle has yet been observed in experiments it must obtain a high mass from its self-coupling. The current lower limit for the Higgs particle mass is $114.4\,\text{GeV}$ [1].

2.2 Quantum Chromodynamics

Quantum chromodynamics, usually abbreviated as QCD, is the quantum field theory of the strong interaction, involving quarks and gluons. In QCD there are three kinds (plus anti-kinds) of a charge called colour which is carried by quarks and in colour anti-colour pairs by gluons. Experimental evidence for the existence of colour charges can be deduced e.g. from the cross section ratio for $e^+e^- \rightarrow$ hadrons versus $e^+e^- \rightarrow \mu^+\mu^-$.

In QCD Dirac's equation has to be invariant under local SU(3) colour transformations. This invariance is yielded by a gluon field whose quanta – the gluons – carry both colour and anti-colour. The $3 \otimes \bar{3}$ combinations split into a colour octet plus a singlet. Only the octet

$$r\bar{g}, r\bar{b}, g\bar{b}, g\bar{r}, b\bar{r}, b\bar{g}, \sqrt{\frac{1}{2}}(r\bar{r} - g\bar{g}), \sqrt{\frac{1}{6}}(r\bar{r} + g\bar{g} - 2b\bar{b})$$

---

[1] Gauge invariance is the invariance of the gauge field under a local phase transformation e.g. $\phi(x) \rightarrow e^{i\theta(x)}\phi(x)$.
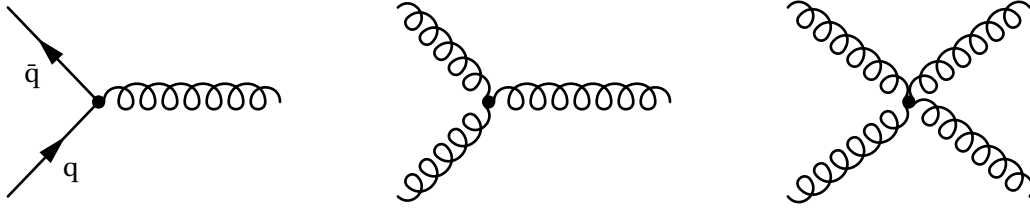
Figure 2.2: Feynman diagrams of the three fundamental gluon couplings in QCD: the quark gluon vertex and the 3 and 4 gluon interactions.
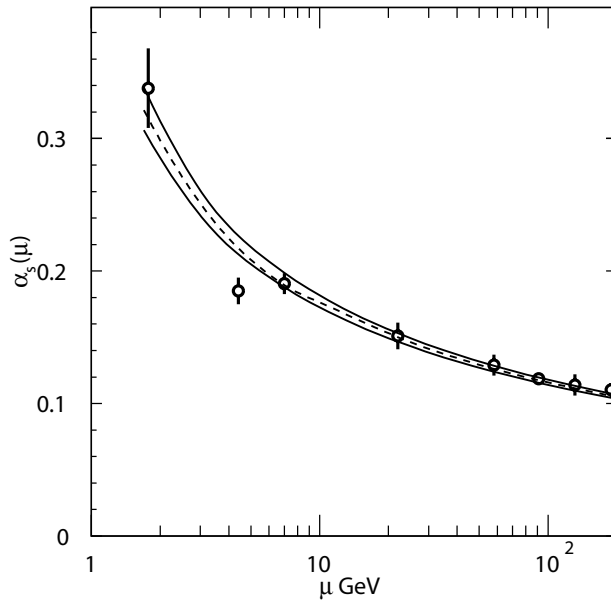
Figure 2.3: Measurement of the strong coupling α_S as a function of the energy scale μ. The band indicates the 1σ confidence level [1].

is a physical solution as the singlet

$$\sqrt{\frac{1}{3}}\,(r\bar{r} + g\bar{g} + b\bar{b})$$

would be colour neutral.

2.2.1 Running Coupling

As carriers of colour charge, gluons interact among each other. Figure 2.2 presents the three fundamental vertices of QCD. Because of the self-coupling of the gluons the effective coupling α_S of QCD approaches zero for increasing momentum transfers, a regime of asymptotic freedom where quarks are quasi-free particles. This renders perturbation calculations, as in QED, possible. On the opposite side α_S increases for decreasing momentum transfers, a phenomenon called confinement as it forbids the observation of free quarks. Figure 2.3 illustrates the running of $\alpha_S(Q)$ as a function of the energy scale Q. At the Z mass, the standard scale value, α_S is 0.1176 ± 0.002 [1].

2.2.2 Hadronisation

Colour confinement ensures that quarks are not observable as free particles. Instead they appear as partons within hadrons, i.e. bound states of quarks which are colour neutral. The transformation of single quarks from the scattering process into final hadrons is called hadronisation (see Figure 2.4). During this process quark anti-quark pairs are created from the gluon field between the original quarks until all quarks are bound into mesons (quark anti-quark states) and baryons (three quark states). In this way an energetic quark, e.g. from proton-proton collisions as described in Section 2.3, produces a bundle of hadrons, a so-called particle jet. The same mechanism causes jets from gluons, too.

As the hadronisation involves long distances, small momenta transfers occur. In this regime a description by means of perturbative QCD is impracticable and has to be replaced by phenomenological models. One approach is the Lund string fragmentation model as implemented in the PYTHIA simulation program [3] (see also Section 2.4): this approach assumes the creation of bands or strings of colour field lines between the departing quarks. Whenever the field energy inside such a string is large enough to create a real quark anti-quark pair the string breaks and the process starts over until the field energies drop below the quark production threshold and all quarks are bound. An alternative model based on quark gluon clusters can be found in [4]. Common to all hadronisation models is the need for tuning parameters which have to be chosen to obtain a good agreement with experimental data.

2.3 Proton-Proton Collisions

In proton-proton collisions particles are produced from parton interactions. At high energies the internal structure of the proton determines the momentum transfer during the hard scattering process. Typically the colliding partons carry only a fraction[2] of the collision energy as the proton consists not only of three valence quarks but also of gluons from the interconnecting colour field and sea quarks which are quarks and anti-quarks produced by vacuum fluctuations. Quantitatively the momentum distribution or structure function of the proton is described by the formula

$$F(x) = \sum_i e_i^2 \, x \, f_i(x, Q^2) \tag{2.1}$$

where x is the fraction of the total proton momentum carried by a parton, e is the charge of the parton, and $f_i(x, Q^2)$ represents the probability of the i-th parton to carry the momentum fraction x at the energy scale Q^2. Usually $f_i(x)$ is referred to as the parton density function, abbreviated as PDF. Because of the non-perturbative QCD involved, the PDFs cannot be calculated but can only be measured. Figure 2.5 shows the density functions of different partons for $Q = 2\,\mathrm{GeV}$ and $100\,\mathrm{GeV}$. The PDFs can be translated to other scales of Q^2 according to the DGLAP evolution equations [5].

The total cross section for a $p_A, p_B \rightarrow p_1, p_2$ reaction in a proton-proton scattering process, as illustrated in Figure 2.6, is given by the sum over all parton combinations of the individual cross sections folded with the proton PDFs:

---

[2]About 1/10 at the Large Hadron Collider with 14 TeV centre-of-mass energy.
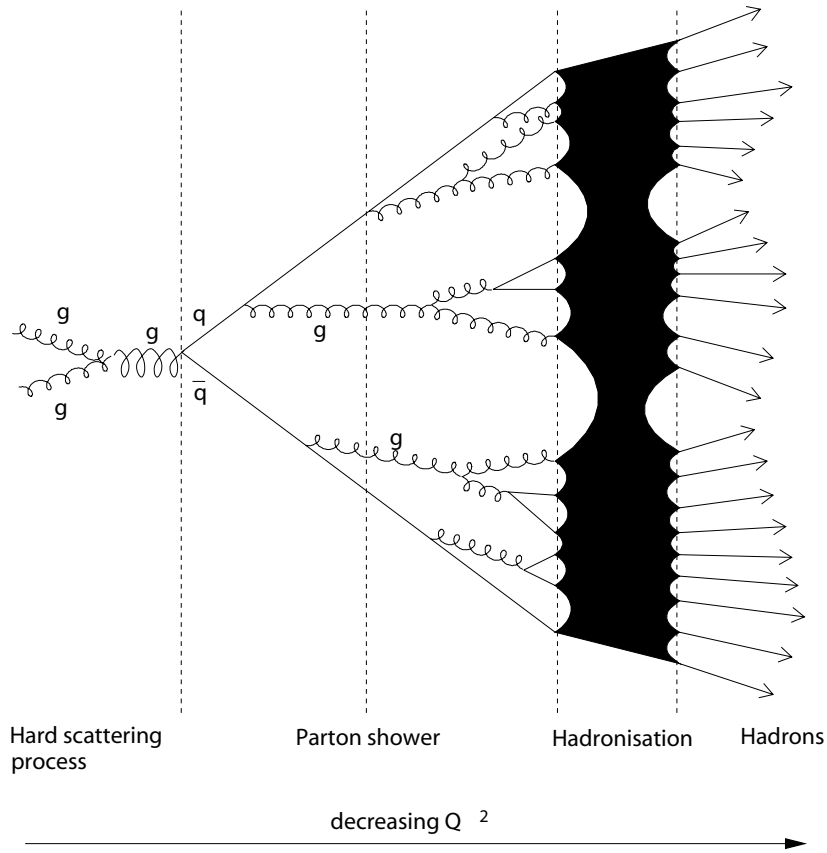
Figure 2.4: The process of hadronisation transforms quarks and gluons into colour-neutral hadrons.

$$\sigma_{\text{tot}} = \sum_{A,B} \int dx_A dx_B f_A(x_A, Q^2) f_B(x_B, Q^2) \, \sigma_{AB \to 12} \tag{2.2}$$

2.4 Monte Carlo Generators

As quantum field theories describe particle collisions by means of probabilities it is obvious to use stochastically simulated events representing such collisions for physics studies. In these simulations, Monte Carlo generators are used to calculate the theoretical wave function of a physics process, such as a particle collision, production and decay chain, and translate the wave function into a measureable event via random number generators [7]. Monte Carlo generators are an important tool in particle physics as measured data must be compared with theoretical predictions. Such simulations are performed for known physics processes in order to obtain a better

understanding of the detector and future background processes and also to predict scenarios of new physics, both together allowing for development and optimisation of analyses. Especially at the present stage of LHC experiments such as ATLAS, where no real data are taken, Monte Carlo simulations are the tool of choice to estimate the potential performance of the experiment.

To simulate collisions for the LHC, Monte Carlo generators need the PDFs of the colliding hadrons, the scattering matrix elements as well as a description of the parton showers and the hadronisation as outlined before. Since the scattering matrix can include different orders of the series expansion and other approximations as well as differing hadronisation models the predictions partially depend on the choice of the event generator. The main generators used in this thesis are:

- PYTHIA [3], a general purpose generator suitable (not only) for proton-proton collisions. It is based on leading order (LO) matrix elements, parton showers and uses the Lund string fragmentation as described before. In spite of the lack of next-to-leading order (NLO) corrections PYTHIA is commonly used because it covers a broad spectrum of physics processes (including supersymmetric or more exotic models) and due to its sophisticated hadronisation scheme.

- HERWIG [4], another multi-purpose event generator which resembles PYTHIA in many points. The major difference is the hadronisation model, which is based on clusters instead of colour strings.

- MC@NLO [8], which includes next-to-leading order matrix elements for the scattering process. As this generator only covers the hard interaction it has to be interfaced to a general purpose generator such as PYTHIA or HERWIG to add parton shower and hadronisation processes.

- ALPGEN [9], an event generator especially suited for events with large jet multiplicities in hadronic collisions. Again, the hard interaction must be supplemented by hadronisation provided by a general purpose generator.
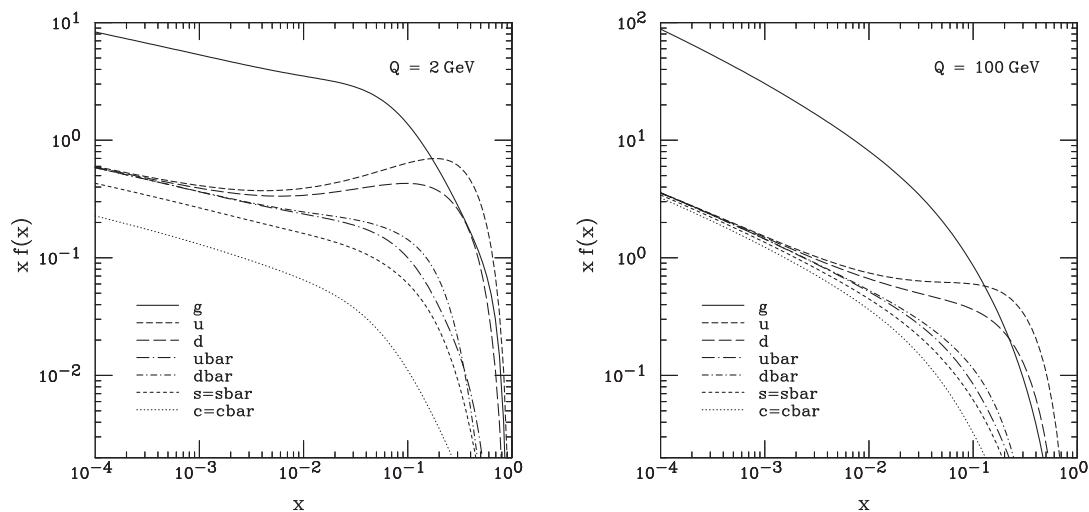
Figure 2.5: The CTEQ6M parton distribution functions for different partons at $Q = 2$ and $100\,\text{GeV}$ [6].
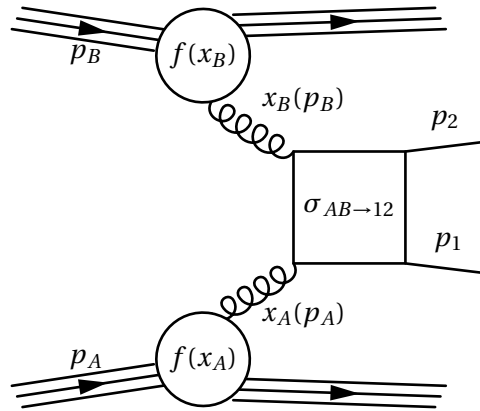
Figure 2.6: Illustration of the proton-proton scattering process.

2.5 Top Quarks

After the discovery of the bottom quark in 1977 [10] the existence of the top quark as the associated weak isospin partner was hypothesised. Later, precision measurements of the electroweak vector boson masses at CERN provided constraints on the top mass [11]. Finally, in 1995 the top quark has been confirmed via direct measurements performed by the CDF and D0 experiments at Fermilab [12, 13]. Reason for the late discovery is the originally unexpected high top mass of slightly above $170\,\text{GeV}$ – which is almost 20 times higher than the b-quark mass and establishes the top as the most massive known elementary particle. As an up-type quark the top carries a charge of $+\,2/3\,$e and a weak isospin of $+\,1/2$.

2.5.1 Top Quark Production

At hadron colliders like the LHC, which will be described in Section 3.1, top quarks are produced in pairs either via gluon fusion or quark anti-quark annihilation, as visualised by the Feynman diagrams in Figure 2.7. At the Tevatron, where protons and anti-protons collide, the annihilation is the main production mechanism. But at the LHC, as a proton-proton machine with a higher collision energy, anti-quarks only appear in fluctuations, which reduces the role of the annihilation process. In addition, at the LHC collision energy more momentum is carried by gluons due to the PDFs. It is expected that at the LHC about 87% of the top pairs will be produced via gluon fusion and consequently quark anti-quark annihilation contributes a mere 13%. At the LHC the overall production cross section in next-to-leading order is estimated to yield [14]

$$\sigma(\text{pp} \to \text{t}\bar{\text{t}}) \approx 830\,\text{pb} \tag{2.3}$$

Even though top quarks are preferentially produced in pairs via the strong interaction, the single top production via the weak force also takes place: in this case a lone top quark is produced by $\text{W}^{\pm}$ exchange, e.g. $\text{q}\bar{\text{q}}' \to \text{W}^+ \to \text{t}\bar{\text{b}}$.

2.5.2 Top Quark Decays

Because of its high mass the top quark has an extremely short lifetime of [1]
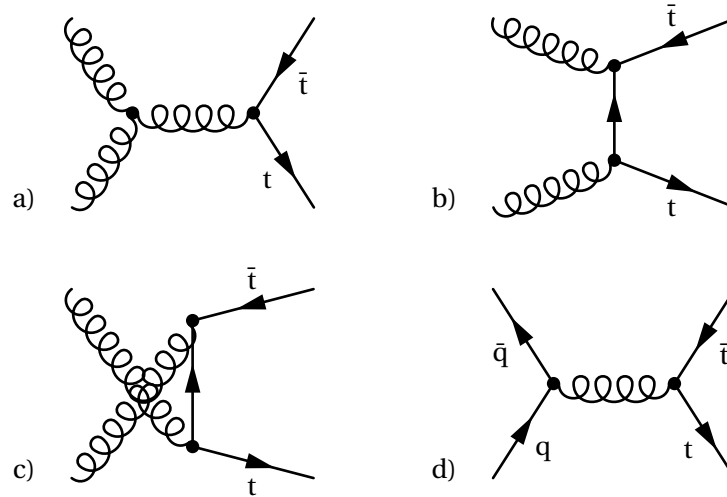
Figure 2.7: Top anti-top pairs can be created either via gluon fusion (diagrams (a) − (c)) or quark anti-quark annihilation (diagram (d)).

Figure 2.8: Combinatorics of the top pair decays.

$$\tau_{\text{top}} \approx 10^{-24}\,\text{s} \qquad\qquad (2.4)$$

No hadronisation occurs for this quark as the creation of bound states would need about 10^{-23} s. As a consequence top quark properties are inherited by its decay products allowing for direct experimental access to the underlying physics.

According to Standard Model constraints the top quark decays essentially into a bottom quark plus W boson only. In a second step the W boson decays either into a quark anti-quark pair with about 2/3 probability or into a charged lepton neutrino pair with the remaining chance of 1/3. Using combinatorics this leads to the following decay categories for top pair decays (see Figure 2.8) with the Feynman diagrams shown in Figure 2.9:

- All-hadronic decays: with 44.4% probability this decay channel is the most frequent one for top pairs. Here in a first step $t\bar{t}$ decays into $W^+b\,W^-\bar{b}$ and in a second step both W bosons
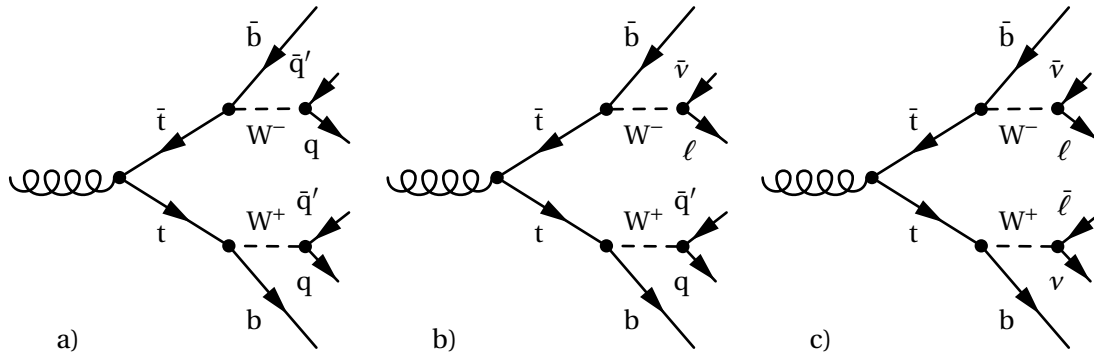
Figure 2.9: Top anti-top pair decays. (a) All-hadronic decay with six quarks resp. jets in the final state, (b) semileptonic decay into four jets, one charged lepton and one neutrino, (c) dileptonic decay into two jets, two oppositely charged leptons and two neutrinos.

decay into quark anti-quark pairs resulting in a six quark final state and accordingly a signature with six jets. Even though this channel has the largest branching ratio it is also the most difficult to observe due to a large QCD background from light quarks.

- Semileptonic decays: in this channel one of the W bosons decays into two jets while the other resolves into a lepton plus associated neutrino. Not considering τ leptons due to their complex consecutive decays this channel has a branching ratio of 29.6%. The semileptonic $t\bar{t}$ decay is the preferred channel for experimental investigation as it has a large cross section paired with a low background signature. Furthermore, because both hadronic and leptonic W boson decay products are present, a good handle on systematic uncertainties is available. The semileptonic channel is examined in detail in this thesis.

- Dileptonic decays: the ratio for both W bosons decaying into leptons plus neutrinos is merely 4.9%, again not counting the cases where τ leptons are produced. Despite the low decay probability this channel is still of major interest because of the low number of events from background processes giving two oppositely charged but not necessarily identically flavoured leptons at the same time plus momentum carried away by neutrinos. Thus, the dileptonic channel is also covered by this work.

- τ decays: the τ leptons decay quickly either into another charged lepton and neutrinos or hadrons plus a neutrino. Taus are hence easily confused with other particles. For this reason these decays require very sophisticated reconstruction and identification methods when analysing top pairs. In the following the τ decays will only be considered as a background to the other decay channels.

2.5.3   Continuing Importance of the Top Quark

Even though the top quark was discovered more than ten years ago and its mass has been measured to a precision of about 1% [15] there are still open questions: why is it the only fermion with a mass near the electroweak scale, is there something like top colour? If there is a Higgs boson, does the top really couple to it via the Yukawa mechanism and does the Higgs mass match to constraints from the top and W masses? Obviously there are good reasons to continue studying

the top quark at the LHC and not merely to use the top resonance for calibration purposes. Top quarks are also expected to contribute a major background in many scenarios for physics beyond the Standard Model such as Supersymmetry. Thus it is crucial to measure the $t\bar{t}$ production cross section and top quark decays precisely at the LHC. The capability of the ATLAS detector to do so during the first year of operation is estimated in Chapters 5 to 8. The open question as to whether the top really almost always decays into W + b is elaborated in Chapter 9 by considering prospects for a decay ratio measurement.

Chapter 3

The ATLAS Experiment

The typical set-up of collider experiments is comprised of three components: the particle accelerator, the detector and the data processing. This chapter gives a brief overview of the important points of the ATLAS experiment regarding the subsequent top physics studies.

3.1 The Large Hadron Collider

The Large Hadron Collider (LHC) at the European Organisation for Nuclear Research (CERN) close to Geneva is the successor to the Large Electron-Positron Collider (LEP). In the 27 km long ring tunnel, where electrons and positrons used to circulate and collide in the days of LEP (1989–2000), the LHC is scheduled to start operation in 2008. Because the collision energy at LEP of up to 209 GeV was limited by synchrotron radiation it became necessary to exchange the e^+e^- collider for a hadron collider. Since the power loss from synchrotron radiation is proportional to m^{-4}, where m is the mass of the circulating particles, the transition from electrons to protons renders this limitation obsolete. The price to be paid consists of the difficulties inherent in understanding the collisions of composite particles such as protons and the demanding detector technologies involved.

At the LHC two oppositely circulating proton beams will be caused to collide with 14 TeV centre-of-mass energy [16]. The restricting factor of the LHC will be the strength of the beam bending magnets although realised in superconducting technology. The LHC aims for a high instantaneous luminosity $\mathscr{L}$ of $10^{34}\,\mathrm{cm^{-2}s^{-1}}$ but will start running with one order of magnitude less during the first two operational years. To achieve the necessary collision rate the proton beams are collimated to thin bunches (15 μm radius), where each bunch is filled with 10^{11} protons. At design luminosity bunches cross every 25 ns and each bunch crossing produces on average 23 individual collisions.

The physics experiments CMS, ATLAS, LHC-B and ALICE are positioned at four intersection points, see Figure 3.1. CMS and ATLAS are universal detectors, designed to cover a broad range of scenarios for new and Standard Model physics. ATLAS is described in more detail in Section 3.2. From the two remaining experiments LHC-B specialises in measuring b-hadrons in order to investigate the parameters of CP violation while ALICE is a heavy ion experiment for a later phase of the LHC when lead nuclei instead of protons will be brought to collision.
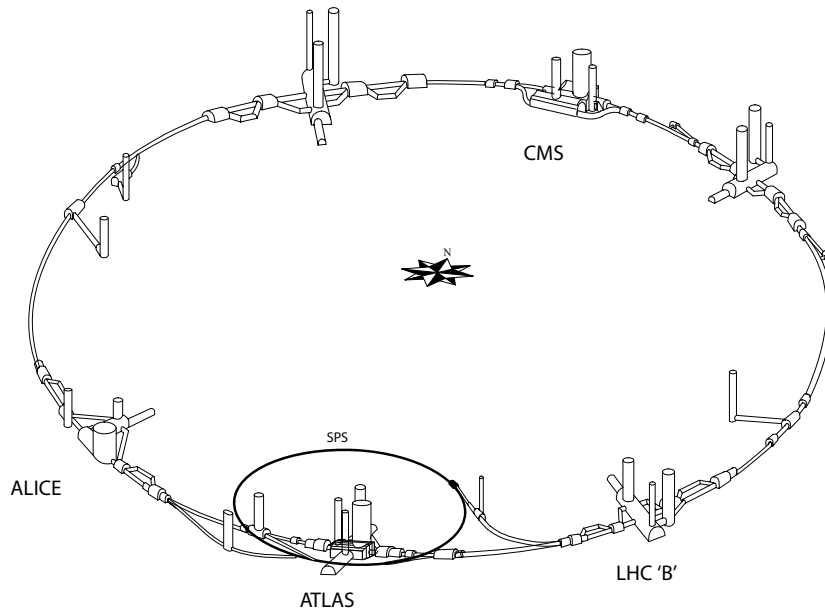
Figure 3.1: The Large Hadron Collider and the four intersection points with the ATLAS, CMS, ALICE and LHC-B detectors. For the LHC the existent Super Proton Synchrotron (SPS) serves as particle injector.

3.2 The Atlas Detector

ATLAS is a universal detector implementing the established symmetric cylindrical barrel layout with a concentric arrangement of subdetectors. It is 46 m long and 25 m in diameter with a weight of about 7000 t. From inside out ATLAS consists of an inner track detector, embedded into a solenoid magnet, an electromagnetic and hadronic calorimeter followed by a muon system inside a large toroidal air magnet. The sensitivity of a subsystem depends on the type of the traversing particle, allowing for its identification. The typical visibility characteristics are given in Table 3.1.

	ID	EC	HC	MS
Electron	✓	✓		
Muon	✓			✓
Charged Hadron	✓		✓	
Neutral Hadron			✓	
Photon		✓		
Neutrino				

Table 3.1: Sensitivity for different types of particles in the Inner Detector (ID), Electromagnetic Calorimeter (EC), Hadronic Calorimeter (HC) and the Muon Spectrometer (MS).

All subsystems of ATLAS can be divided into a barrel and two end cap regions. An illustration of the ATLAS detector is presented in Figure 3.2. For a recent in-depth compendium on the detector layout and the expected performance see [17, 18].
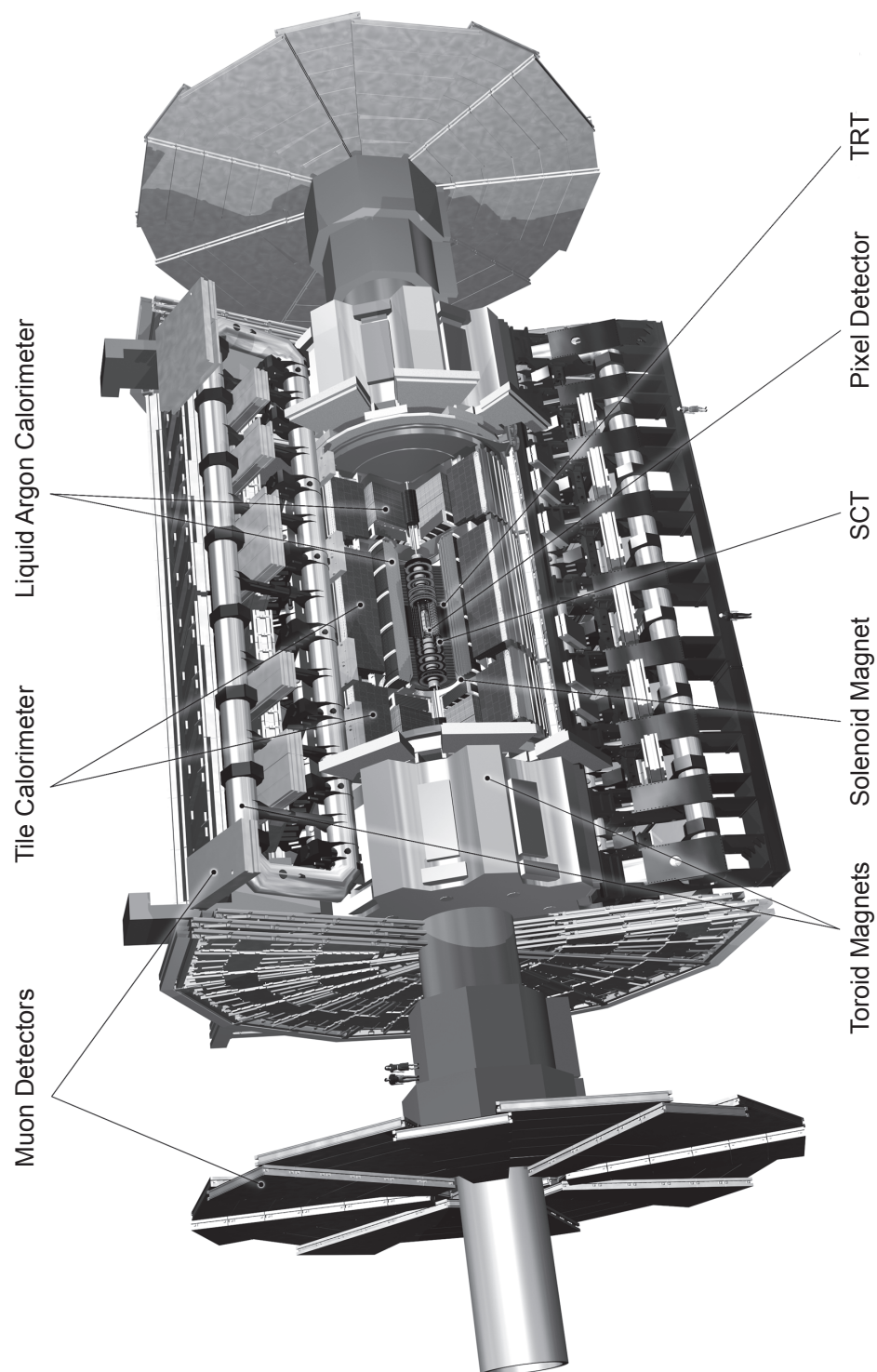
Figure 3.2: Composition of the ATLAS detector.

3.2.1   Coordinates

The shape of ATLAS favours the use of a cylindrical coordinate system with its origin at the centre of the detector where the collisions take place. In Cartesian coordinates the x-axis points toward the centre of the LHC ring, the y-axis upwards and the z-axis is defined by the beam direction in a right handed system. In cylindrical coordinates the azimuthal angle ϕ is measured about the beam axis and the polar angle θ is defined by $\tan\theta = {}^r\!/_z$ with $r^2 = x^2 + y^2$ as the distance to the z-axis. Usually not θ is used but the so-called pseudorapidity

$$\eta = -\log\left(\tan\frac{\theta}{2}\right) \tag{3.1}$$

which is in good approximation additive under Lorentz boosts along the beam direction. In terms of η the barrel region ranges from $0 \le |\eta| < 1.0$, the transition region from $1.0 \le |\eta| < 1.4$ and the end cap region from $1.4 \le |\eta| \le 2.7$.

A definition of the spatial distance between two physics objects in the η-ϕ-plane is given by

$$\Delta R \equiv \sqrt{(\Delta\eta)^2 + (\Delta\phi)^2} \tag{3.2}$$

For proton-proton collisions the initial momentum along the z-axis of the two interacting partons is unknown on a single event basis. Hence Lorentz invariant measures are used in order to be insensitive to any boost of the colliding partons along the z-direction. But since the x- and y-momentum components must each sum up to zero this constraint can be used when considering transverse quantities which are defined as projections onto the x-y-plane.

3.2.2   Inner Detector

The Inner Detector [19] ranges from near the beam axis to the enclosing solenoid magnet. It is subdivided into the silicon Pixel Detector, surrounded by the Semiconductor Tracker (SCT) with strip sensors followed by the Transition Radiation Tracker (TRT) which is implemented in gas detector technology. The Inner Detector is designed to precisely reconstruct tracks of charged particles allowing for a momentum measurement from the track curvature in the magnetic field. With the TRT a good separation of electrons from pions is possible. The geometric acceptance of the Inner Detector ranges up to $|\eta| = 2.5$.

3.2.3   Calorimetric System

The calorimeters [20] measure the particle energies and distinguish electrons, positrons, and photons from hadrons. The inner subsystem is the Electromagnetic Calorimeter (EC) which absorbs and detects electromagnetically showering particles – mainly electrons, positrons, and photons but in principle also muons and charged hadrons. The latter two lose a fraction of their energy in the EC only and reach the outer detector regions. The EC is a sampling calorimeter with consecutive layers of absorbing lead and liquid argon as active material. It ranges up to $|\eta| = 1.475$ for the barrel region and covers $1.4 \le |\eta| \le 3.2$ for the end cap. Parts of the Electromagnetic Calorimeter with massive structures before the sampling layers are preceded by additional pre-sampling detectors. The spatial granularity is $\Delta\eta \times \Delta\phi = 0.025 \times 0.025$ and the energy resolution for electromagnetic showers is roughly [20]

$$\frac{\Delta E}{E} = \frac{0.1}{\sqrt{E/\text{GeV}}} \oplus 0.01 \qquad\qquad (3.3)$$

The Hadronic Calorimeter (HC) follows the electromagnetic part and absorbs the bulk energy of both charged and neutral hadrons via hadronic showers caused by strong interactions with the absorbing material. Again a sampling technique is applied. The barrel of the HC ranges up to $|\eta| = 1.7$ and covers up to $|\eta| = 3.2$ for the end cap region. The intrinsic segmentation amounts to $\Delta\eta \times \Delta\phi = 0.1 \times 0.1$ for $|\eta| < 2.5$. Beyond that angle the granularity is coarser and reduced to $\Delta\eta \times \Delta\phi = 0.2 \times 0.2$. A parametrisation of the energy resolution is given by [20]

$$\frac{\Delta E}{E} = \frac{0.5}{\sqrt{E/\text{GeV}}} \oplus 0.03 \qquad\qquad (3.4)$$

In principle only muons (and neutrinos) can pass the calorimetric system. Nevertheless, thermalised neutrons and soft photons from calorimeter showers may still reach the inner parts of the muon system.

3.2.4 Muon Spectrometer

The Muon Spectrometer (MS) is the outermost subdetector of ATLAS [21]. It is designed to measure muons and their deflection in the on average 0.6 T field of the toroid magnet as precisely as possible. The Muon Spectrometer is supposed to measure muon momenta with a stand alone resolution comparable to the precision of the Inner Detector. For transverse momenta between 10 and 100 GeV 3% uncertainty and for muons at 1 TeV still 10% precision is expected [21].

In terms of technology the Muon Spectrometer comprises three layers of high precision Monitored Drift Tube Chambers (MDTs), in general combined with fast trigger detectors. In the very forward region Cathode Strip Chambers are also used. The high precision of the muon system would not be possible without the optical alignment systems.

3.2.5 Trigger and Data Acquisition

Due to the high collision rate of 40 MHz at ATLAS not all events can be recorded and stored. The event reconstruction system is able to handle an event rate of about 100 Hz. Hence ATLAS, just like other detectors, discriminates in advance between interesting physics processes and low energy background events by means of a trigger system [22]. This trigger consists of three discrimination steps as illustrated in Figure 3.3.

Level One (LVL1) is a hardware trigger which reduces the event rate from 40 MHz to 75 kHz. It separates interesting event candidates on the basis of coarse grained calorimeter information plus data from the fast muon trigger chambers. The LVL1 trigger also separates the event into regions of interest. In a pipeline stream the data from Level One are passed on to the second trigger layer.

Level Two (LVL2) is a software implemented trigger level. It has access to the event with full resolution for the regions of interest as well as for the whole inner detector. In this trigger layer the event rate is reduced to 1 kHz. The LVL2 data are buffered and handed on to the last trigger level.

The third trigger layer, called Event Filter (EF), makes the final decision whether an event is recorded or not, aiming for an event rate of 100 Hz. The EF is software based and runs on a computer
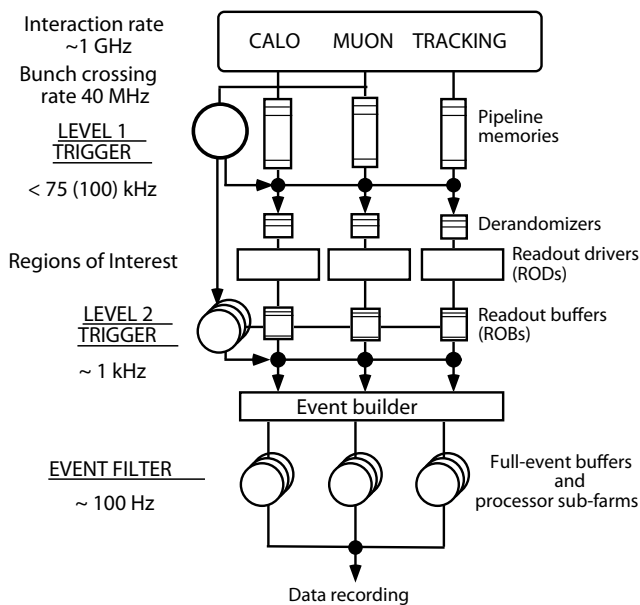
Figure 3.3: Layout of the ATLAS trigger system.

cluster close to the ATLAS detector. At this point the complete event is examined for the first time with the full granularity and decisions based on more complex analyses are made. Events accepted by the EF are written to storing devices and distributed to computer farms all over the world, as described in Section 3.3.1.

3.3   Data Analysis

The size and complexity of the ATLAS experiment is not limited just to the detector hardware but is also reflected in the analysis software and required computing infrastructure. At the design trigger rate of 100 Hz data of more than 1 PB are taken annually. The Grid, a network of computer clusters, is needed for the offline reconstruction of physics objects from the recorded events. ATHENA, the software framework used by the ATLAS collaboration, serves not only for event reconstruction but also for simulation and detector alignment purposes.

3.3.1   Grid Computing

The world-wide LHC computing grid is a network of hierarchically interconnected computing centres all over the world. Its structure is sketched in Figure 3.4: the Tier-0 is at CERN and will be responsible for the first processing and the subsequent distribution of the data. Next in the hierarchy are the Tier-1 centres for different regions of the world. These are responsible for further data processing, data storage and distribution. The smaller Tier-2 centres will be responsible for larger physics analyses, Monte Carlo productions and storing selected data samples whilst Tier-3 clusters are most suitable for smaller user analyses or local test jobs.

Only the Tier-0 at CERN is intended to have a full copy of all data sets while the other Tiers are only meant to keep fractions. Due to the large size of the stored data in a typical analysis job the user
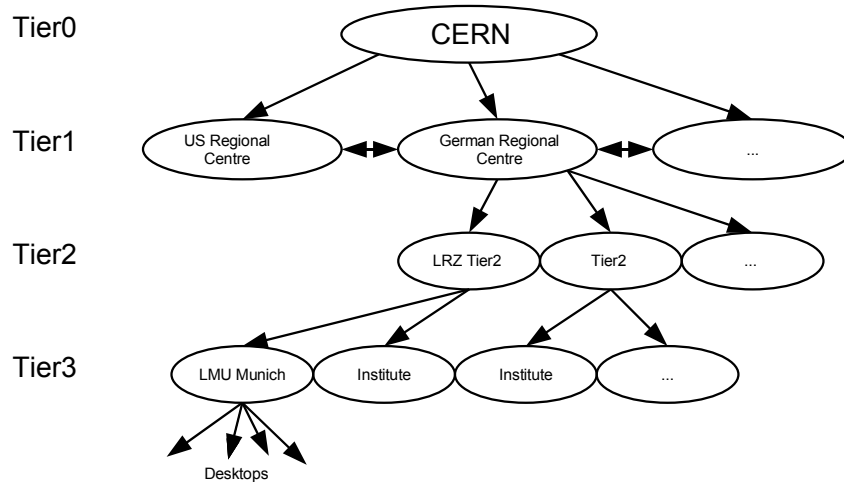
Figure 3.4: Structure of the High Energy Physics Grid.

analysis program will be transferred in the computing grid to the data (instead of the other way round) and the collected results will be returned to the user afterwards.

3.3.2 The Analysis Framework ATHENA

As the ATLAS specific adaptation of the GAUDI [23] framework for high energy physics experiments, ATHENA [24] provides access to physics objects abstracted from raw data such as four-momenta of leptons or jets. ATHENA is also used to simulate realistic detector responses for particle reactions as it provides interfaces to popular Monte Carlo generators calculating the scattering process and simulates the impact of the final state particles on the detector material via GEANT4 [25]. Furthermore ATHENA derives calibration and alignment parameters from statistical comparisons between the event reconstruction and the raw data.

ATHENA is object oriented software written mainly in the C++ language with parts realised in Fortran. It is designed to run on both the Grid and local machines or clusters. For higher flexibility ATHENA is controlled and configured by means of so-called job-option files written in the Python scripting language. By now widely used as job-options in the ATLAS community is a collection of ATHENA wrapping programs called EVENTVIEW [26] or, in the top physics specific variant, TOPVIEW [27]. The analyses in this thesis are all based on physics objects selected by TOPVIEW among the original candidates from ATHENA.

3.3.3 The Monte Carlo Simulation Chain

The simulation of Monte Carlo events involves several steps, see Figure 3.5. At the beginning particle interactions are created by means of Monte Carlo generators. The resulting data are stored in standard HepMC format. In the next step the passage of the generated particles through ATLAS and their interactions with detector material and the magnetic field are estimated using the GEANT4 package, which considers effects such as multiple scattering, energy loss, photon conversions and further particle decays. The interactions with sensitive detector material are stored as in the next step the digitisation calculates expected detector responses such as pulses or drift times from the GEANT4 hits. After this step the simulated events correspond to real detector measure-
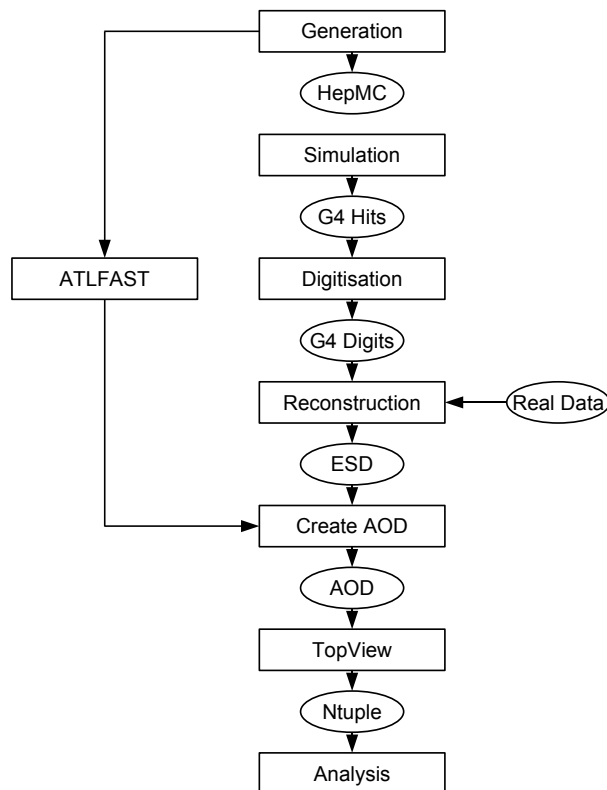
Figure 3.5: Full chain of the ATLAS Monte Carlo Simulation using the ATHENA framework.

ments.

In the following the reconstruction of particle tracks and calorimeter clusters is run, delivering the four-momenta of physics objects. Depending on the interaction characteristics the four-momenta are stored as candidates e.g. for electrons, muons or jets. These derived physics data are stored in both Event Summary Data (ESD) and Analysis Object Data (AOD) format. The first kind stores events in more detail and contains original calorimeter clusters and is intended for calibration studies or optimisation of jet reconstruction algorithms. The AOD format is reduced to objects of primary interest for physics analysis such as four-momenta, charges or reconstruction quality parameters.

User analyses are intended to be run on AOD files. But since the access to AODs is only possible within the ATHENA framework it is convenient to extract just the needed objects into a so-called ntuple file which can be accessed by stand alone software such as ROOT [28]. For this reason here TOPVIEW is run as the last pre-analysis step on the AODs. TOPVIEW not only dumps the relevant AOD objects to ntuples but also applies a preselection, removes reconstruction overlap and assigns the surviving objects to the Monte Carlo truth, which is kept through all the steps of the simulation chain.

Processing all the steps of the simulation chain takes 10 to 20 minutes per event on a current CPU. The effort to create the large number of events needed for the development of analyses is shared amongst the computing centres interconnected via the Grid. But even with this capacity it remains impossible to fully simulate all physics processes with the desired statistics.

3.3.4 Parametrised Simulation with ATLFAST

ATLFAST [29] is a parametrisation of the simulation, digitisation and reconstruction steps. Simplified, ATLFAST takes the 4-vectors from the Monte Carlo Generator and smears them according to the detector resolution as previously derived from fully simulated events. With this approach it is possible to reduce the computation time by many orders of magnitude. However, the resulting AODs do not contain objects stemming from the GEANT4 simulation of particle showers.

Chapter 4

Physics Objects and Preselection

From simulated or recorded data ATHENA reconstructs a variety of physics objects per event and stores them in AOD files. As raw detector patterns are not always unambiguous and can be interpreted in several ways, an overlap of reconstructed objects may occur. The preselection as performed by TOPVIEW removes this overlap in large part.

4.1 AOD Objects

In version 12.0.6 ATHENA stores, amongst other parameters, the 4-vectors of reconstructed photons, electrons, muons, τ leptons and calorimeter jets. For some of these objects, e.g. muons or jets, alternative reconstruction algorithms exist within ATHENA. Only the algorithms applied in the present analyses are described here.

4.1.1 Electrons

Characteristic for electrons is the track in the Inner Detector plus an electromagnetic shower in the calorimeter. To reconstruct electrons two algorithms are used [30]: one, particularly suitable for highly energetic electrons, considers sliding window clusters as reconstructed in the Electromagnetic Calorimeter and tries to match them to tracks from the Inner Detector. The other technique is seeded by preselected tracks in the Inner Detector, which are matched to calorimeter showers. Double counts from candidates reconstructed via both methods are removed in a subsequent step with priority placed on the first algorithm.

Reconstructed electrons can be classified into quality categories. Loose electrons are selected via cluster based criteria. Medium electrons must pass additional cuts on the track quality and the matching while tight electrons must also have a certain energy-momentum ratio plus a positive TRT decision. In ATHENA version 12.0.6 no reliable calorimeter isolation criterion can be used to further increase the quality of selected electrons.

4.1.2 Muons

For muon identification the STACO reconstruction algorithm [31, 32] is chosen. This algorithm statistically combines tracks from the Inner Detector with tracks reconstructed independently in

the Muon Spectrometer. The track selection is based on a χ^2 discriminant of the individual track parameters.

The inner track is identified by the xKalman algorithm which starts its reconstruction from the TRT and propagates track candidates inwards to the SCT and pixel layers, considering more and more hits. In the recent version xKalman is also able to seed its reconstruction in the SCT or pixel layers.

The track in the Muon Spectrometer is calculated by Muonboy [31]. Here regions of activity are identified and local tracks are reconstructed in the muon chambers. In a second step the local tracks are matched and finally spectrometer wide global fits are calculated.

4.1.3 Jets

The jets used in this thesis are reconstructed with the classical fixed cone jet algorithm built around seeds [33]. The jets are constructed using electromagnetic energy measurements delivered by the calorimeter towers and are calibrated via cell signal weights [34]. A split-merge tool assures non-overlapping exclusive jets in each event.

The cone algorithm forms jets by merging calorimeter towers lying within a radius R in the η-ϕ-plane. Starting from seeds with sufficient transverse energy $E_T = E \sin\theta$, the cone axis is moved to the centroid of the included calorimeter tower weights until a stable solution is reached, i.e. the centroid of the energy depositions within the cone is aligned with the geometric axis. The resulting 4-vector is composed of the vector of the cone axis and the total transverse energy within the cone.

In the following jets refer to cone jets of $R = 0.4$ with a seed E_T of at least 2 GeV. Only jets exceeding 10 GeV are stored in the AOD files.

B-Tagging

Jets stemming from bottom quarks can often be discriminated from light quark jets via so-called b-tagging. The lifetime of hadrons containing b-quarks suffices to travel a macroscopic distance of some millimetres before decaying. However, their lifetimes are not as high as those of light quark hadrons. Thus b-hadrons decay relatively close to, but not exactly at the point where the bottom quark was created. As b-quarks are far more massive than their decay products b-jets on average are wider and have more constituents than light quark jets. B-jets are also much more likely to contain leptons with substantial momentum perpendicular to the jet which are hence far from the jet axis, sometimes even outside the cone radius – an issue important later on in this thesis when considering fake leptons from QCD.

4.1.4 Missing Transverse Energy

Missing transverse energy ($\displaystyle{\not}E_T$) is a typical signature for events with neutrinos in the final state. Even though neutrinos escape detection they reveal themselves when the balance of transverse momentum is considered. The imbalance is calculated from the vector sum of transverse energy deposited in all calorimeter cells. The calorimeter calibrations for electromagnetic particles and jets are considered and a noise suppression is applied. Next a correction for the energy lost in the cryostat is applied and finally the contribution from muons passing beyond the calorimetric

system is added [35]. For this purpose the muon momentum measurement from Muonboy is used. The absolute value of the resulting corrected vector is used when referring to $\not{E}_T$ in the following.

4.1.5 Other Objects

In addition to the objects just described, two more classes are contained in the AODs. Photons are detected as electromagnetic calorimeter showers, just like electrons but without an inner track [36]. Photons are of minor importance for examinations of top pair production and are ignored here. Photons faking a calorimeter jet occur in the list of jets anyway.

The last category of physics objects reconstructed by ATHENA are tau leptons. Since tau particles decay quickly after their production only their decay products are observable. Hadronic tau decays, e.g. into some pions plus neutrino, resemble small jets and are difficult but possible to distinguish [37]. Especially during the initial data-taking period of ATLAS the reliability of the tau identification may not be trustworthy. In case of leptonic decays taus are detected as a lighter charged lepton plus missing transverse energy. When examining (semi)leptonic top decays into final states with leptons only from the first two generations, the tau decays contribute a substantial background. In case of semileptonic top pair decays a separation of $t\bar{t}$ events with hadronic τ lepton decays should be helpful but is not relied on here.

4.2 TopView Preselection

Not all objects in the AOD file are suitable candidates for top physics analyses. E.g. electrons of loose quality or jets just above the reconstruction threshold are unlikely to correspond to objects from the hard interaction. To eliminate the bulk fraction of these soft objects TOPVIEW [27] applies a number of preselection cuts on the reconstructed physics objects, following the recommendations by the ATLAS combined performance groups. TOPVIEW also removes the reconstruction overlap between electrons and jets.

4.2.1 Preselection Cuts

With TOPVIEW version 12.14 the following cuts have been implemented [38]: electrons must have a transverse energy of at least 10 GeV, $|\eta| < 2.5$, be of medium quality (as defined in Section 4.1.1) and have been reconstructed by the algorithm for highly energetic electrons. For muons a transverse energy exceeding 10 GeV and $|\eta| < 2.5$ is demanded as well as less than 6 GeV energy in a surrounding cone of $R = 0.2$. In addition only muons using the best match between the Muon System and the Inner Detector are taken. Jets are required merely a transverse energy larger than 15 GeV. They are considered as b-tagged for a likelihood of 7.05 or more, corresponding to a b-tag efficiency of 60% [39].

4.2.2 Overlap Removal

Electrons and jets are both reconstructed from objects in the calorimeter. Since jets can have an electromagnetic component showers in the Electromagnetic Calorimeter cannot unambiguously be reconstructed as electrons/photons or jets. For this reason ATHENA reconstructs these objects as both electrons and jets. As for a top pair analysis both the number of leptons and the number

of jets are relevant these double counts have to be removed. For this purpose TOPVIEW eliminates all jets reconstructed within a radius of $R = 0.3$ in the η-ϕ-plane around electron candidates [38] since it is less probable that a jet will be reconstructed as an electron than vice versa.

Part II

The Semileptonic Decay Channel

Chapter 5

Semileptonic Top Pair Analysis

5.1 Cross Section Measurement

In the early phase of ATLAS the measurement of the $t\bar{t}$ cross section should already be possible. For this purpose robust cut based analyses will be presented here, beginning with the semileptonic channel. The number of events observed after applying an analysis selection is given by

$$N = \varepsilon_{\text{s}} \cdot N_{\text{s}} + \varepsilon_{\text{b}} \cdot N_{\text{b}} = \varepsilon_{\text{s}} \cdot \sigma_{\text{s}} L + \varepsilon_{\text{b}} \cdot \sigma_{\text{b}} L \tag{5.1}$$

with the respective numbers of signal and background events, N_{s} and N_{b}, the selection efficiencies, ε_{s} and ε_{b}, the cross sections, σ_{s} and σ_{b}, and the integrated luminosity $L = \int \mathscr{L}\, dt$. For a signal cross section measurement the signal and background selection efficiencies have to be determined from Monte Carlo simulations, the background cross section has to be known as well as the integrated luminosity, measured e.g. on the basis of well understood processes as the elastic proton-proton scattering. To reduce the influence from uncertainties associated with the background cross section a selection with a small background efficiency paired with a good signal selection is required. More precisely, the cross section significance

$$\frac{\sigma}{\Delta\sigma} = \frac{N - B}{\sqrt{N + (\Delta B)^2}} \tag{5.2}$$

has to be maximised where $S = \varepsilon_{\text{s}} N_{\text{s}}$, $B = \varepsilon_{\text{b}} N_{\text{b}}$, and $N = S + B$. As the statistical errors on ε_{b} and N_{b} will be small when derived from Monte Carlo simulations, $(\Delta B)^2$ is negligible and the selection significance to be optimised is thus

$$\frac{\sigma}{\Delta\sigma} = \frac{S}{\sqrt{S + B}} \tag{5.3}$$

5.2 Signal and Backgrounds

For the cross section analysis Monte Carlo samples of the signal and relevant background processes are needed. In the following the centrally provided official ATLAS samples, namely all except the QCD background, taken for the analysis of dileptonic top pair decays are introduced, in-

Decay Type	Events	Cross Section [pb]
semileptonic	292 703	242.6
tau lepton(s)	207 480	168.9
dileptonic	48 327	38.3
undefined	40	

Table 5.1: The number of events (without considering weights) in the t̄t sample without all-hadronic decays, separated according to the decay type.

cluding the expected cross sections. Further details and references concerning the official datasets are collected in Appendix C.

5.2.1 The Top Anti-Top Sample

The t̄t signal was simulated with the Monte Carlo generator MC@NLO [8] interfaced to HERWIG for the parton showers. Here the next-to-leading order corrections in MC@NLO result in a fraction of $\approx 13\%$ of events with negative weight. The all-hadronic decays were excluded at the generator level. For this analysis the sample has been subdivided, based on the Monte Carlo truth information, into one selection containing only semileptonic t̄t decays and another one containing the dilepton and τ channels which will be considered as a background in the following. The predicted cross sections are $242.6^{+15.1}_{-11.3}$ pb for the semileptonic channel and $207.2^{+12.9}_{-9.7}$ pb for the others, excluding all-hadronic t̄t events [1, 14]. Table 5.1 gives the number of events for the different decay categories, selected according to the Monte Carlo truth information. For 40 events no unambiguous assignment could be made, e.g. due to the production of a second top pair. These events have been excluded from all further analysis.

5.2.2 W+Jets Background

Leptonically decaying W bosons with associated jets are a major source of background in the semileptonic t̄t decay channel since the final state may contain exactly the same particles, namely a charged lepton, a neutrino plus QCD jets, as the t̄t signal, see Figure 5.1. Due to the limited detector resolution the W+jets background events are indistinguishable from the t̄t signal on single event basis. Since only events with at least four jets will be selected for analysis, a filter to reject events with less than three true jets directly after the ALPGEN [9] & HERWIG [4] generators has been applied before the time consuming detector simulation. The generated W+jets cross section, including the filter efficiency[1], amounts 813 pb [40]. An additional correction factor of 1.15 has to be applied to scale this sample to the theoretically calculated next-to-leading order cross section, resulting in 935 pb [41]. The statistics and cross sections of the individual samples are listed in Table 5.2.

5.2.3 Single Top Background

Events with leptonic single top decays plus jets from initial or final state radiation, see Figure 5.2, are a second source of irreducible background, i.e. only kinematically distinguishable from the

---

[1]Electrons are considered as jets by the truth filter.
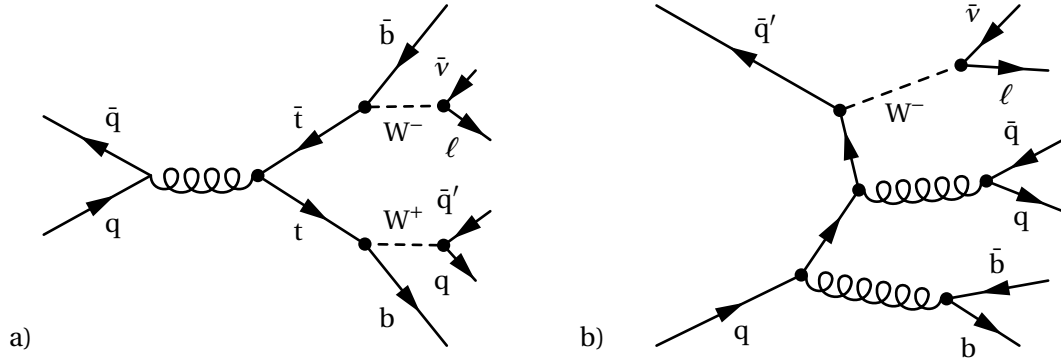
Figure 5.1: Semileptonic anti-top pair decays (a) and leptonic W decays with associated jets from initial state radiation (b) may have the same particles in the final state.

Sample	Events	Cross Section [pb]
$W \rightarrow e\nu + 2$ partons	21 950	246.1
$W \rightarrow e\nu + 3$ partons	11 250	142.5
$W \rightarrow e\nu + 4$ partons	6 000	61.7
$W \rightarrow e\nu + 5$ partons	4 950	25.7
$W \rightarrow \mu\nu + 2$ partons	7 000	18.8
$W \rightarrow \mu\nu + 3$ partons	12 500	74.4
$W \rightarrow \mu\nu + 4$ partons	3 200	41.4
$W \rightarrow \mu\nu + 5$ partons	2 750	23.3
$W \rightarrow \tau\nu + 2$ partons	19 700	100.9
$W \rightarrow \tau\nu + 3$ partons	13 000	100.2
$W \rightarrow \tau\nu + 4$ partons	5 750	52.8
$W \rightarrow \tau\nu + 5$ partons	550	23.9
$Wb\bar{b} + 0$ partons	6 250	7.2
$Wb\bar{b} + 1$ partons	7 200	8.0
$Wb\bar{b} + 2$ partons	4 000	4.5
$Wb\bar{b} + 3$ partons	3 000	3.2

Table 5.2: The available statistics for the W+jets samples plus the expected NLO cross sections including the 3 true jets filter efficiency. The decays with $b\bar{b}$ production in the hard interaction have been produced separately.

signal. The t-channel has at least three quarks two of which are b-quarks in the final state plus charged lepton and neutrino from the leptonic W decay. The cross section including hadronic decays has been calculated to be $246.6^{+11.4}_{-11.9}$ pb [42]. In the s-channel only two b-jets originate from the hard interaction plus the W decay products, so here two additional jets from initial or final state radiation are necessary for background events. A production cross section of $10.65^{+1.06}_{-0.97}$ pb is predicted [42]. The Wt-channel has three or more quarks in the final state including one b-quark and the charged lepton plus neutrino. Here the total cross section is expected to be 66 ± 2 pb [43]. The samples for all three channels have been produced with ACERMC [44], a leading order Monte Carlo Generator, plus PYTHIA [3] parton showers. All samples exclude hadronic W decays[2]. A

---

[2]In the Wt-sample at least one W has to decay leptonically.
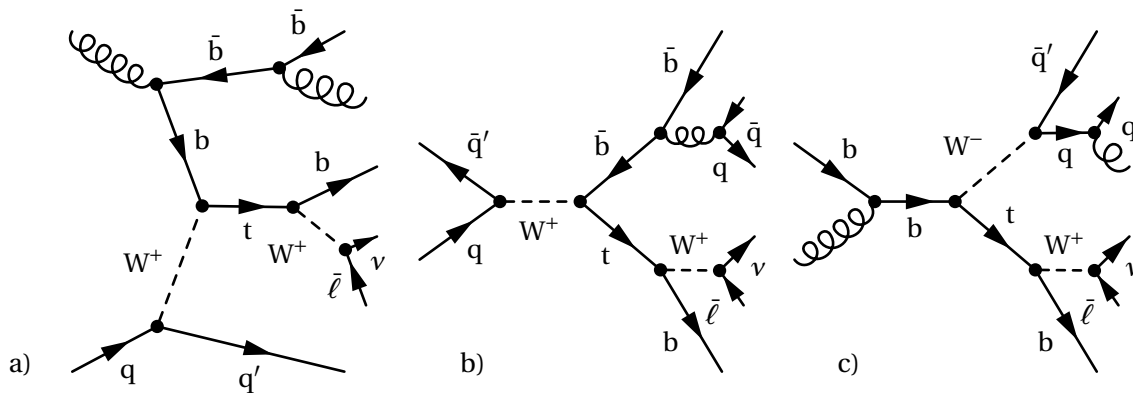
Figure 5.2: Background from single top events to semileptonic top pair decays is produced via the *t*-channel (a), the *s*-channel (b), and the Wt-channel (c).

Channel	Events	Cross Section [pb]
t	18 500	79.7
s	9 750	5.0
Wt	15 200	30.4

Table 5.3: The number of events in the single top samples plus the cross section times branching ratio for leptonic decays (incl. τ).

summary is listed in Table 5.3.

5.2.4   QCD Background

In principle pure QCD events should not contribute any background to an analysis with leptons in the final state such as semileptonic t$\bar{\text{t}}$ events. However, occasionally the shower of a jet in the calorimeter is ambiguous and a jet is reconstructed as an electron. Such fakes are supposed to occur due to π^0 decays into photons within a jet, leading to a larger signal in the EC. Furthermore real leptons may originate from weak decays inside the parton showers at momentum transfers large enough for the lepton to lie outside the overlap removal cone. Such a lepton is reconstructed as an individual object. Especially b-jets are a source of these non-prompt leptons. Although these mis-reconstructions are expected to appear rarely, the high cross section for QCD events requires the consideration of this background. Another difference between the signal and the QCD background is the absence of missing transverse energy from neutrinos. However, in QCD events neutrinos occur within weak decays inside the parton showers. Some missing transverse energy also arises from the limited energy resolution of the detector and the consequently imperfect vectorial energy balancing.

Unfortunately the production of fully simulated QCD samples with the required number of events is impracticable and too time consuming, even on the LHC-Computing Grid. In the next section a method to create QCD background events with fake and non-prompt leptons from collisions simulated with ATLFAST is presented.

Sample	Cross Section [nb]	Events
3 partons	4 766	162 878
4 partons	480	210 000
5 partons	48	430 106
6+ partons	26	449 900
4 partons (b)	69	38 000
5 partons (b)	16	74 843
6 partons (b)	4	77 980

Table 5.4: Cross sections and statistics of the available ALPGEN events.

5.3 QCD Background Model

Although no fully simulated QCD background sample could be created it is still possible to study the QCD background using samples produced with ATLFAST, when assuming a fake electron probability. The following method interprets 4-vectors of reconstructed jets as leptons and weights events according to assumed fake rates.

5.3.1 ATLFAST Samples

For an all-hadronic $t\bar{t}$ analysis QCD background events have been created as described in [45]. The event generation was performed by ALPGEN [9], interfaced to PYTHIA [3] for the parton showers. Exclusive samples are available for 3, 4 and 5 light jets plus another inclusive sample for 6 or more light jets. For all samples except the 3 jets additional samples with b-quarks in the final states are available. The corresponding cross sections, as calculated by ALPGEN, are reproduced in Table 5.4 as well as the number of events used.

For this analysis these generated events have been used as input for a parametrised detector simulation with ATLFAST in ATHENA version 12.0.6 choosing cone jets with a radius of 0.4. As simulated at the generator level, non-prompt leptons from the parton showers already exist in the samples. Fake electrons are not covered since ATLFAST simulations do not provide calorimeter showers.

5.3.2 Fake Electron Model

Most QCD events do not contain fake electrons. Selecting fake events at the generator level is impossible as fake electrons would occur during the GEANT4 step in a full simulation. However, assuming an average fake probability and a negligible difference between the 4-vectors of calorimeter objects when reconstructed either as electron or jet, the QCD background can be approximated with the available ATLFAST samples. For every single event each jet 4-vector is taken once and considered as a reconstructed electron while the other jets remain unchanged and the event is weighted with the fake probability. Looping over all n jets in an event results in n new events with one additional fake lepton plus $n-1$ jets. The chance of more than one fake lepton per event can be neglected as the associated probability is of the order of the fake probability squared. Thus the new effective cross sections have to be calculated according to

Partons	σ [pb]	$\langle n_{jets} \rangle$	σ_{eff} [pb]
3	$4.766 \cdot 10^6$	2.390	11 390
4	$4.80 \cdot 10^5$	3.315	1 591
5	$4.8 \cdot 10^4$	4.318	207
6+	$2.6 \cdot 10^4$	6.392	166
4 (b)	$6.9 \cdot 10^4$	3.188	219
5 (b)	$1.6 \cdot 10^4$	4.171	67
6+ (b)	$4 \cdot 10^3$	6.133	25

Table 5.5: Expected effective cross section of the QCD samples with jets falsely reconstructed as electrons.

| Partons	Jets	Leptons	Non-prompt Rate
3	397 453	7	$(1.8 \pm 0.7) \cdot 10^{-5}$
4	705 368	23	$(3.3 \pm 0.7) \cdot 10^{-5}$
5	1 856 940	65	$(3.5 \pm 0.4) \cdot 10^{-5}$
6+	2 964 990	107	$(3.6 \pm 0.3) \cdot 10^{-5}$
4 (b)	123 152	118	$(95.8 \pm 8.8) \cdot 10^{-5}$
5 (b)	318 466	232	$(72.8 \pm 4.8) \cdot 10^{-5}$
6 (b)	500 948	203	$(40.5 \pm 2.8) \cdot 10^{-5}$

Table 5.6: Non-prompt lepton rates for the original ALPGEN QCD samples.

$$\sigma_{\text{eff}} = \sigma \cdot P(j \to e) \cdot \langle n_{\text{jets}} \rangle \tag{5.4}$$

Using the mean values for the number of jets per events in the available QCD samples as shown in Figure 5.3 for $\langle n_{\text{jets}} \rangle$ and assuming an average probability $P(j \to e) = 10^{-3}$, the order of magnitude observed at the D0 experiment at the Tevatron [46] for fake electrons, leads to the effective cross sections listed in Table 5.5. For other probabilities the effective cross sections have to be scaled accordingly. The effective volumes of the samples also increase by a factor of $\langle n_{\text{jets}} \rangle$ but for the price of correlated events.

5.3.3 Total QCD Background

The total QCD background does not consist only of the modelled fake electrons but also contains non-prompt leptons from the weak component of the parton showers escaping the jet cones. Table 5.6 gives the number of reconstructed leptons surviving the overlap removal for the different QCD samples and compares the result with the total number of reconstructed jets in the sample via the counting rate ratio. Here only leptons with $p_T > 20$ GeV, $|\eta| < 2.5$ as selected by TOPVIEW are considered. In addition $\Delta R > 0.4$ between the lepton trajectory and all jet axes is required as used in the analysis later on. As expected most non-prompt leptons occur in the QCD samples containing b-quarks in the hard interaction as the high b-quark mass facilitates sufficient momentum transfers during weak decays. Unfortunately the usage of the original QCD samples involves large scaling factors for the non-prompt lepton QCD background. However, for fake rates of $\mathcal{O}(10^{-3})$ the non-prompt leptons should contribute little to the QCD background.
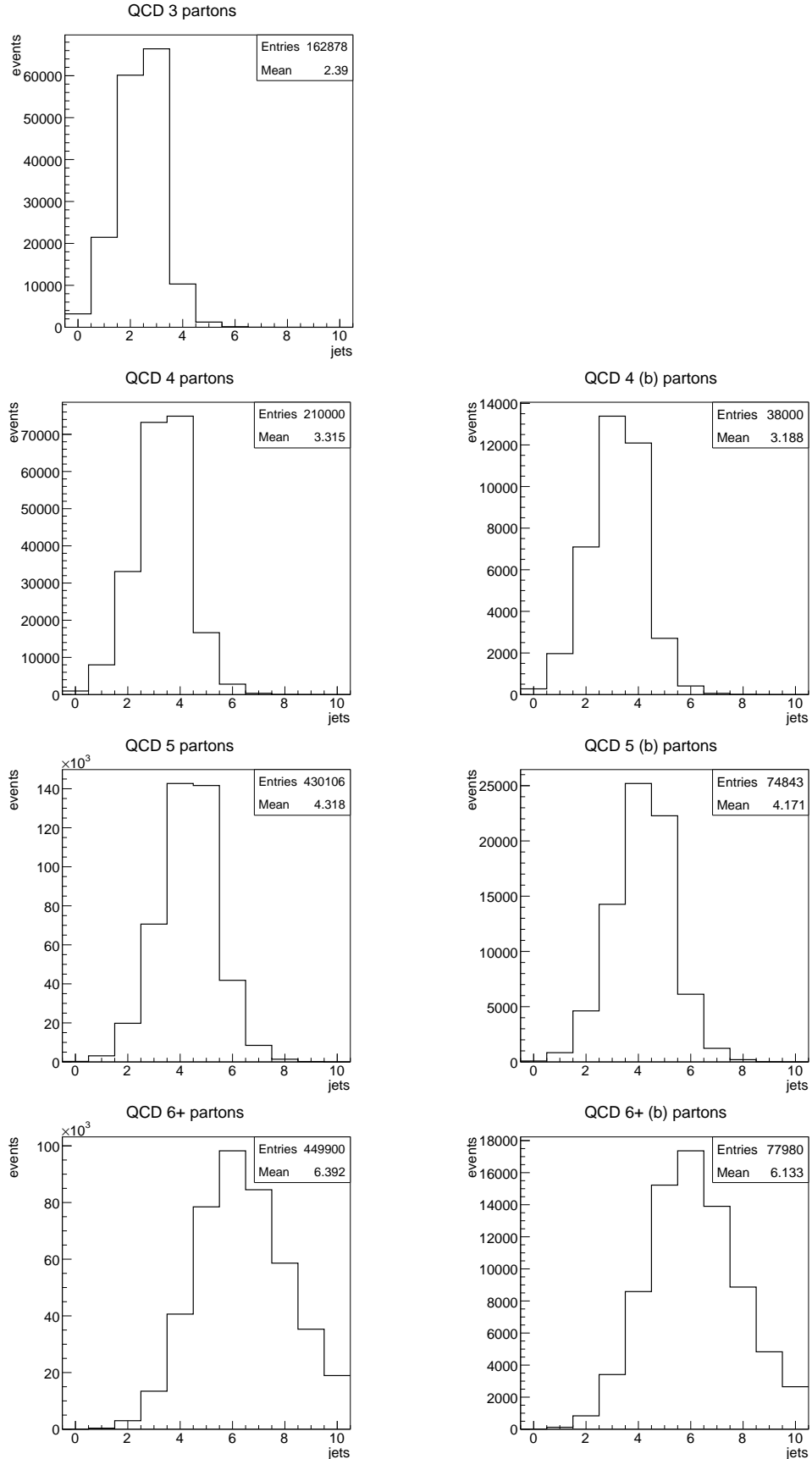
Figure 5.3: The number of jets per event in the QCD samples for the different final state parton multiplicities without (left) and with (right) b-quarks in the hard interaction.

For a complete QCD model both the fake electron QCD events and the original samples have been taken. Any overlap between this double usage will be removed when demanding exactly one reconstructed lepton in the analysis. As the fractions of fake electron events and non-prompt lepton events are small the cross sections remain uncorrected for the overlap.

5.4   Event Selection with First Data

The following selection is based on a proposal for a semileptonic $t\bar{t}$ cross section analysis which was originally developed on the basis of ATHENA version 10 simulations [47]. Regularly adjusted to the latest simulation samples this analysis emerged as a commissioning analysis standard within the ATLAS top cross section group. Hence the semileptonic analysis presented here complies with this proposal to keep coherency. This decision also allows for straightforward cross checks.

5.4.1   Trigger Stage

At ATLAS it is impossible to store the data from all collisions. As described in Section 3.2.5 a three stage trigger system discriminates between collisions of interest and background events. Since the trigger is not perfect and as its efficiency depends on the kinematics of a channel the trigger decision has to be considered in an analysis. In principle triggers are available for electrons and muons as well as for jets and other objects, each with several momentum thresholds and distinct object multiplicities. But since the electron and muon triggers are robust and unprescaled, i.e. without artificially reduced efficiency since lower threshold energies can be dealt with than for jets, only these triggers will be considered here even for the costs of a considerably reduced selection efficiency. For muons at least 20 GeV at all trigger stages is required and for electrons a 25 GeV threshold plus an isolation requirement was chosen. Figure 5.4 shows the trigger efficiencies for the signal and background samples after the three trigger levels as simulated by ATHENA. The numeric values are given in Table 5.7. The signal efficiency lies above 57% while the background events pass the trigger with a probability of less than 35% and 40%, respectively. So already at trigger level the background is suppressed, confirming the choice of the triggers. One reason for this behaviour is the non-constant 4-momentum dependence for the efficiency of the chosen triggers in combination with the different kinematics of the examined samples, especially around the threshold values. A second cause is the existing fraction of τ lepton events in all the background samples since tau leptons decay either into pions, which are not considered by the selected triggers, or into lower energetic charged leptons which are likely to not exceed the trigger thresholds. This effect is demonstrated in Figure 5.5 for the τ component of the $t\bar{t}$ background in comparison to the semileptonic signal.

As the QCD samples have only been generated with the fast simulation the trigger influence could not be examined here. But from Figure 5.6, where the triggering probabilities as a function of the reconstructed lepton transverse momenta are plotted, it is apparent that for leptons above the trigger turn-on threshold the triggering probability stays approximately constant, at a value independent of the sample considered. By separating electronic and muonic W decays in the W+jets samples and fitting a constant trigger efficiency for transverse momenta larger than 30 GeV, a trigger probability of 87% for reconstructed electrons and 78% for reconstructed muons in the plateau region is obtained. In the following the QCD events will be weighted according to these probabilities by assuming all fake electrons have the same trigger probability as real electrons. The turn-on region will be excluded from analysis, as explained in the next section. A dependency on
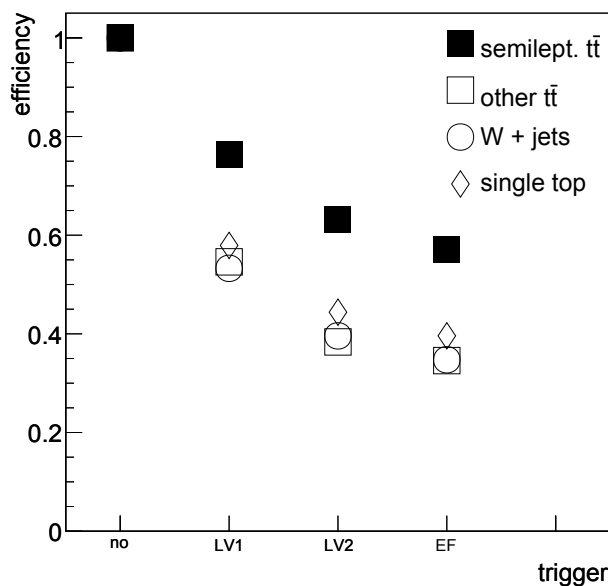
Figure 5.4: The efficiency after the Level 1 (LV1), Level 2 (LV2) and Event Filter (EF) trigger stages.

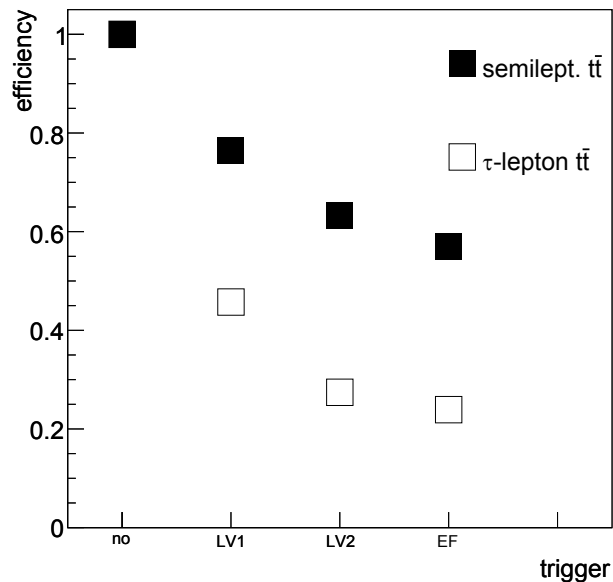| Sample	Level 1	Level 2	Event Filter
semileptonic t$\bar{t}$	0.764 ± 0.003	0.632 ± 0.002	0.571 ± 0.001
other t$\bar{t}$	0.546 ± 0.002	0.384 ± 0.002	0.346 ± 0.001
W+jets	0.533 ± 0.002	0.396 ± 0.002	0.347 ± 0.001
single top	0.579 ± 0.005	0.444 ± 0.004	0.396 ± 0.003

Table 5.7: Trigger efficiency values for signal and background samples.

$|\eta|$ of the triggering probability in the plateau region, as examined in Figure 5.7, has been neglected for the QCD events.

5.4.2 Lepton Selection Criteria

In spite of the preselection and overlap removal by TopView not all reconstructed leptons should be used for analysis. Leptons with $|\eta| > 2.5$ have been removed by TopView in advance and also leptons with $p_T < 20$ GeV are vetoed for analysis. To avoid double counting all leptons reconstructed within a jet cone are rejected and as a precaution electrons in the ECAL crack region $1.37 < |\eta| < 1.52$, which might not be completely understood in the early phase, are also ignored. All electrons and muons passing this preselection are considered to be good lepton candidates.

To increase the signal to background significance events with no or more than one good lepton are removed a priori. For events with exactly one good lepton the $|\eta|$ distribution has been inspected, see Figure 5.8, but no significant selection criterion could be found. As the QCD would dominate a plot where all samples were on the same scale the individual distributions have been normalised for better visibility of the shapes. For the lepton p_T distributions in Figure 5.9 the plots are nor-

Figure 5.5: The efficiency after the Level 1 (LV1), Level 2 (LV2) and Event Filter (EF) triggers for the τ component of the $t\bar{t}$ background and the semileptonic $t\bar{t}$ decays.
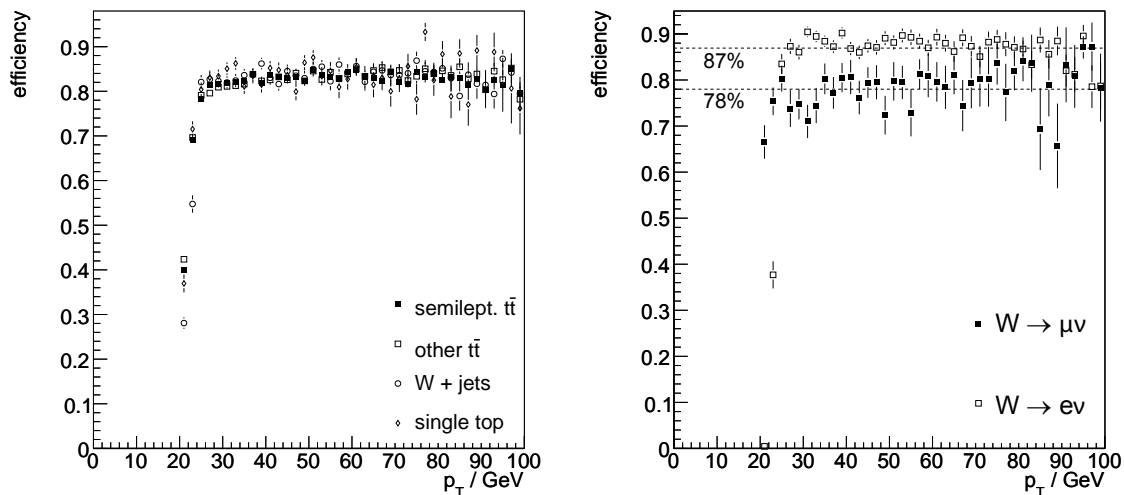
Figure 5.6: Triggering efficiency as a function of the transverse momentum of the reconstructed lepton for events with exactly one reconstructed electron or muon. The left plot shows the compatibility of the results amongst all samples. On the right the W + light jets samples have been split into electronic and muonic W decays, exemplifying the different triggering probabilities for electrons and muons. All samples have been weighted according to their cross sections.
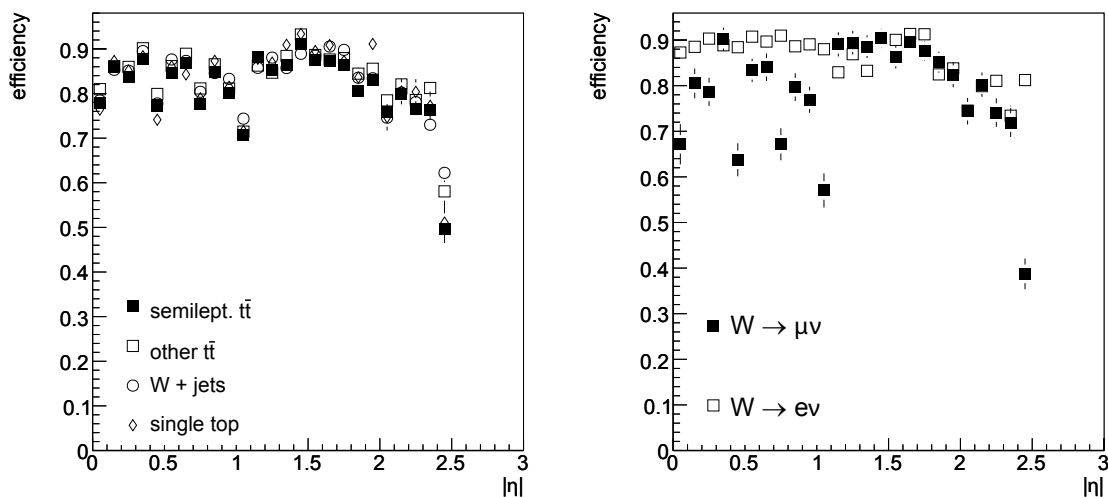
Figure 5.7: Triggering efficiency as a function of $|\eta|$ of the reconstructed lepton for events with exactly one re-constructed electron or muon in the trigger plateau region ($p_T > 30$ GeV). The left plot shows the results for both electrons and muons for all samples. The right plot differentiates between electronic and muonic W decays in W + light jets events. All samples have been weighted according to their cross sections. The fluctuations are due to acceptance gaps of the detector.

malised again. Here the solid line indicates the significance for a possible cut with the value given for a fake electron rate of 10^{-3} and $10\,\text{fb}^{-1}$ integrated luminosity. Due to the finite W mass the selection significance improved when rejecting events with transverse lepton momenta smaller than 37 GeV at a fake rate of 10^{-3}. The best cut value depends only slightly on the fake rate. E.g. for 10^{-2} fake electron probability the optimum threshold value shifts to 40 GeV. For lower fake rates the best cut value does not drop below 30 GeV as non-prompt leptons form the dominant background in this region. The best cut-off value remains constant, independent of optimising with or without the trigger simulation. However, a re-inspection of the lepton p_T cut after all the following semileptonic analysis cuts showed that due to correlations with the jet selection the optimum value drops down to the trigger thresholds, i.e. in principle a lepton p_T cut should not be necessary. However, because of the uncertainty associated with the trigger simulation in this region a safe 30 GeV lower cut is chosen for the analysis.

Another interesting aspect of leptons might be their isolation in the detector, i.e. the absence of activity in the surrounding detector elements. Unfortunately for electrons in ATHENA 12.0.6 no reliable calorimeter isolation variable was available. Furthermore, appropriate variables are not included in the ATLFAST QCD samples. So only the isolation in terms of the spatial distance ΔR between the lepton and the axis of the closest jet could be examined. Figure 5.10 shows the lepton isolation distributions for the signal and the background samples, individually normalised for better shape visualisation. At first glance removing events with large ΔR values seems to be necessary, especially to reduce the QCD background. However, a closer inspection of the QCD subsamples in Figure 5.11 reveals the large fraction of QCD events with fewer final state partons and hence fewer jets responsible for the highly isolated events. As the use of an isolation criterion for ATLFAST samples is particularly arguable no cut on ΔR (except during the previous good lepton selection) is applied. Instead, most of the QCD background will be removed in the following selections concerning jets and missing transverse energy.
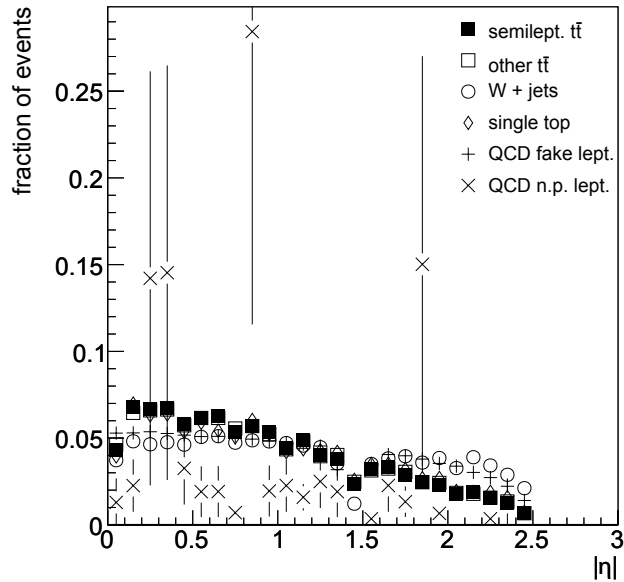
Figure 5.8: Normalised $|\eta|$ distributions of reconstructed leptons for events with exactly one good lepton.
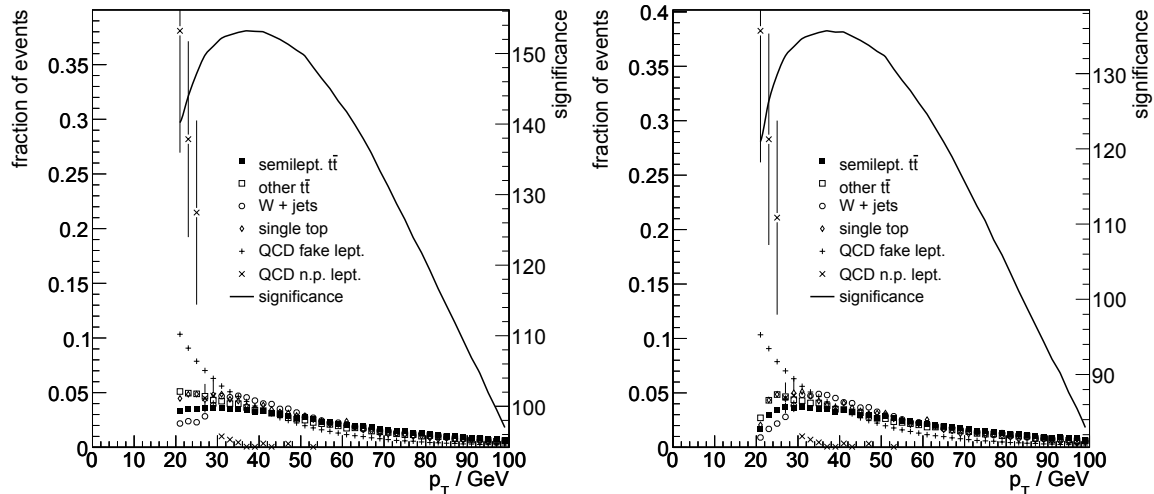
Figure 5.9: Normalised p_T distributions of reconstructed leptons for events with exactly one good lepton. The solid line indicates the significance at $10\,\mathrm{fb}^{-1}$ integrated luminosity with 10^{-3} fake electron probability when rejecting events with lower transverse momenta. The left plot does not consider the trigger simulation whereas the right plot does. In both cases the best cut lies at $37\,\mathrm{GeV}$. The large error bars for the leftmost points of the non-prompt QCD background originate from the low statistics (7 events with one good lepton) and correspondingly large scaling factor of the QCD 3 partons sample.
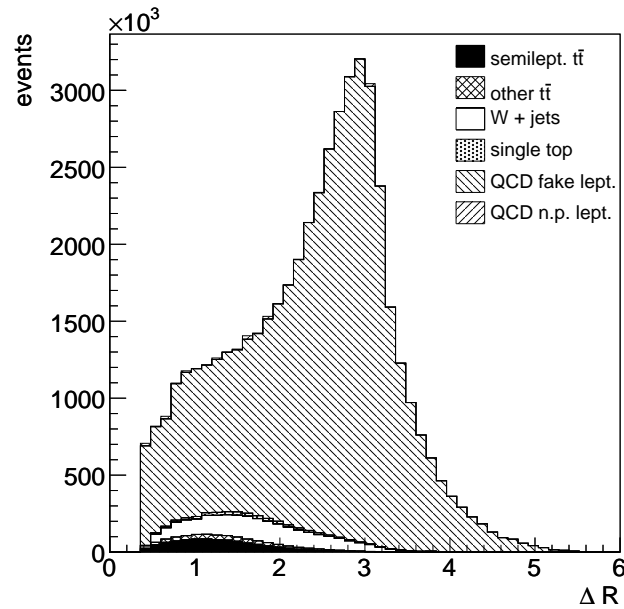
Figure 5.10: Stacked ΔR isolation distribution of reconstructed leptons for events with one good lepton. All samples have been scaled to $10\,\mathrm{fb}^{-1}$ integrated luminosity and 10^{-3} fake electron probability was assumed for the QCD background.
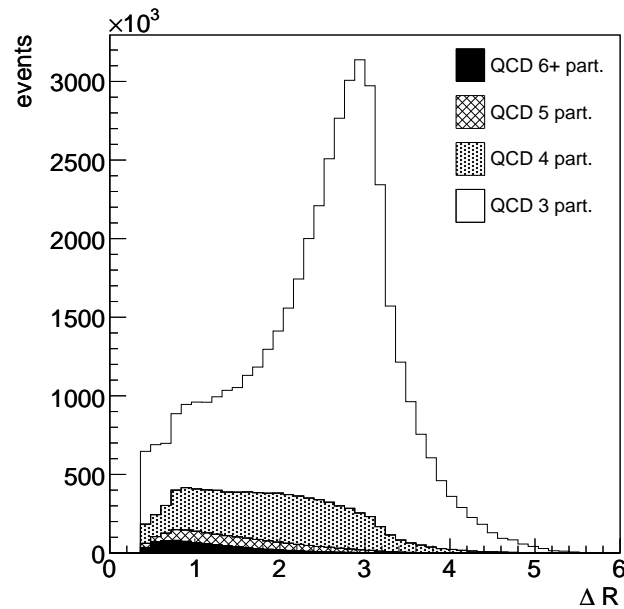
Figure 5.11: Stacked ΔR isolation distribution of reconstructed leptons for one lepton QCD events. Events with highly isolated leptons occur mostly in the QCD samples with less final state partons which have larger distances between the jets on average.

5.4.3 Particle Jet Properties

The second class of reconstructed objects used in this analysis are particle jets. As the semileptonic $t\bar{t}$ signal contains four final state quarks whereas the background samples also include other multiplicities, a cut on the number of jets is crucial. Furthermore a cut requiring three or more true jets with $p_T > 20\,\text{GeV}$ was applied to the W+jets samples at the generator level. As the number of jets reconstructed after the full detector simulation may easily differ by one from the jet multiplicity as reconstructed from Monte Carlo truth particles, in the following at least four jets with transverse momenta larger than $20\,\text{GeV}$ will be demanded. This selection already removes a major part of the W+jets and QCD samples with low final state parton multiplicities. Also dileptonic $t\bar{t}$ events or τ events are unlikely to pass this cut due to their fewer final state quarks. The significance can be enhanced when applying higher p_T threshold values to some of the reconstructed jets. For events with at least four jets Figure 5.12 shows the transverse momentum distributions for the four highest p_T jets in each event. The solid line indicates the significance of a cut at a certain p_T value when cutting on this jet exclusively. Table 5.8 gives the significance for the best cut. In principle applying all the cuts on the different jets at the same time should raise the significance even more. However, in practice the improvement is marginal: when demanding $p_T > 50\,\text{GeV}$ for the leading jets, $p_T > 40\,\text{GeV}$ for the second, and $p_T > 30\,\text{GeV}$ for the third leading jets the significance remains constant at a value of 424 for an integrated luminosity of $10\,\text{fb}^{-1}$. Apparently the jet p_T cuts are strongly correlated. As the correlation might be different between some of the jets one might consider scanning the four dimensional threshold space for the best cuts. However, since the commissioning analysis in [48] only distinguishes between jets above $40\,\text{GeV}$ and $20\,\text{GeV}$ this scheme will be used here, too. Figure 5.13 shows the selection significance, represented by the box sizes, when requiring a minimum number of jets above $20\,\text{GeV}$ and among them another number of jets exceeding $40\,\text{GeV}$. The optimum is reached when at least four jets above $20\,\text{GeV}$ exist, of which two or more have at least $40\,\text{GeV}$ transverse momentum. The selection significance attains a value of 427 for $10\,\text{fb}^{-1}$ integrated luminosity which is even slightly better than the combination of the individual best jet p_T cuts. The commissioning analysis as referenced above differs at this point as it requires three jets above $40\,\text{GeV}$. Here this would correspond to a lower significance of 399.

Another variable of interest is the pseudorapidity of the jets. It might be expected that the jets within the $t\bar{t}$ signal events tend to lie in the more central region of the detector. Due to the high top mass the centre-of-mass frame should correspond more to the lab frame. Hence $t\bar{t}$ jets should be less boosted than the background jets. But, as Figure 5.14 shows, this effect seems to be marginal due to the high collision energy at the LHC and therefore no $|\eta|$ cut apart from the TOPVIEW preselection is considered.

Jet	Optimum p_T Cut [GeV]	Significance
1st	51	424
2nd	39	427
3rd	30	426
4th	21	417

Table 5.8: Significance for cutting on a single jet p_T at the optimum threshold without considering the other jets. The values are calculated for $10\,\text{fb}^{-1}$ integrated luminosity and 10^{-3} fake electron probability.
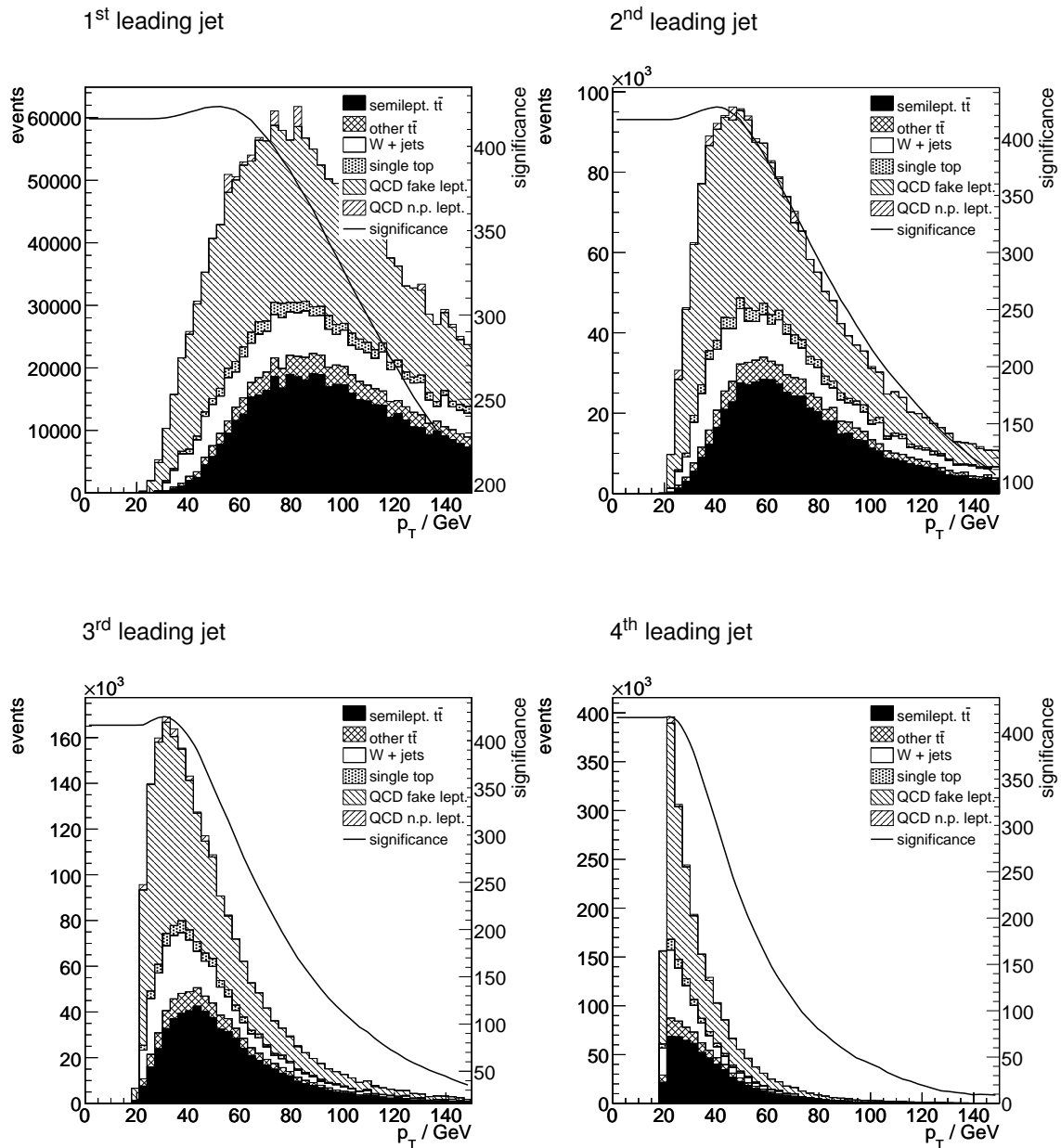
Figure 5.12: Stacked jet p_T distributions for $10\,\text{fb}^{-1}$ integrated luminosity at 10^{-3} fake electron probability for the four leading jets. The maximum of the significance line indicates the best cut.

5.4.4 Missing Transverse Energy

As an object not directly reconstructed by the detector but calculated from the E_T balance, the missing transverse energy ($\not{E}_T$) might not be sufficiently understood in the very first phase of AT-LAS to be useful for analysis. However, as soon as it is available missing transverse energy will provide a quantity especially suited to distinguish QCD background from the other processes, as QCD has no real $\not{E}_T$ except for the weak component within parton showers. In particular if fake electron rates are larger than expected the analysis benefits a lot from a cut on missing transverse energy, as this section will show.
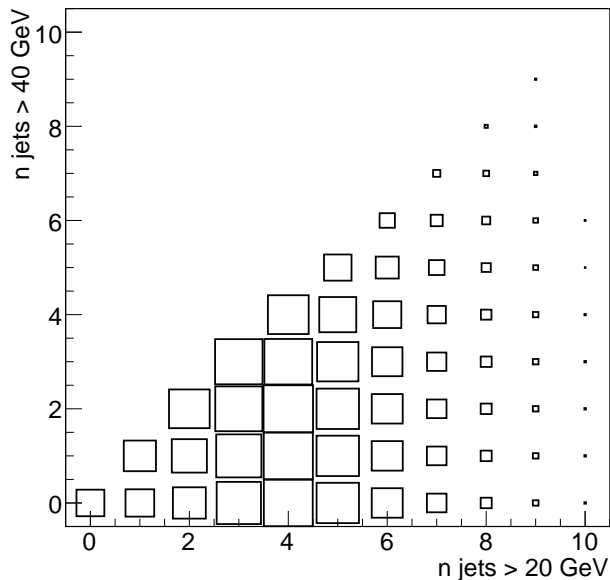
Figure 5.13: Significance of a combination of cuts on jets with $p_T > 20\,\text{GeV}$ and the number of jets with $p_T > 40\,\text{GeV}$. For the optimum at least four 20 GeV jets of which at least two exceed 40 GeV are demanded.

Figure 5.15 shows the $\not{E}_T$ distribution for the signal plus background, as usual for 10^{-3} fake electron probability. Already visible to the bare eye is the pronounced separation of QCD events, which peak at low values of missing transverse energy as expected. The significance amounts to 509 at $10\,\text{fb}^{-1}$ integrated luminosity for the optimum cut at about 20 GeV. If using the jet selection of the commissioning analysis the significance reaches 458 for a 20 GeV $\not{E}_T$ cut.

Of course this best cut might change for scenarios with a different fake electron probability. In principle the previous cuts would also be affected, but as the amount of QCD background events can be estimated well from the $\not{E}_T$ distribution, as explained later in Section 6.2, it is reasonable to keep the previous cuts fixed. Figure 5.16 shows the $\not{E}_T$ distributions for other fake rates of 10^{-4}, $5 \cdot 10^{-4}$, $5 \cdot 10^{-3}$, and 10^{-2}. The values of the best cuts are collected in Table 5.9. For fake electron rates considerably lower than the 10^{-3} scenario the importance of the $\not{E}_T$ cut drops as the significance improves just a little compared to the situation without the optimum $\not{E}_T$ cut. However, in the cases of the high fake rates the significance benefits considerably from the application of the cut.

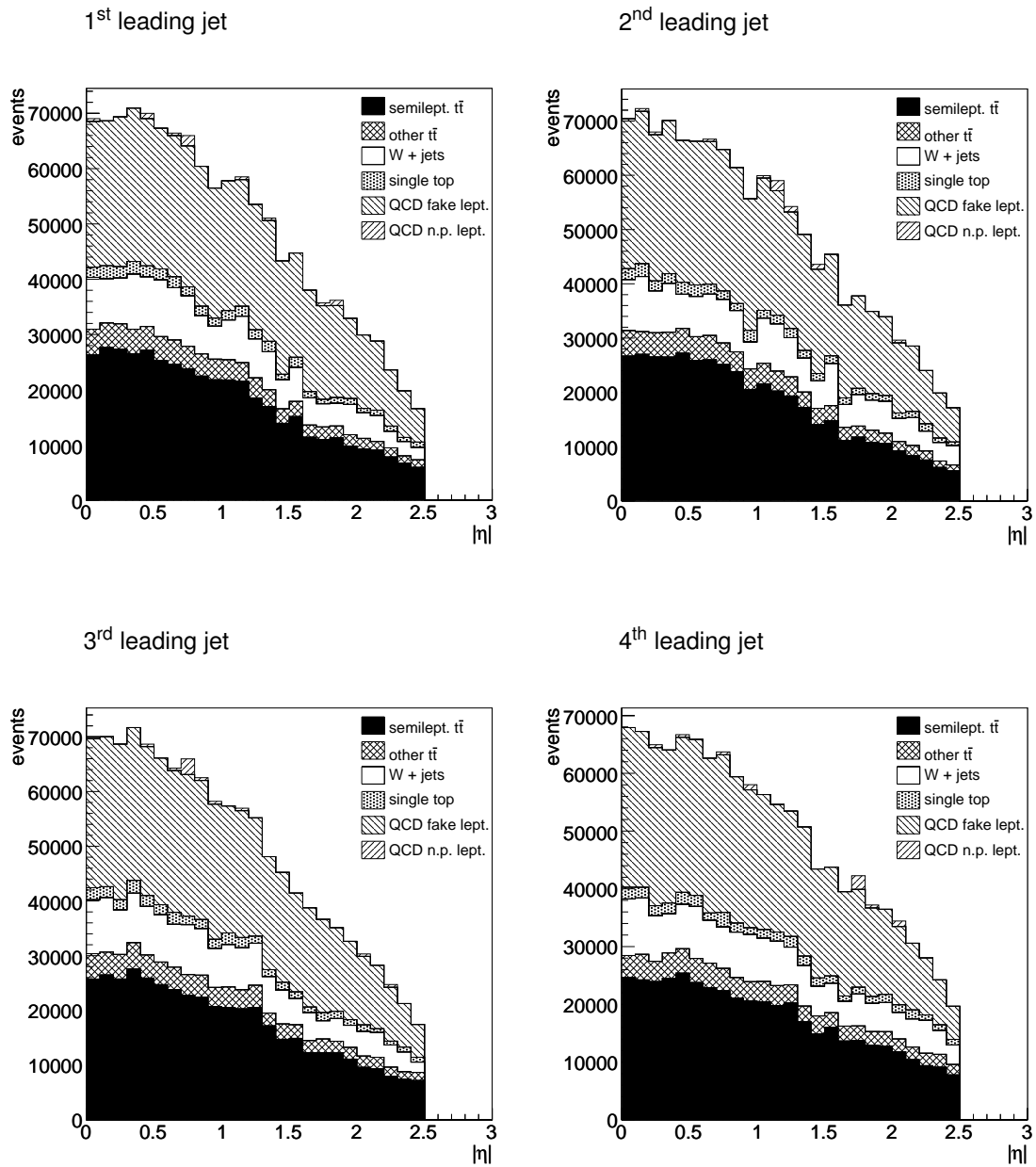| Fake Rate	Optimum $\not{E}_T$ Cut [GeV]	Cut Significance	No Cut Significance
10^{-4}	9	553	551
$5 \cdot 10^{-4}$	18	525	484
10^{-3}	21	509	427
$5 \cdot 10^{-3}$	30	453	256
10^{-2}	33	418	191

Table 5.9: Significance for cutting on $\not{E}_T$ at the optimum threshold plus the original significance before the cut. The values are calculated for $10\,\text{fb}^{-1}$ integrated luminosity and 10^{-3} fake electron probability.

Figure 5.14: Stacked jet $|\eta|$ distributions for $10\,\text{fb}^{-1}$ integrated luminosity at 10^{-3} fake electron probability for the four leading jets showing that the signal efficiency cannot be improved by cutting on $|\eta|$.

5.5 Top and W Reconstruction

In principle the kinematic reconstruction of the top quarks should further improve the selection significance. In this section a simple reconstruction of both top quarks as well as the W bosons, in agreement with the standard commissioning analysis, is presented. It turns out that more sophisticated methods which are not considered here and are unlikely to be applicable to early ATLAS data, such as a kinematic fit, are necessary to improve the selection by means of the top mass.
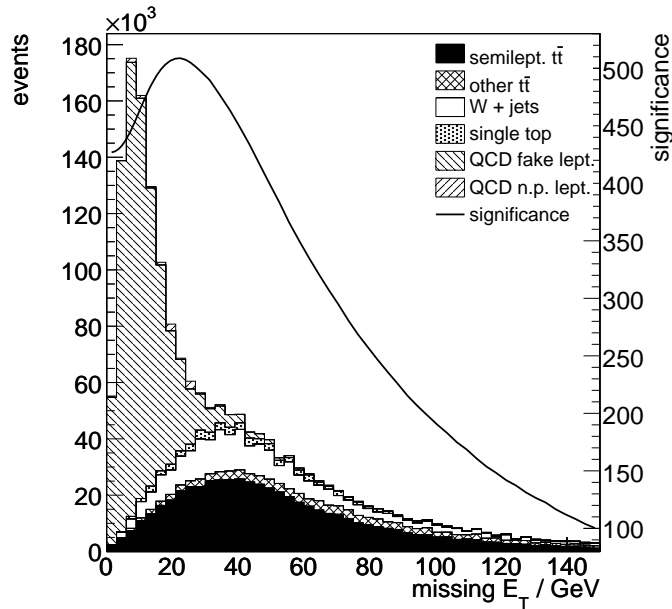
Figure 5.15: Stacked missing transverse energy distributions for a fake electron probability of 10^{-3} and $10\,\mathrm{fb}^{-1}$ integrated luminosity. The solid line indicates the selection significance when removing events below the $\slashed{E}_T$ value.

5.5.1 The Hadronic Branch

In the hadronic branch of $t\bar{t}$ decays all products of the top quark are in theory directly accessible as reconstructed jets. Here the problem is to assign the correct jets to the top quark decay and to cope with the limited jet energy resolution of the detector.

The Hadronic Top Quark

To identify the three jets stemming from the hadronic top decay as a matter of principle it is possible to take all existing combinations of three jets, calculate their invariant masses according to

$$m_{3\mathrm{jets}} = \sqrt{\left(\sum_{i=1}^{3} E_i\right)^2 - \left(\sum_{i=1}^{3} p_{x,i}\right)^2 - \left(\sum_{i=1}^{3} p_{y,i}\right)^2 - \left(\sum_{i=1}^{3} p_{z,i}\right)^2} \tag{5.5}$$

and decide whether one combination is close to the known top mass or not. Neglecting energy losses from final state radiation one expects to find a good triplet of jets for all signal events whilst the background events give a random contribution only. However, in practice there are arguments against such an approach. First of all the detector resolution is finite and smears out the reconstructed invariant masses. Secondly the measured jet energies are probably not calibrated very well, especially during the early phase of data taking, which biases the reconstructed masses, see also Section 6.4. And thirdly the top mass is known with a limited precision only, contributing a further bias. It is possible to correct for the jet energy scale as well as for the top mass, e.g. in connection with a kinematic fit, while also reconstructing the leptonic top decay and using the W mass constraints, assuming a good understanding of the missing transverse energy. Obviously

Figure 5.16: Stacked missing transverse energy distributions for a fake electron probability of 10^{-2} (upper left), $5 \cdot 10^{-3}$ (upper right), $5 \cdot 10^{-4}$ (lower left), or 10^{-4} (lower right). All plots are for $10\,\text{fb}^{-1}$ integrated luminosity. The solid line indicates the selection significance when removing events below this value.
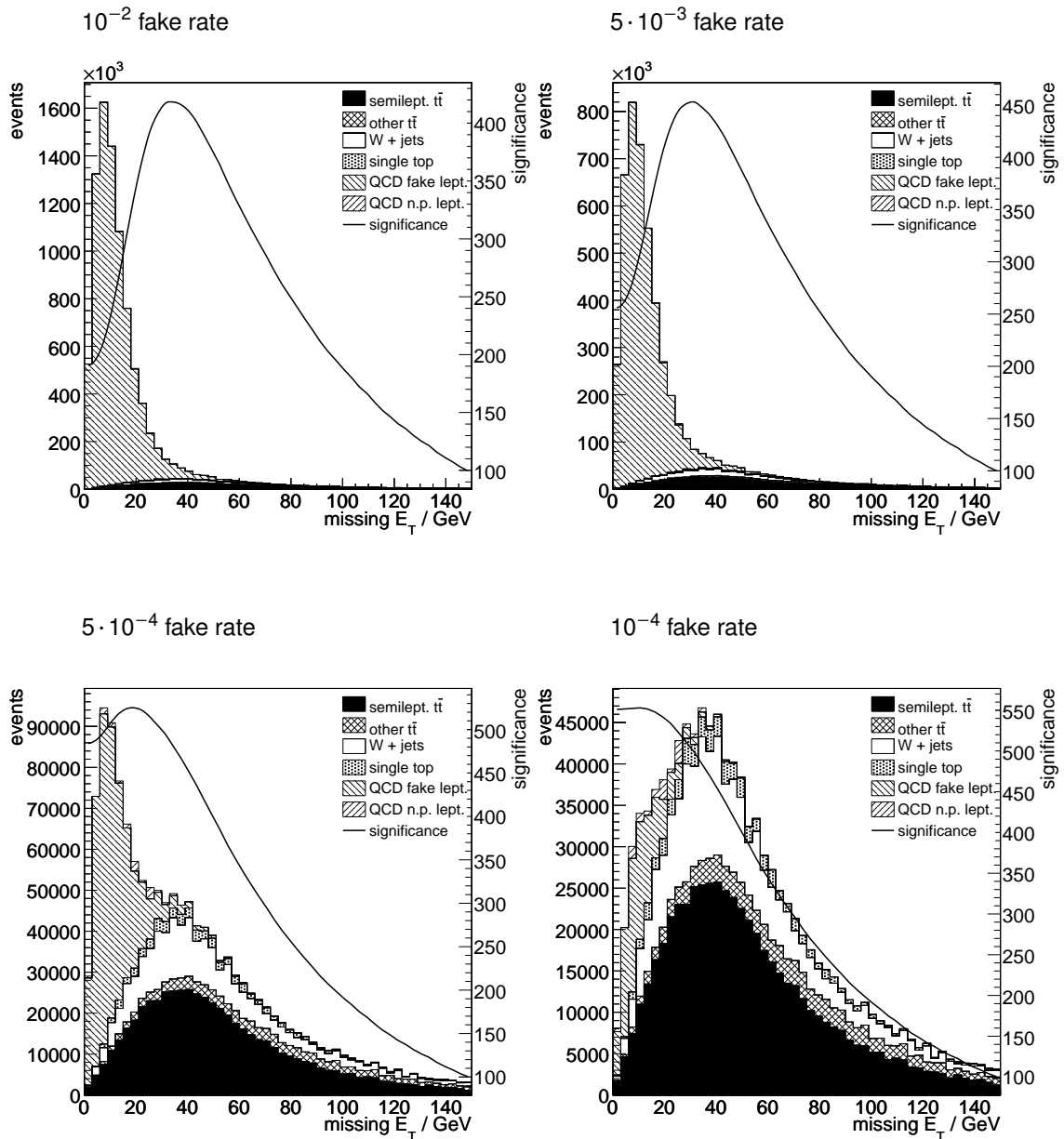
such an analysis is appropriate for a later phase of ATLAS with well calibrated detector modules.

The standard commissioning analysis uses a more robust, but necessarily less precise approach for the top mass reconstruction. Again all possible combinations of three jets are considered but this time the triple with the highest norm of the transverse momentum vector sum

$$|p_T| = \sqrt{\left(\sum_{i=1}^{3} p_{x,i}\right)^2 + \left(\sum_{i=1}^{3} p_{y,i}\right)^2} \tag{5.6}$$
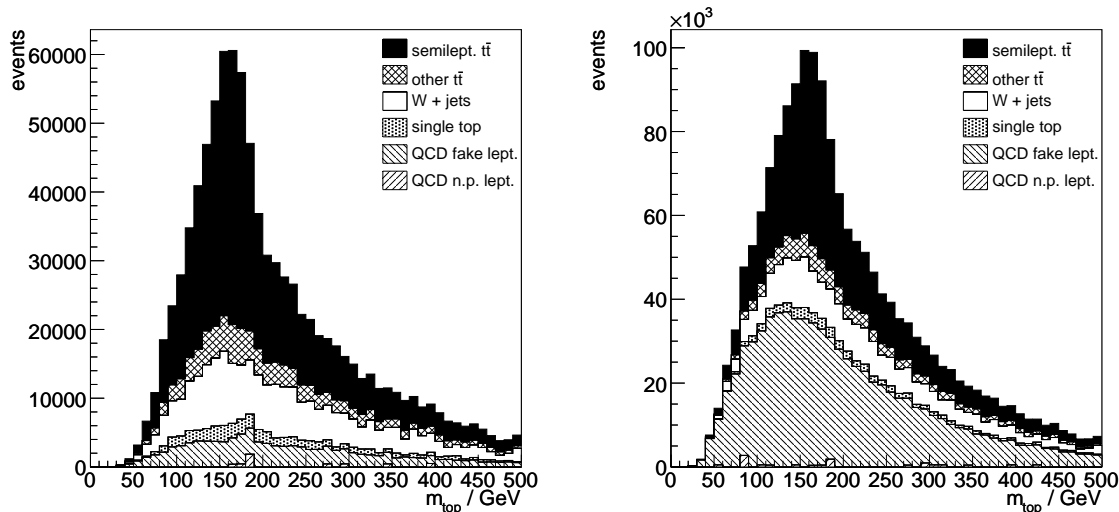
Figure 5.17: Stacked top mass distributions as reconstructed from the three jets with the highest vector sum p_T. Both plots are for a fake electron probability of 10^{-3} and $10\,\text{fb}^{-1}$ integrated luminosity. The left hand plot includes the cut on $\not{E}_T$ whereas the right hand plot does not.

is chosen as the top candidate [47]. This approach is motivated by the tendency of the $t\bar{t}$ system to recoil immediately after production. Of course such a coarse criterion leads to a considerable combinatorial background. One advantage of the method is that a constant jet scale parameter does not affect the choice of jets but merely the value of the reconstructed top mass. The top mass peak in the spectrum of the invariant mass as reconstructed from the three selected jets is shown in Figure 5.17. Even without the previous cut on missing transverse energy the top mass peak is still prominent. The background also shows a maximum in the region around the top mass as the jet preselection favours top-like events. Hence the top mass spectrum does not allow for a further selection improvement. Nevertheless the top mass reconstruction becomes relevant when correcting for the jet energy scale (see Section 6.4) or when estimating the background from data (see Section 6.2).

The Hadronic W Boson

Among the three jets supposed to originate from the hadronic top decay there should be a pair of jets stemming from the W boson decay. In theory one could calculate the invariant mass of all three pairs among the top jet candidates and examine the difference between the reconstructed mass and the well known W mass. But again in practice the number of permutations in combination with the limited detector resolution does not allow for a better event selection. Figure 5.18 shows the difference between the W boson mass and the mass of the dijet combination closest to the nominal W mass. Although for the signal with its true hadronic W decay more events are located around the W mass no cut could increase the selection significance even for the extreme fake lepton frequency scenarios.
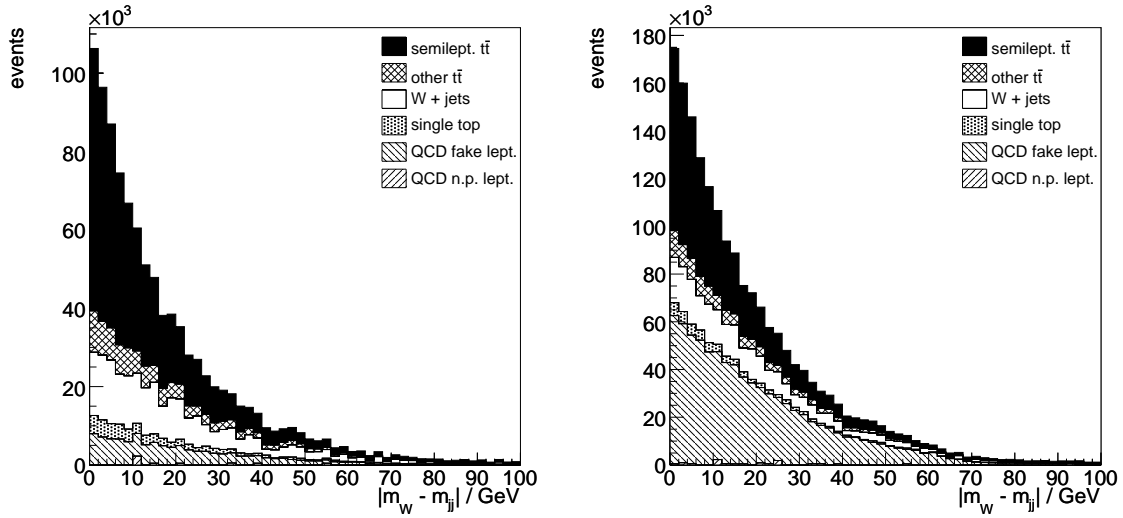
Figure 5.18: Stacked distributions for the mass distances to the W boson for the best fitting pair of jets. The normalisation assumes a fake electron probability of 10^{-3} and $10\,\mathrm{fb}^{-1}$ integrated luminosity. The left hand plot includes the cut on $\not{E}_T$ whereas the right hand plot does not.

5.5.2 The Leptonic Branch

In the leptonic branch of the $t\bar{t}$ decays not all decay products of the top quark can be directly reconstructed from the detected objects as the involved neutrino only appears as missing energy, of which only the transverse components can be obtained from transverse momentum conservation. Hence in the leptonic branch it is necessary to first reconstruct the leptonic W before addressing the top mass.

The Leptonic W Boson

As the z-component of the neutrino momentum cannot be measured, the mass of the W boson cannot be reconstructed. However, by using the W mass as a constraint it is possible to calculate the z-component $p_{\nu,z}$ of the neutrino momentum which is necessary to obtain the desired mass. Up to two solutions may exist as $p_{\nu,z}$ appears squared in the relation

$$m_W^2 = (E_\ell + E_{\nu,T})^2 - (p_{\ell,x} + p_{\nu,x})^2 - (p_{\ell,y} + p_{\nu,y})^2 - (p_{\ell,z} + p_{\nu,z})^2 \tag{5.7}$$

with the W mass m_W, the lepton four-vector $(E_\ell, p_{\ell,x}, p_{\ell,y}, p_{\ell,z})$, and the neutrino four-vector $(E_\nu, p_{\nu,x}, p_{\nu,y}, p_{\nu,z})$. Due to the limited detector resolution the measured energies may be too small for a real solution of the quadratic equation to exist. As the neutrino x- and y-momenta are the components in the equation measured with the least precision they will be scaled according to

$$p_{\nu,i}^{\mathrm{new}} = p_{\nu,i}^{\mathrm{old}} \cdot \frac{m_W^2}{2 \cdot (p_{\nu,T} \cdot p_{\ell,T} - p_{\nu,x} \cdot p_{\ell,x} - p_{\nu,y} \cdot p_{\ell,y})} \tag{5.8}$$

in such cases. This scaling factor is chosen such that the imaginary part of the complex solution
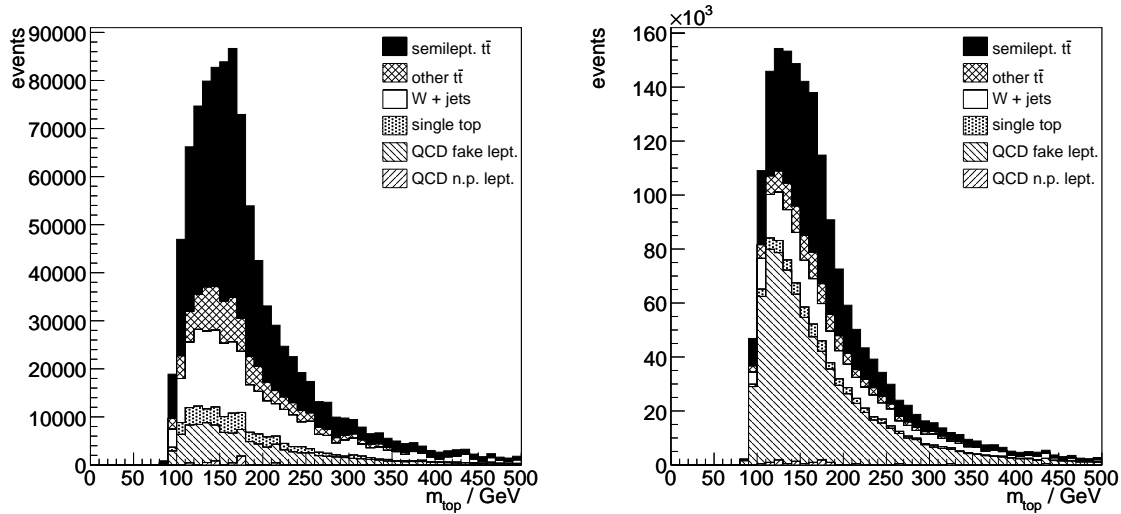
Figure 5.19: Stacked top mass distributions as reconstructed from the charged lepton, the neutrino plus the remaining jet with the highest transverse momentum. Again the plots are normalised for a fake electron probability of 10^{-3} and $10\,\mathrm{fb}^{-1}$ integrated luminosity. The left hand plot includes the cut on $\not{E}_T$ whereas the right hand plot does not.

vanishes. In the other cases, where two real solutions exist, the candidate with the smaller absolute value of the neutrino momentum z-component is chosen as it is typically the correct solution.

The Leptonic Top Quark

Now, with the z-component of the neutrino, it is possible to calculate the mass for the leptonic top decay. For this the 4-vectors of the charged lepton, the neutrino, plus the most energetic jet not used in the reconstruction of the hadronic top are chosen. Their invariant mass is calculated in analogy to the hadronic top mass. Figure 5.19 shows the distribution obtained this way, with the signal peaking close to the top mass. As for the hadronic top mass reconstruction no cut on m_{top} can be chosen to increase the selection significance as again the background also has a maximum in the region of the signal peak due to the previous event selection.

Top Mass Cross-Check

In principle one could use as a requirement for the jet selection and neutrino z-component solution that both the hadronic and leptonic top masses should yield about the same value. This is not done here as such a selection is affected by the jet energy scale because the decay branches have different jet multiplicities. However, as a cross check the difference between the reconstructed top masses is still valuable, revealing problems with any reconstructed object used in the semileptonic analysis. Figure 5.20 shows the distributions for the difference between the reconstructed hadronic and leptonic top masses. As expected, the signal events peak around zero. The distribution of background events is also enhanced for mass differences close to zero.

Even though a selection based on neither hadronic nor leptonic top masses improves the semileptonic cross section analysis the reconstruction of these objects still is a useful input for the compar-
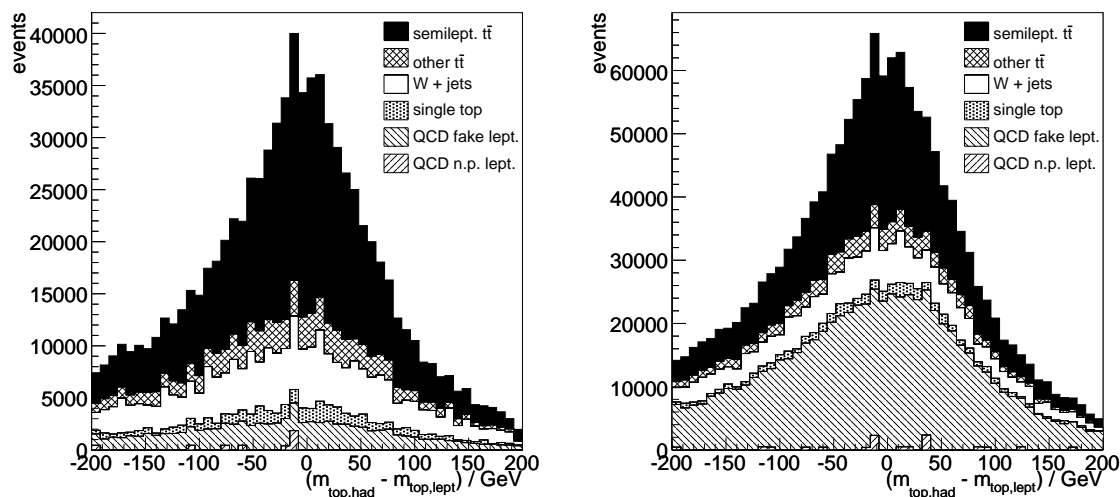
Figure 5.20: Stacked distributions of the difference between the reconstructed hadronic and leptonic top masses. The plots are normalised for a fake electron probability of 10^{-3} and $10\,\mathrm{fb}^{-1}$ integrated luminosity. The left hand plot includes the cut on $\not{E}_T$ whereas the right hand plot does not.

ison between the simulated events and real detector data when available, allowing for corrections in order to obtain a better agreement.

5.6 Topological and Other Variables

At the Tevatron collider topological variables, describing the shape of events, turned out to be quite powerful, e.g. combined to a likelihood parameter as for the D0 analysis in [49, 50]. Unfortunately these quantities lose most of their power when moving to the LHC collision energy. At the LHC top pairs are no longer produced close to the creation threshold, yielding events which are more strongly boosted than those observed at the Tevatron.

Other variables considered, but not used for analysis are the transverse W boson mass for the leptonic decay, the total energy or mass, and the angles between the jets and the beam direction in the decay rest frame. It was determined that none of these variables could be used to increase the selection significance. The distributions for these quantities are compiled in Appendix A.

5.7 Selection Efficiency and Cut Flow

In the previous section the individual analysis selections for the semileptonic channel have been presented. Here, as a conclusion before continuing with systematic studies, the total flow of the selection cuts is summarised. In addition to the selection significance the selection efficiencies as well as the total number of events are covered.

Figure 5.21 and Table 5.10 show the selection efficiencies after the individual selection steps for the signal and the background Monte Carlo samples. The errors given in the table are due to the finite statistics of the samples and are calculated as described in Appendix B. For those backgrounds

which consist of several individual samples the respective errors have been weighted according
to the sample scaling factors as specified in Appendix C. Except for the non-prompt leptons from
QCD and to a minor degree for the single top sample the uncertainty is two orders of magnitude
lower than the expectation value. The signal selection is visibly enhanced during the analysis cuts,
ending with around 21% efficiency for the signal and 5% or less for the background. The QCD fake
electron background is reduced by three orders of magnitude after the cut on missing transverse
energy and by more than two orders when excluding this last step.
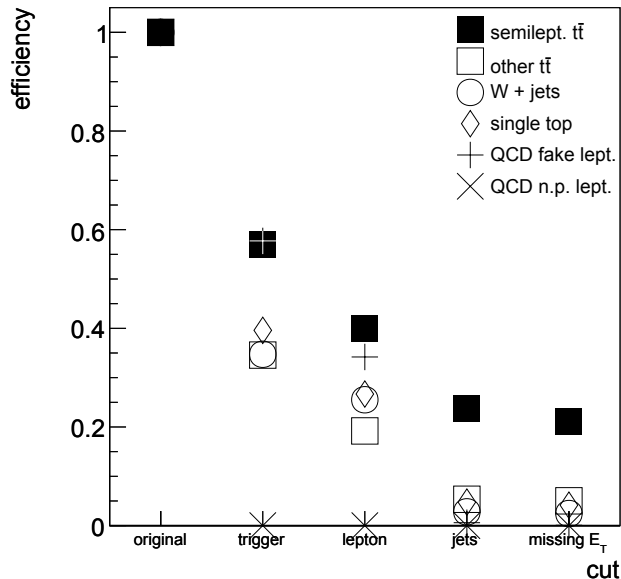
Figure 5.21: Accumulated efficiencies after each analysis cut. As smaller than the marker sizes the uncertainty on
the efficiency is not drawn but listed in Table 5.10 instead.

Figure 5.22 and Table 5.11 give the numbers of events as obtained from the selection efficiencies
above when normalising the Monte Carlo samples to an integrated luminosity of $10\,\mathrm{fb}^{-1}$ and a fake
electron probability of 10^{-3}. One notices the large number of QCD background events which the
selection eventually reduces to a manageable quantity. The drastic decrease of the non-prompt
fraction at the trigger level occurs as most events in the non-prompt sample have no leptons out-
side of the jet cones. For most of the backgrounds there is no single selection step of outstanding
importance. The impact of the lepton selection appears to be reduced only because the trigger
has already enriched the sample with good leptons. Nevertheless, especially for the fake leptons
from QCD, the jet selection has the largest relevance. The final cut on missing transverse energy
mainly suppresses the QCD background. In Table 5.11 the accumulated significance after each
selection step is also given. A continuous rise is observed except for the lepton selection where
exactly one lepton above $30\,\mathrm{GeV}$ was required. This drop in significance was accepted in order
to avoid the trigger turn-on region. The requirement of exactly one lepton is also crucial in order
to avoid including further backgrounds such as Z boson production with associated jets, which is
not considered in this study. The selection significance increases predominantly after the jet se-
lection. For fake rates of 10^{-3} as assumed here or less the cut on missing transverse energy can be
dispensed with if necessary, at the price of larger errors as will be seen in Section 6.6.

Sample	Cut 1: Trigger	Cut 2: Lepton
semileptonic $t\bar{t}$	0.5708 ± 0.0013	0.3992 ± 0.0012
other $t\bar{t}$	0.3458 ± 0.0013	0.1920 ± 0.0011
W+jets	0.3474 ± 0.0014	0.2552 ± 0.0014
single top	0.3959 ± 0.0030	0.2668 ± 0.0027
QCD fake leptons	0.5772 ± 0.0006	0.3419 ± 0.0006
QCD non-prompts	$9 \cdot 10^{-5} \pm 1 \cdot 10^{-5}$	$27 \cdot 10^{-7} \pm 8 \cdot 10^{-7}$

Sample	Cut 3: Jets	Cut 4: Missing E_T
semileptonic $t\bar{t}$	0.2378 ± 0.0011	0.2103 ± 0.0010
other $t\bar{t}$	0.0534 ± 0.0006	0.0503 ± 0.0006
W+jets	0.0280 ± 0.0005	0.0245 ± 0.0005
single top	0.0477 ± 0.0012	0.0414 ± 0.0012
QCD fake leptons	$595 \cdot 10^{-5} \pm 2 \cdot 10^{-5}$	$815 \cdot 10^{-6} \pm 6 \cdot 10^{-6}$
QCD non-prompts	$21 \cdot 10^{-8} \pm 7 \cdot 10^{-8}$	$8 \cdot 10^{-8} \pm 5 \cdot 10^{-8}$

Table 5.10: Accumulated efficiencies after the analysis cuts.
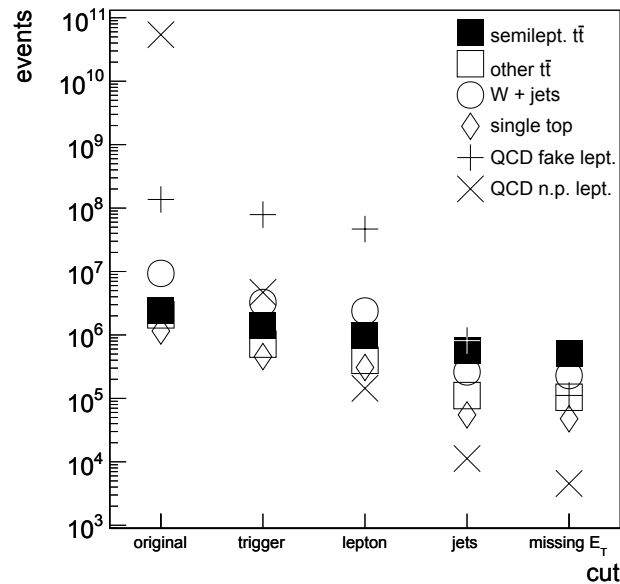
Figure 5.22: The number of events remaining after the analysis cuts for a fake electron probability of 10^{-3} and $10\,\text{fb}^{-1}$ integrated luminosity.

Sample	Original	Cut 1: Trigger	Cut 2: Lepton
semileptonic t$\bar{\text{t}}$	2 426 000	1 384 790	968 486
other t$\bar{\text{t}}$	2 072 000	716 420	397 828
W+jets	9 344 810	3 246 670	2 384 750
single top	1 151 000	455 726	307 033
QCD fake leptons	136 650 000	78 879 700	46 725 800
QCD non-prompts	54 090 000 000	4 686 500	144 016
significance	10.4	146.5	135.7

Sample	Cut 3: Jets	Cut 4: Missing E_T
semileptonic t$\bar{\text{t}}$	577 015	510 241
other t$\bar{\text{t}}$	110 748	104 209
W+jets	261 334	228 940
single top	54 915	47 734
QCD fake leptons	813 730	111 321
QCD non-prompts	11 266	4 547
significance	426.6	508.5

Table 5.11: Remaining events after the analysis cuts for a fake electron probability of 10^{-3} and $10\,\text{fb}^{-1}$ integrated luminosity.

Chapter 6

Studies of Systematic Uncertainties

The analysis presented in the previous chapter relied on a perfect understanding of the detector which, of course, cannot be expected in reality. In this chapter the influence of deviations from the simulation is studied for the semileptonic analysis.

6.1 Tests of Fake Lepton Assumptions

Up to this point it was assumed that the probability to fake an electron is identical for all jets. In reality one expects certain dependencies. Low energy jets should provoke fake electrons with a higher probability than highly energetic jets. The reason for this is that for small jets the relative energy depositions in the electromagnetic part of the calorimeter are subject to stronger fluctuations. E.g. a single pion decay within a low energy jet has a larger impact in a small than in a large jet. In [51] the p_T dependence of fake leptons has been examined on basis of the jets contained in the fully simulated $t\bar{t}$ sample which is also used in this thesis. The electrons were selected basically as in this thesis but with an additional energy isolation criterion[1]. Also the direction of the jet in the detector influences the fake electron probability as the calorimeter is not isotropic. Figure 6.1, taken from [51], shows the probability to observe an extra electron, i.e. either fake or non-prompt, for non-b jets. The rate has been studied as a function of the transverse jet momentum and the pseudorapidity. The event topology and kinematics of the QCD background differ from those of the $t\bar{t}$ events from which the distributions are obtained. Since, furthermore, the extra electrons examined include non-prompts and as the criterion for a good electron partially differs from the selection in this thesis the absolute fake probability results are not used in the following. Only the trend for highly energetic jets to produce fewer extra electrons is adopted. The η dependency is not followed up as the shape is likely to be dependent on the additional energy isolation requirement.

To study the influence of a fake rate as a function of p_T the following hypothesis for the fake probability p has been used:

$$p = p_0 \cdot \left(\frac{p_T}{\text{GeV}}\right)^c \tag{6.1}$$

where p_T is the transverse momentum of the reconstructed jet, $c < 0$ is a shape parameter and p_0

---

[1]Energy isolation of the leptons was not used in the selection here as the implementation in the ATHENA version used turned out to be incorrect.
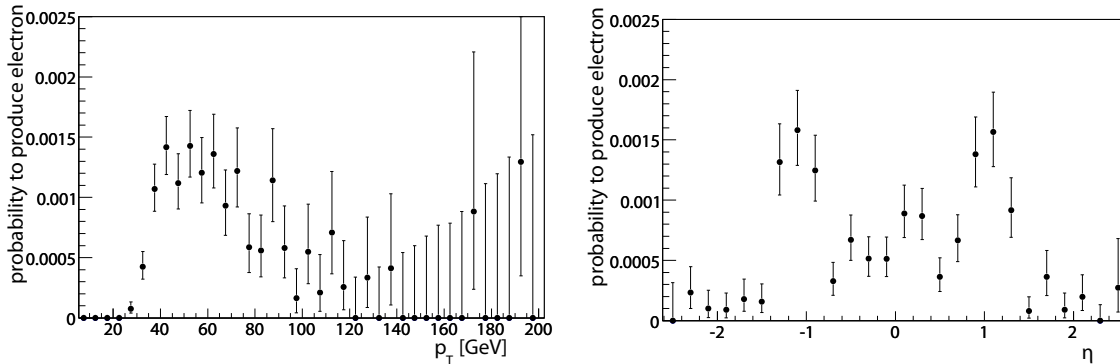
Figure 6.1: The probability for a jet to produce an extra electron (either fake or non-prompt) as a function of the transverse jet momentum (left) and pseudorapidity (right). The plots are taken from [51].

c	0.0	-0.25	-0.5	-0.75	-1.0
$\dfrac{p(p_T=100\,\mathrm{GeV})}{p(p_T=20\,\mathrm{GeV})}$	1.0	0.67	0.45	0.30	0.2

Table 6.1: Impact of the shape exponent c on the fake lepton transverse momentum distribution.

is a scaling constant which is chosen for the values of c such that the number of events before all selection cuts remains constant, i.e. the average fake rate is not altered.

In the following the values of -0.25, -0.5, -0.75, and -1.0 for the exponent c are considered. Table 6.1 shows the fake probability for 100 GeV jets as a fraction of the probability for 20 GeV jets, to give a feeling for the values chosen. In addition Figure 6.2 depicts the impact of the shape exponent on the fake lepton transverse momentum distribution. As expected the distribution becomes steeper for increasing absolute values of c as the low energy fakes are assigned higher weights than the fake electrons with large transverse momenta.

The impact on the cut flow from the previous Section 5.7 is illustrated in Figure 6.3. As expected the lepton selection has the strongest dependence on the exponent c as large absolute values of c emphasise the events with low energy fake leptons, which are less likely to survive the trigger and lepton selection. So the expected shape of the p_T dependence enhances the QCD background reduction and supports a constant fake rate as a conservative approach.

However, as the average fake rate is a parameter to be estimated from real data it is also important to look at the impact of the exponent c on the shape of the relevant histograms after the selection. A good understanding of these shapes in Monte Carlo samples helps when extracting the normalisation factor from real data.

Figure 6.4 shows the impact of c on the p_T distribution of the four leading jets after the lepton selection. The integrals of these plots have been normalised to unity for a better comparison of the shapes as the original normalisation is affected by the previous selection cuts. A small variation of the left edge of the spectrum occurs mainly for the leading jets. This effect is presumably caused by the fakes from low energy jets which, with their higher weight, emphasise the softer events. As a consequence the average transverse jet momenta are slightly reduced.

In Figure 6.5 the impact of the shape exponent c on the distribution of the missing transverse
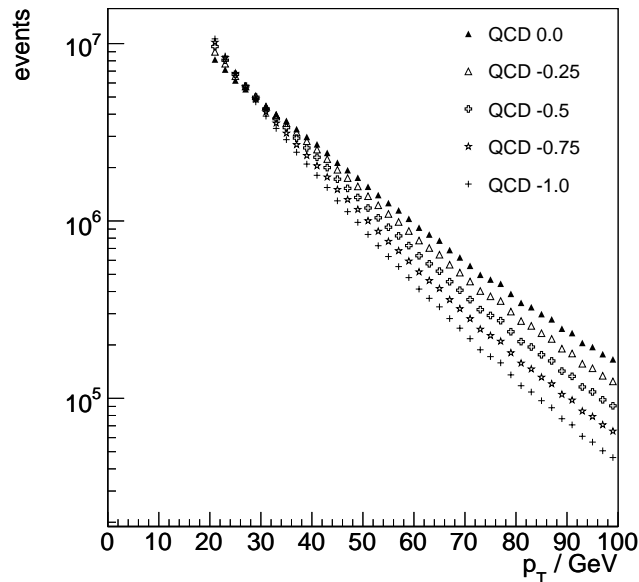
Figure 6.2: Impact of the shape exponent *c*, here in the range between 0.0 and -1.0, on the fake lepton transverse momentum distribution. The distributions have been normalised to the number of events before the trigger decision with a constant fake rate of 10^{-3} and $10\,\text{fb}^{-1}$ integrated luminosity as reference.

energy after the jet selection is depicted. Again the integrals are normalised to unity for a better comparison of the shape. Also here the main impact is visible for low energy events which are likely to have only a small reconstructed transverse energy and are likely to produce a fake electron at the same time. Nevertheless the impact is marginal and the shape quite robust.

The QCD background in the top mass distributions after the cut on missing transverse energy, as presented in Section 5.5, for different values of the parameter *c* is given in Figure 6.6 for the hadronic top and for the leptonic top in Figure 6.7. As for the previous plots the integrals are normalised to unity. Both top mass distributions are quite stable during the variation, especially the tail at high masses. Both edges at lower masses show a small deviation and are hence more exposed to the fake rate as a function of p_T.

6.2 Background Estimation from Data

For a precise cross section measurement the contributions from background processes must be well understood. Even with a perfect understanding of the respective selection efficiencies the production cross sections are still afflicted with uncertainties. At present the relative precision of the predictions for the non-QCD background contributions is in the order of 10%. The main source of uncertainties are the parton distribution functions extrapolated to the LHC energy. With the start of data taking at the LHC progress on this issue can be expected.

Independent from this the fake rate modelling of QCD will remain problematic. A direct comparison with Monte Carlo simulations is not possible due to the reasons outlined in Section 5.2.4. Hence it is desirable to extract the amount of QCD background events directly from real data.
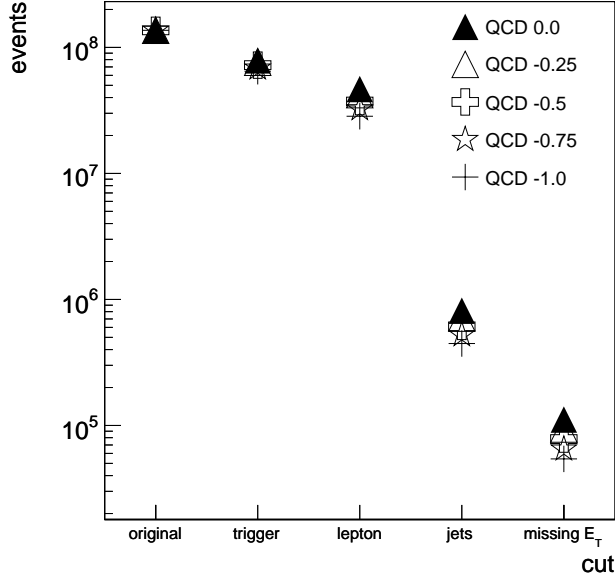
Figure 6.3: The number of events remaining after the analysis cuts for a fake electron probability of 10^{-3} and $10 \, \text{fb}^{-1}$ integrated luminosity. The shape exponent for the fake electrons as a function of p_T has been varied according to equation 6.1 in the range between 0.0 and -1.0.

6.2.1 QCD Background

In this thesis the normalisation of the QCD background is merely an estimate based on experience from the Tevatron. Also there it was not feasible to have a complete Monte Carlo description for the QCD. Instead, e.g. at D0, the number of QCD events after the event selection was estimated using the following approach [50]: the events taken from real data were classified as loose or tight, depending on the degree of isolation of the lepton. Apart from this the same selection cuts were made, so the tight lepton events are a subset of the loose selection and $N_{\text{loose}} > N_{\text{tight}}$. With $\varepsilon_{\text{non-QCD}}$ as the combined efficiency for the signal and the other backgrounds to pass the tight isolation cut after the signal selection and with ε_{QCD} denoting the tight isolation selection efficiency for the QCD events one gets

$$
\begin{aligned}
N_{\text{loose}} &= N_{\text{loose}}^{\text{QCD}} + N_{\text{loose}}^{\text{non-QCD}} \\
N_{\text{tight}} &= \varepsilon_{\text{QCD}} \cdot N_{\text{loose}}^{\text{QCD}} + \varepsilon_{\text{non-QCD}} \cdot N_{\text{loose}}^{\text{non-QCD}}
\end{aligned}
\tag{6.2}
$$

Solving these equations for $N_{\text{loose}}^{\text{QCD}}$ and $N_{\text{loose}}^{\text{non-QCD}}$ yields

$$
\begin{aligned}
N_{\text{loose}}^{\text{QCD}} &= \frac{\varepsilon_{\text{non-QCD}} \cdot N_{\text{loose}} - N_{\text{tight}}}{\varepsilon_{\text{non-QCD}} - \varepsilon_{\text{QCD}}} \\
N_{\text{loose}}^{\text{non-QCD}} &= \frac{N_{\text{tight}} - \varepsilon_{\text{QCD}} \cdot N_{\text{loose}}}{\varepsilon_{\text{non-QCD}} - \varepsilon_{\text{QCD}}}
\end{aligned}
\tag{6.3}
$$

which could be translated into the fake rate using the QCD multijet production cross sections from the Monte Carlo generator. The detailed error calculation for the resulting equations 6.3 is given
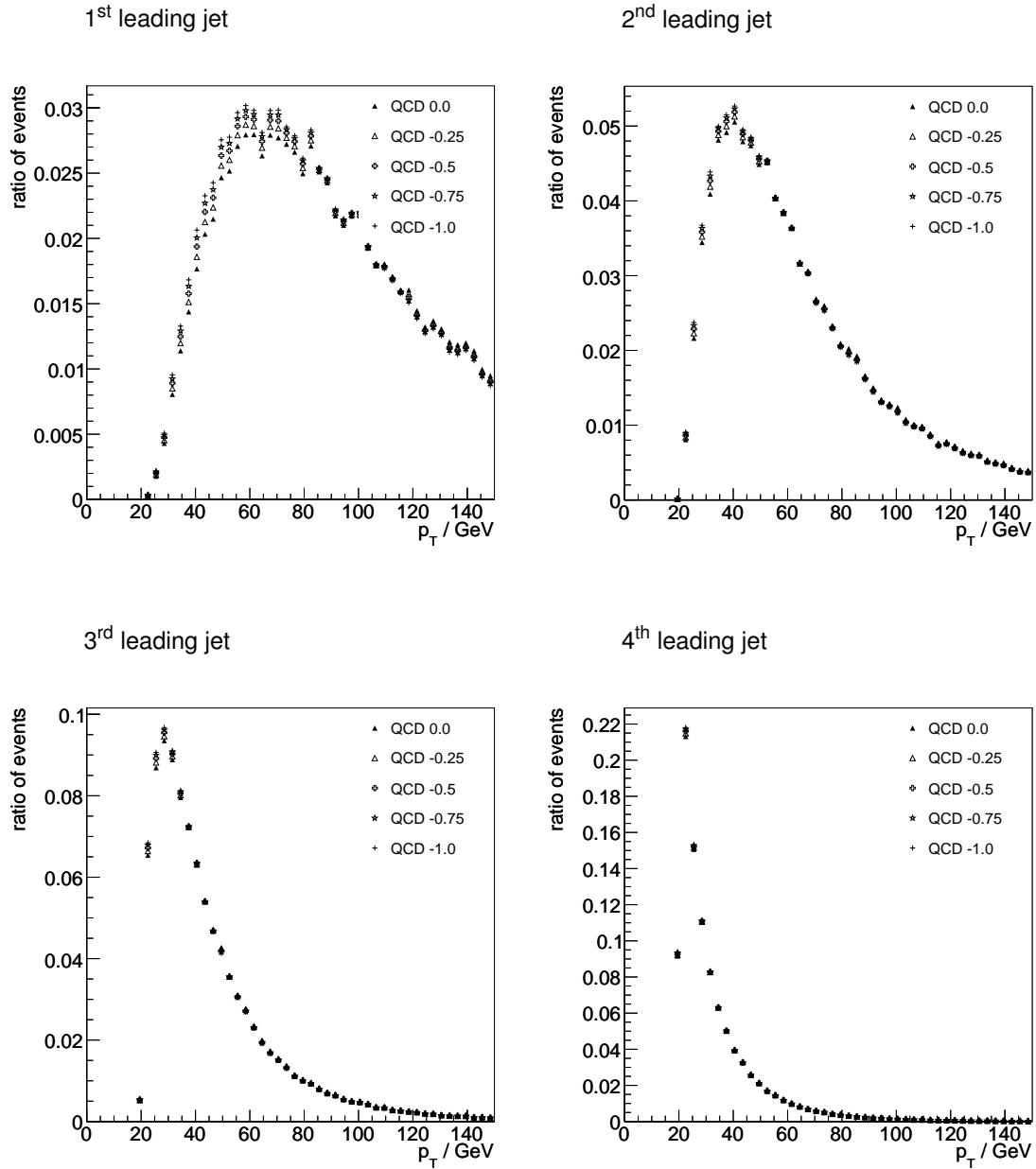
Figure 6.4: The normalised shapes of the four leading jet transverse momentum distributions after the lepton selection. A non-constant fake rate, as modelled with the shape parameter in the range between 0.0 and -1.0, enhances the lower energetic edge, in particular for the highest energetic jets.
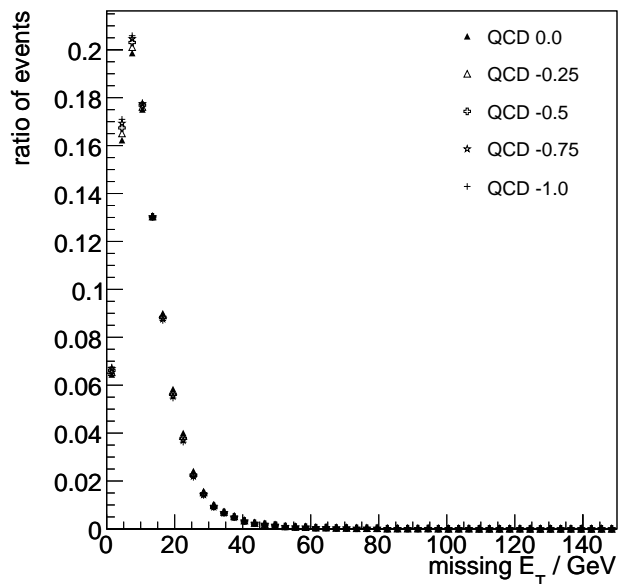
Figure 6.5: The normalised shapes of the missing transverse energy distribution after the jets selection. A non-constant fake rate, as modelled by a parameter varied between 0.0 and -1.0, slightly enhances the lower energetic edge.
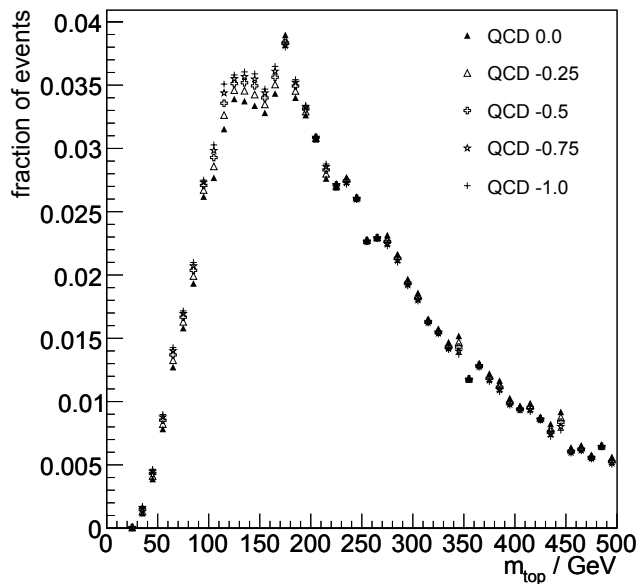
Figure 6.6: The normalised shapes of the hadronic top mass distribution after the cut on missing transverse energy. A non-constant fake rate, here with shape parameters between 0.0 and -1.0, slightly affects the region at low invariant masses.
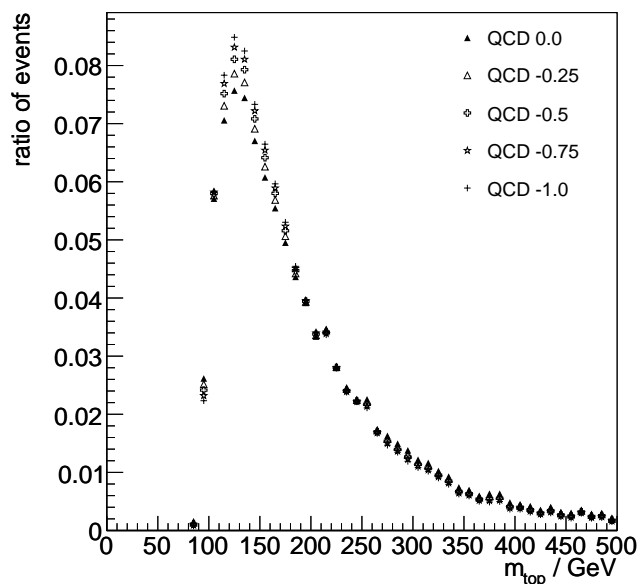
Figure 6.7: The normalised shapes of the leptonic top mass distribution after the cut on missing transverse energy. A non-constant fake rate, here with shape parameters between 0.0 and -1.0, slightly affects the region at low invariant masses.

in [52]. Neglecting the uncertainty and systematics of the efficiencies ε_{QCD} and $\varepsilon_{\text{non-QCD}}$ the error on $N_{\text{tight}}^{\text{QCD}} = \varepsilon_{\text{QCD}} \cdot N_{\text{loose}}^{\text{QCD}}$ is given by

$$
\Delta N_{\text{tight}}^{\text{QCD}} = \left(\left(\frac{\varepsilon_{\text{QCD}} \cdot \varepsilon_{\text{non-QCD}}}{\varepsilon_{\text{non-QCD}} - \varepsilon_{\text{QCD}}} \right)^2 (N_{\text{loose}} - N_{\text{tight}}) + \left(\frac{\varepsilon_{\text{QCD}} \cdot (1 - \varepsilon_{\text{non-QCD}})}{\varepsilon_{\text{non-QCD}} - \varepsilon_{\text{QCD}}} \right)^2 N_{\text{tight}} \right)^{\frac{1}{2}}
\tag{6.4}
$$

As the ATLFAST simulation of the QCD sample does not include the necessary lepton isolation information the precision of this method remains to be examined with real data.

Nevertheless, as a substitute for this method, it is possible to vary the ratio of QCD events by means of variables other than the lepton isolation. Even though these alternatives might not yield the same precision as the isolation approach or might turn out to be dominated by systematic errors they should give a feeling for the scale of the achievable statistical precision.

As a cut on missing transverse energy powerfully discriminates between QCD and the other samples, and as the missing transverse energy turned out to be robust when comparing non-constant fake rate scenarios one might consider using this quantity to estimate the amount of QCD background as an alternative to the lepton isolation. Calculating the uncertainty using equation 6.4, with the events before the cut on E_T treated as loose and the passing events as tight, yields 0.13% relative statistical precision for the amount of QCD background at a real fake rate of 10^{-3} and $10\,\text{fb}^{-1}$ integrated luminosity. As the understanding of missing transverse energy will not reach this level of precision systematic errors have to be examined thoroughly to estimate the fraction of

QCD background.

Other distributions which are little affected by non-constant fake rates are the top mass distributions, which can be split into a region where the signal and non-QCD backgrounds dominate and the remaining range where the signal is less influential. Here for the hadronic mass (see Figure 5.17) the interval between 110 GeV and 220 GeV is used. Estimating the QCD background from the hadronic mass might be useful if the systematic error on missing transverse energy is too large to be used. For a real fake rate of 10^{-3} the relative statistical precision for the QCD background drops to 0.92%. Though one loses the systematic error on missing transverse energy it is necessary to recall that the shapes in the top mass distributions are also subject to systematic uncertainties.

6.2.2 Lepton Charges in W+Jets and Single Top

Not only the simulated QCD background has to be normalised to real data. The cross sections of the other backgrounds are also prone to errors and require a comparison with real data, similar to the procedure for the QCD fraction. As these normalisations need detailed studies with real data and since precise predictions for the achievable accuracy are presently not possible this issue will not be treated here in detail. It is assumed that a good understanding of the shapes of the distributions will be important and for this reason the following thoughts might be helpful.

As the LHC is a proton-proton collider more up-type than down-type quarks should be involved in the collisions. As a consequence more W^+ than W^- bosons are produced and hence more positively than negatively charged leptons must be created in the leptonic decays. For the $t\bar{t}$ decays no asymmetry is expected as here the W bosons do not relate to the partons in the proton. Also the QCD fake leptons should not favour a type of charge, so a random charge of ± 1 was chosen for them. For both the W+jets and the single top background[2], however, an asymmetry of the lepton charge should be observable. Figure 6.8 shows the number of events with a positively or negatively charged lepton after the event selection. The number of events with positive leptons is significantly enhanced due to the W+jets and single top contributions. Other differences are within the statistical fluctuations of the samples used.

Trusting in the ratio derived from the Monte Carlo samples, the number of W+jets and single top events can be extracted as long as the normalisation uncertainties of both backgrounds are strongly correlated. As such a correlation is primarily obvious for the contribution of the parton density functions both backgrounds have to be disentangled. For this purpose a distribution with differing shapes for the W+jets and the single top backgrounds has to be chosen. To statistically remove the signal events and other backgrounds, the histogram entries can be weighted with the charge of the reconstructed lepton since the W+jets and the single top samples scale with the number of events n whereas the fluctuations of the other channels have a $\sqrt{n}$ dependence. So with enough statistics a disentangling analogous to the approach for the QCD background might be possible.

To illustrate the method Figure 6.9 shows the hadronic top distribution with charge weighted entries. Even with the limited statistics of the samples available the emergence of the W+jets background is visible, allowing assessment of the W+jets background shape under the top peak.

Following this approach the systematics of the lepton charge ratios as obtained from the simulations have to be examined. In particular the impact of a variation of the parton density functions must be tested as well as the probability for charge misidentification by the detector. Nevertheless

---

[2]The asymmetry should occur in the s-channel and the t-channels but not in the Wt-channel.
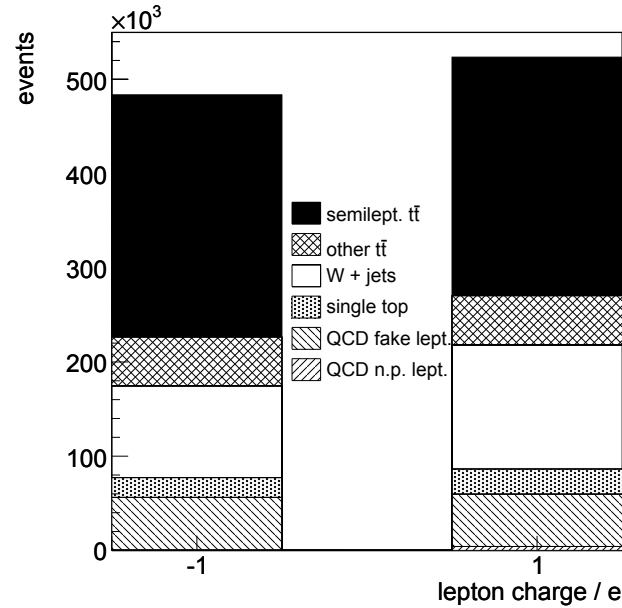
Figure 6.8: Events after the analysis cuts split by the charge of the reconstructed lepton. Only for the W+jets and single top samples is a significant excess of positive leptons observed. Applied are a fake electron probability of 10^{-3} and $10\,\text{fb}^{-1}$ integrated luminosity.
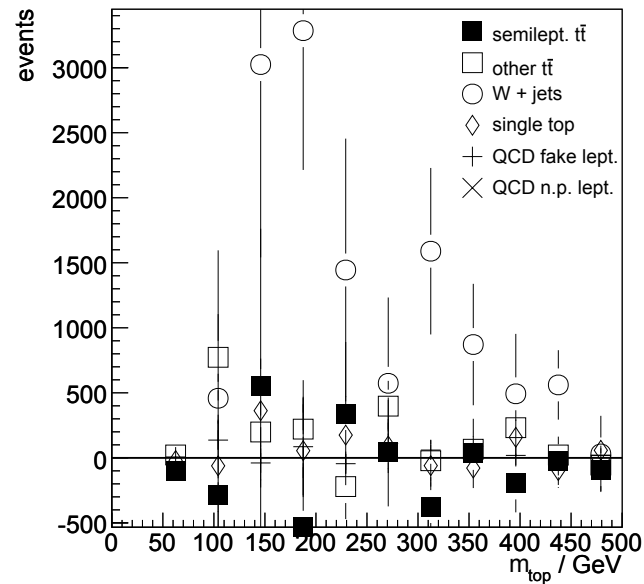
Figure 6.9: Top mass distributions with lepton charge weighted entries, normalised to $10\,\text{fb}^{-1}$ integrated luminosity. For the $t\bar{t}$ and QCD samples only statistical fluctuations occur while the W+jets dominate the distribution.

charge weighting of the events in the semileptonic $t\bar{t}$ analysis should at least allow for a cross check between simulation and data.

6.3   Scenario with a Reduced Detector Resolution

The semileptonic $t\bar{t}$ analysis depends largely on the jet resolution which, apart from the jet selection, also has an impact on the cut on missing transverse energy. In this section the sensitivity of the semileptonic $t\bar{t}$ analysis to scenarios with a reduced jet energy resolution is studied.

The resolution of the ATLAS calorimeter aims for

$$\frac{\Delta E}{E} = \frac{0.5}{\sqrt{E/\text{GeV}}} \oplus 0.03 \tag{6.5}$$

for hadronic jets in the central region of the detector. Especially during the early phase of ATLAS the energy resolution of the calorimeter may be lower than expected if the calibration process is not yet complete. To study the impact of such scenarios the measured energies and momenta have been smeared in addition to the detector simulation with Gaussian distributions of width

$$\sigma_E = c \cdot \sqrt{E} \tag{6.6}$$

In doing so the jet directions have been kept constant. Figure 6.10 shows the jet energy resolution $\sigma(\Delta E)$, where ΔE is the difference between the jet energies reconstructed from truth particle jets and from detector jets, as a function of the energy of the truth particle jet. The smearing constant c has been varied in the range from $0/\sqrt{\text{MeV}}$ up to $50/\sqrt{\text{MeV}}$ in $5/\sqrt{\text{MeV}}$ steps. The average resolution increases from $11.3\,\text{GeV}$ with no additional smearing to $19.3\,\text{GeV}$ at $c = 50/\sqrt{\text{MeV}}$. Figure 6.11 shows the dependence of the average jet resolution as a function of the smearing constant c. As the resolutions of the original detector simulation and the additional smearing add quadratically, the original resolution dominates for small values of c whereas for larger choices of c the smearing term becomes significant. At about $c = 35/\sqrt{\text{MeV}}$ the original and the additional smearing contribute equally.

Figure 6.12 shows the jet selection significance after the cuts are applied on the number of jets with p_T above $20\,\text{GeV}$ and the number of jets over $40\,\text{GeV}$, once without any additional smearing and as an example also for $c = 35/\sqrt{\text{MeV}}$. Over the whole c variation interval the optimum selection remains to demand at least 4 jets above $20\,\text{GeV}$, two of which exceed $40\,\text{GeV}$. The selection significance after this selection step drops from initially 427 to 417 at $c = 50/\sqrt{\text{MeV}}$, see Figure 6.13. So the jet selection will not need to be altered in case of a reduced jet energy resolution.

As the missing transverse energy is calculated from the measured momentum balance, a reduced jet energy resolution should also be reflected by a lessened $\not{E}_T$ precision. For a respective correction the originally reconstructed value for $\not{E}_T$ was shifted according to the vectorial difference of the jets caused by the smearing. Also the detected transverse energy which did not contribute to any reconstructed jet, i.e. the difference between the transverse vector sum of the reconstructed physics objects and the reconstructed missing transverse energy, was smeared according to equation 6.6 and used for the correction. Figure 6.14 shows the original $\not{E}_T$ distribution in comparison to the distribution obtained for $c = 35/\sqrt{\text{MeV}}$. Especially for the QCD a substantial broadening of the peak can be seen. Figure 6.13 shows the selection significance after the standard cut on missing transverse energy as well as the significance achieved after an optimisation of the cut on $\not{E}_T$ for
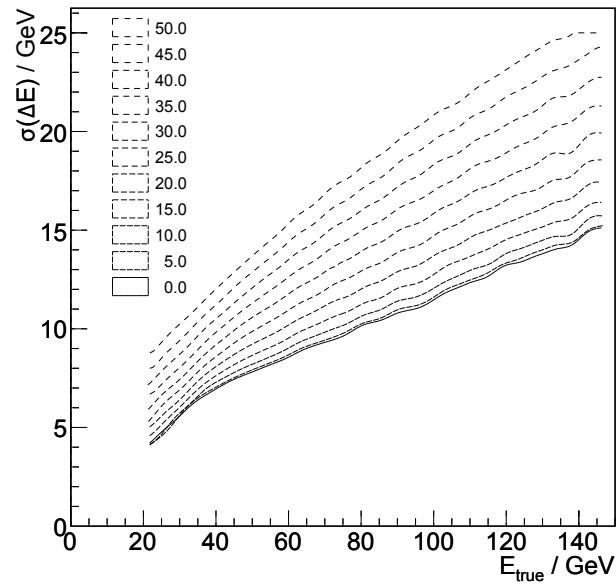
Figure 6.10: The resolution of the difference between the jet energies reconstructed from true jets minus the energies of the matched detector jets as a function of the true jet energy. The smearing constant c has been varied in the range from $0/\sqrt{MeV}$ up to $50/\sqrt{MeV}$ in $5/\sqrt{MeV}$ steps.
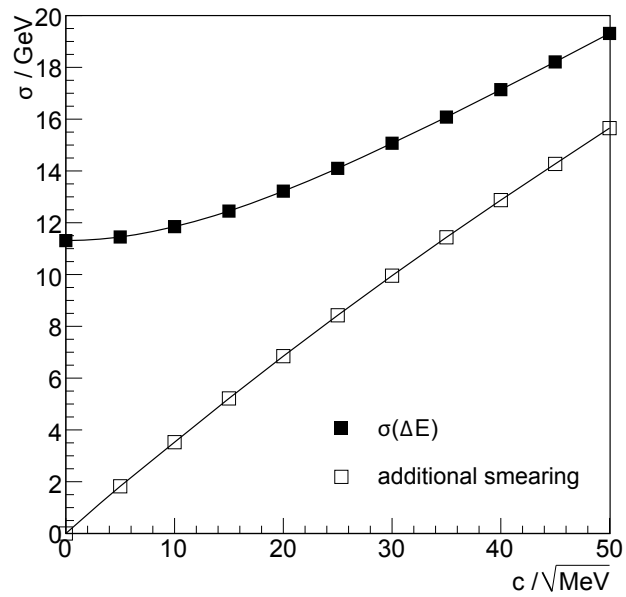
Figure 6.11: The total jet energy resolution $\sigma(\Delta E)$ and the contribution of the additional smearing as a function of the smearing constant c.
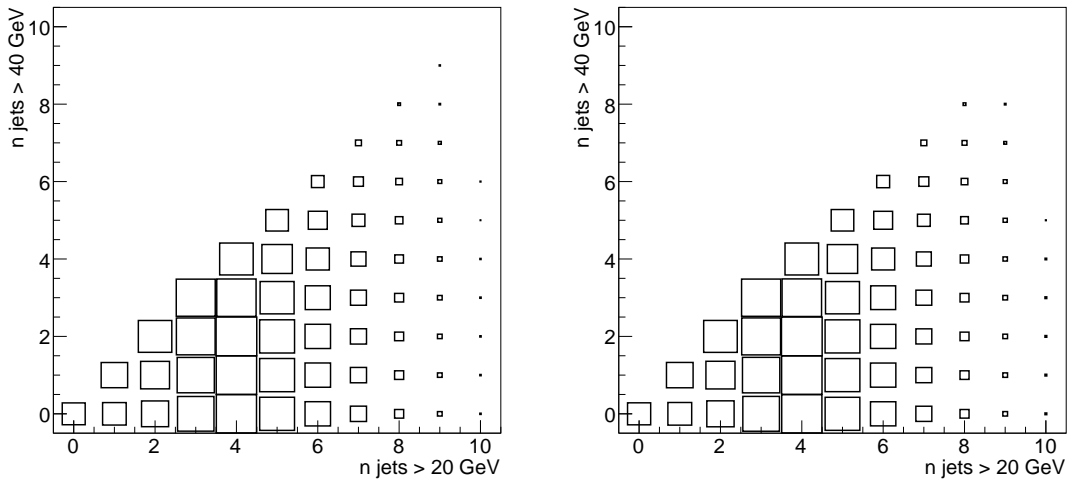
Figure 6.12: Significance of a combination of cuts on number of jets with $p_T > 20$ GeV and the number of jets with $p_T > 40$ GeV. The left plot is the result after the detector simulation only whereas for the right plot an additional smearing with $c = 35/\sqrt{MeV}$ was applied. The best selection cut remains unchanged, requiring 4 jets above 20 GeV of which 2 jets exceed 40 GeV.
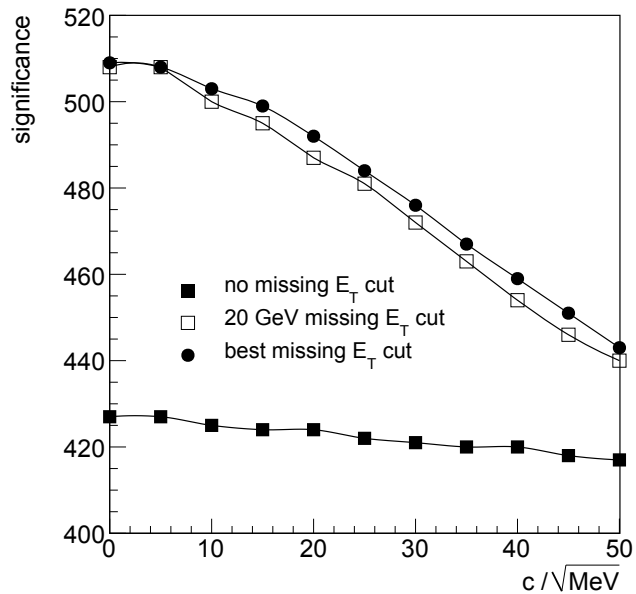
Figure 6.13: The selection significance without the cut on $\not{E}_T$, the selection significance including the cut on $\not{E}_T$, and a significance using the optimum $\not{E}_T$ cut. All graphs are plotted as functions of the smearing constant c.

the respective value of c. Apparently the cut on $\not{E}_T$ is affected more by an additional smearing of the jets than the previous cuts on the jet momenta and even a re-optimisation of the $\not{E}_T$ cut[3] can only slightly compensate for this. The analysis without the final cut on missing transverse energy remains more stable in scenarios with a less than expected energy resolution.
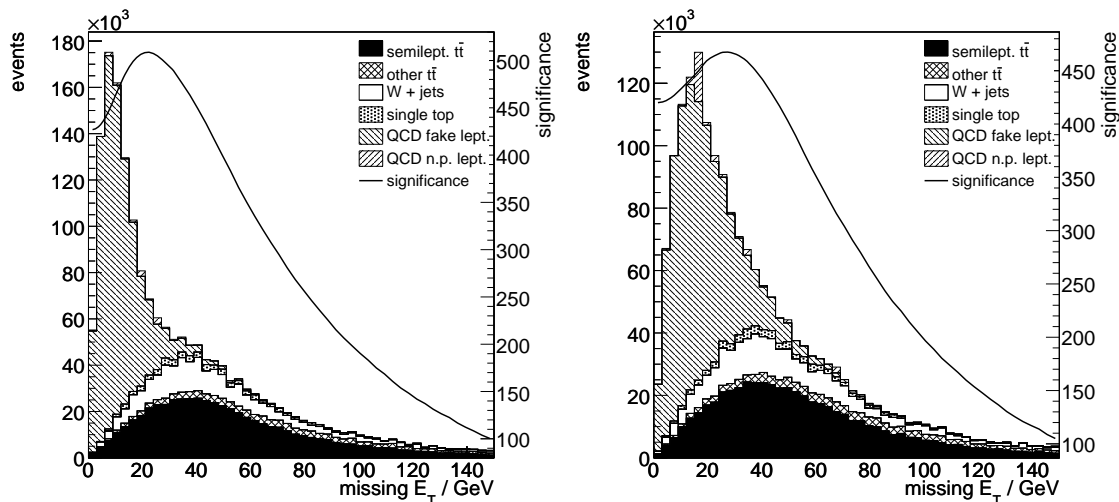
Figure 6.14: The original missing transverse energy distributions after the jet selection (left) compared to the same distribution after an additional smearing according to equation 6.6 with $c = 35/\sqrt{\text{MeV}}$ (right). As before, the line indicates the significance of a cut and the histograms are normalised to a constant fake electron probability of 10^{-3} and $10\,\text{fb}^{-1}$ integrated luminosity.

6.4 Impact of the Jet Energy Scale

Not only the width but also the central value of the jet energy measurement may be affected by additional uncertainties during the early phase of ATLAS. During this time the jet energy scale will probably not be understood as well as predicted by the detector simulations. As a first approximation the measured jet energies might vary by a constant factor from the correct values. In the early phase of ATLAS an uncertainty on the jet energy scale of about 5% is expected [41]. Figure 6.15 shows the influence of a jet energy scale variation in the range between 0.9 and 1.1 corresponding to $\pm 2.5\%$, $\pm 5\%$ and $\pm 10\%$ deviation. Plo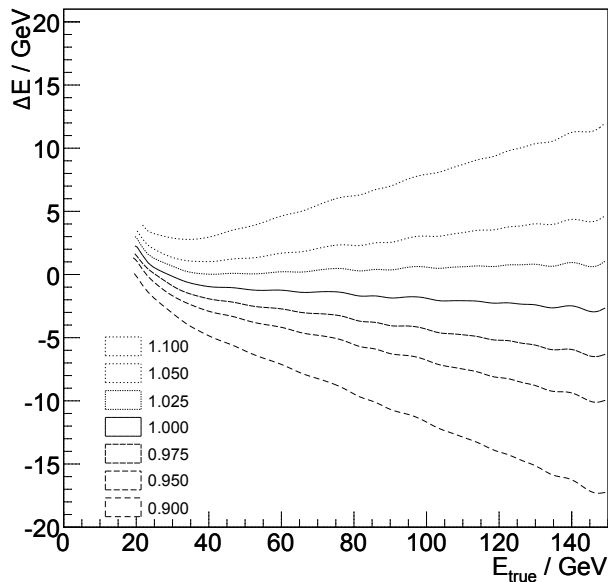tted is the deviation ΔE between the jet energy as reconstructed from the detector simulation and the true jet as a function of the energy of the true jet. The slopes reflect the scale factors. The slight asymmetry of these slopes, ignoring the curvature at low energies caused by the jet selection threshold, is due to the imperfect original scaling of the reconstructed jets whose energies already seem to be underestimated by about 2%.

Figure 6.16 depicts the influence of the jet energy scale on the selection significance of the analysis with and without the cut on missing transverse energy. For scale factors below 1.0 the significance drops as in this case events which were meant to be cut away now survive the selection. In the other case with a scale factor above 1.0 the impact on the selection significance is lower, as here the number of selected events is reduced but the ratio between signal and background remains relatively stable. Evidently a selection including a cut on $\not{E}_T$ depends more strongly on the knowledge

---

[3]The cut on missing transverse energy rises from $20\,\text{GeV}$ for $c = 0/\sqrt{\text{MeV}}$ to $27\,\text{GeV}$ for $c = 50/\sqrt{\text{MeV}}$.

Figure 6.15: The deviation ΔE between the jet energy as reconstructed from the detector simulation and the true jet as a function of the energy of the true jet. The jet energy scale factor has been varied between 0.9 and 1.1. The slopes of the curves correspond to the respective scale factors whereas the curvature at low energies is caused by the jet selection threshold, which suppresses negative fluctuations of ΔE.

Scale Uncertainty	$\pm 2.5\%$	$\pm 5\%$	$\pm 10\%$
Error Contribution with $\not{E}_T$ Cut	0.8%	2.2%	6.1%
Error Contribution without $\not{E}_T$ Cut	0.7%	1.2%	3.0%

Table 6.2: Translation of the relative jet energy scale uncertainty to the relative uncertainty of the selection significance. The absolute uncertainty on the values is about 0.3%.

of the jet energy scale as here the uncertainties associated with the direct cuts on the transverse jet momenta and the cut on missing transverse energy, which also depends on the scale factor, accumulate.

The deviation of the significance from the original value as a consequence of the systematic uncertainty on the scaled jet energy can be translated into a corresponding systematic error on the selection significance. Table 6.2 gives these systematic errors for scenarios with jet energy scale precisions of $\pm 2.5\%$, $\pm 5\%$ and $\pm 10\%$. As the curves in Figure 6.16 are asymmetric the left shoulders have been chosen for a conservative calculation. So a scenario with $\pm 5\%$ energy scale uncertainty contributes about 2.2% error on the significance in case of the complete analysis selection and 1.2% error for an analysis which does not rely on the cut on missing transverse energy.
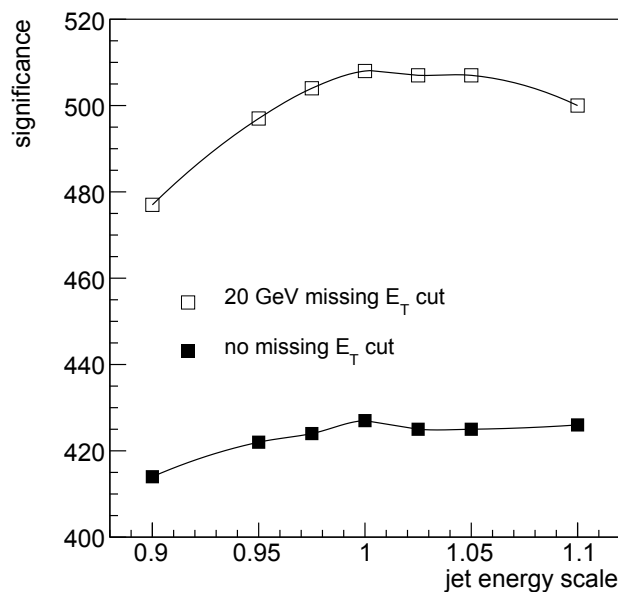
Figure 6.16: The impact of the jet energy scale factor on the significance of the complete analysis selection and a selection without the cut on $E̸_T$. As before the values are calculated for a constant fake electron probability of 10^{-3} and $10\,\text{fb}^{-1}$ integrated luminosity.

6.5 Fake Electron Scale Factor

At present it is unclear whether the energies measured for fake electrons are biased due to the jet misinterpretation. Figure 6.17 exhibits the difference measured for the transverse energy between calorimeter clusters originating from a real electron when reconstructed either as an electron or a jet[4]. This discrepancy factor, which peaks at 1.16, originates from different calibrations applied during reconstruction of electron and jet energies. Event though it is unclear if this factor is still applicable for fake electrons the impact of a correction according to

$$E_{T,\text{electron}} = \frac{E_{T,\text{jet}}}{1.16}$$
(6.7)

has been studied. The transverse momentum has been reduced by the same factor, leading to fewer fake electrons passing the $p_T > 30\,\text{GeV}$ lepton selection threshold. Figure 6.18 compares the normalised lepton transverse momentum distributions with and without the application of the scaling factor. The curve with the factor drops more quickly than the original one as the correction implies a larger absolute reduction for highly energetic fake electrons.

Table 6.3 shows the impact of the scaling on the total selection significance and on the selection efficiency of the QCD fake electron background. As with the correction factor applied fewer QCD events pass the cut on the transverse momentum, the significance increases by 0.6% for the complete analysis and by 2.8% for an analysis without the $E̸_T$ cut.

As long as a scale factor for fake electrons only affects the normalisation of the distributions that

---

[4]Jets reconstructed from electromagnetic showers are normally eliminated during the TOPVIEW overlap removal.
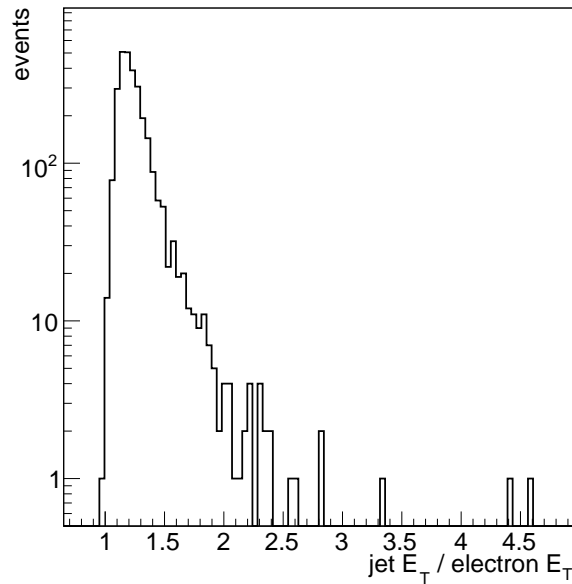
Figure 6.17: The ratio between the transverse energy of a true electron if reconstructed as a jet and the transverse energy when interpreted correctly as an electron [53].
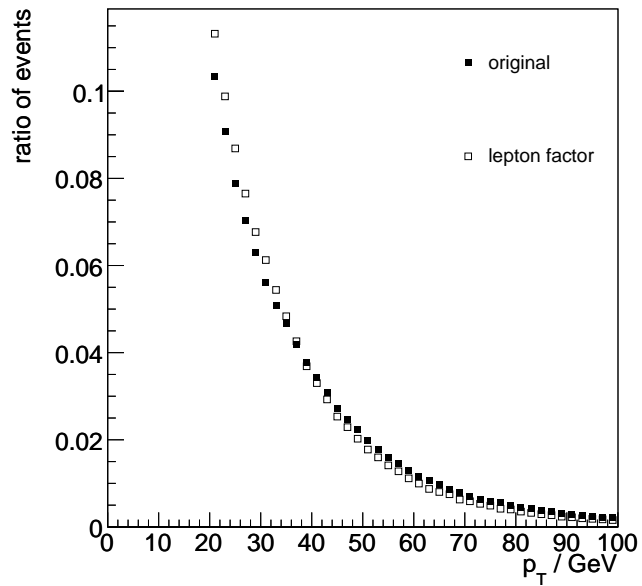
Figure 6.18: Distribution of the transverse momentum of the fake electron once without and once with a scale factor of 1/1.16 applied. For a better comparison of the shapes both integrals are normalised to unity.

	Significance	
	With $\not{E}_T$ Cut	Without $\not{E}_T$ Cut
unscaled fakes	508	427
scaled fakes	511	439

	Selection Efficiency	
	With $\not{E}_T$ Cut	Without $\not{E}_T$ Cut
unscaled fakes	$815 \cdot 10^{-6} \pm 6 \cdot 10^{-6}$	$595 \cdot 10^{-5} \pm 2 \cdot 10^{-5}$
scaled fakes	$744 \cdot 10^{-6} \pm 6 \cdot 10^{-6}$	$523 \cdot 10^{-5} \pm 2 \cdot 10^{-5}$

Table 6.3: Impact of a scale factor according to equation 6.7 on the selection significance (for a constant fake electron probability of 10^{-3} and $10\,\mathrm{fb}^{-1}$ integrated luminosity) and the selection efficiency of the QCD background. Scenarios with and without the cut on missing transverse energy have been considered.
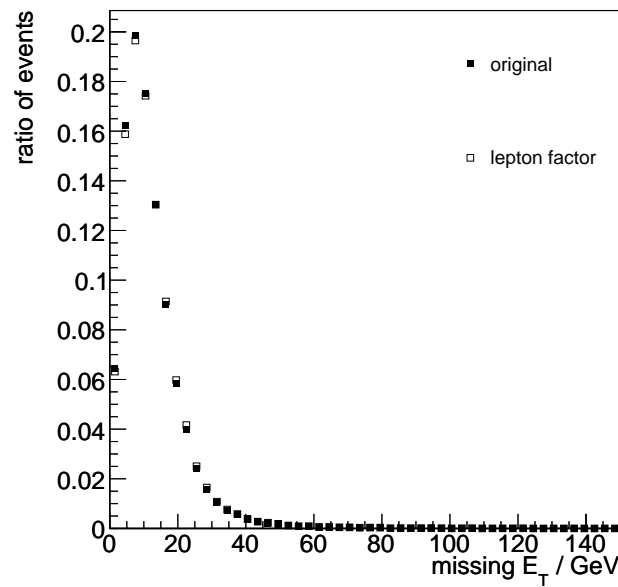
Figure 6.19: Comparison between the transverse energy of a true electron if reconstructed as a jet and the transverse energy when interpreted correctly as an electron. Both distributions are normalised to unity.

were cut, but not the shapes, the impact on the analysis steps following the lepton selection can be neglected. Figure 6.19 shows the influence on missing transverse energy caused by the lepton scaling factor. Only a small deviation for low amounts of $\not{E}_T$ can be observed. Figure 6.20 shows the influence of the QCD fake lepton contribution on the top mass plots. The distribution for the hadronic top varies less than the statistical fluctuations of the Monte Carlo samples and also the QCD background for the leptonic top is only slightly affected even though the lepton is used directly in the calculation. So the influence of a possible fake lepton scale factor on the systematic uncertainties seems to be low and will be neglected as the QCD will be normalised using data.
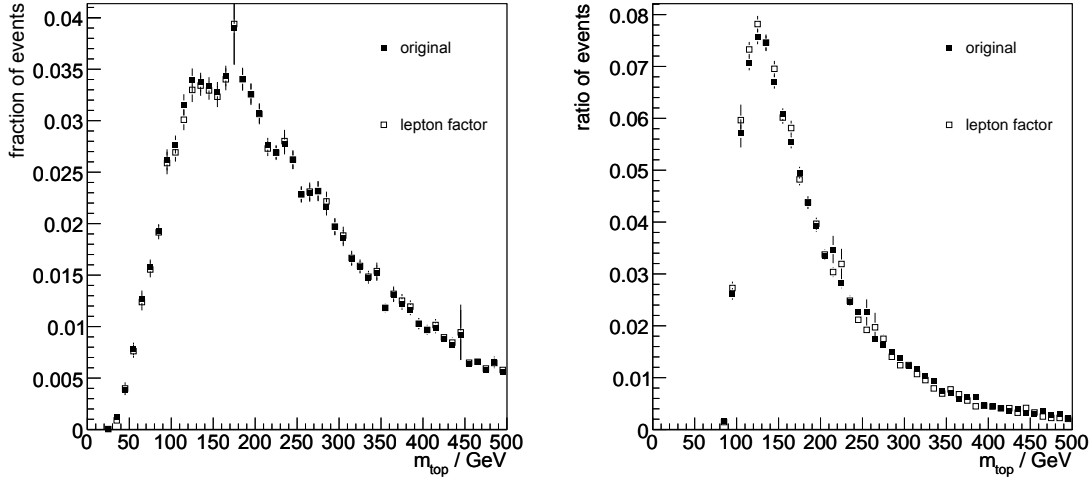
Figure 6.20: Impact of the fake lepton scale factor for the QCD background on the hadronic top mass (left) and the leptonic top mass (right). All distributions are normalised to unity.

6.6 Estimated Cross Section Precision

The signal cross section σ will be calculated according to

$$\sigma = \frac{N - \varepsilon_{\mathrm{b}} \sigma_{\mathrm{b}} L}{\varepsilon_{\mathrm{s}} L} \tag{6.8}$$

where N is the number of events measured after the selection, ε_{s} and ε_{b} are the signal and background efficiencies as estimated from Monte Carlo studies, assured via comparisons with real data later in experiment, σ_{b} is the background cross section, and L the integrated luminosity. The term $\varepsilon_{\mathrm{b}} \sigma_{\mathrm{b}}$ can be expressed as a sum of individual contributions i from the background samples via

$$\varepsilon_{\mathrm{b}} \sigma_{\mathrm{b}} = \sum_i \varepsilon_{\mathrm{b},i} \sigma_{\mathrm{b},i} \tag{6.9}$$

The precision for σ is limited by the combination of statistical and systematic errors plus the uncertainty on the integrated luminosity. The statistical error on the cross section is given by

$$(\Delta\sigma)_{\mathrm{stat}} = \frac{\sigma}{S} \tag{6.10}$$

with significance S. For an analysis at $10\,\mathrm{fb}^{-1}$ integrated luminosity and $\sigma = 242\,\mathrm{pb}$ this results in $(\Delta\sigma)_{\mathrm{stat}} = 0.47\,\mathrm{pb}$ for the analysis with the $\not{E}_T$ cut and $(\Delta\sigma)_{\mathrm{stat}} = 0.57\,\mathrm{pb}$ without this cut.

The systematic errors due to the limited Monte Carlo statistics, derived from equation 6.8, are

$$(\Delta\sigma)_{\mathrm{MC,s}} = \frac{\partial\sigma}{\partial\varepsilon_{\mathrm{s}}} \Delta\varepsilon_{\mathrm{s}} = \frac{N - \varepsilon_{\mathrm{b}} \sigma_{\mathrm{b}} L}{\varepsilon_{\mathrm{s}}^2 L} \Delta\varepsilon_{\mathrm{s}} \tag{6.11}$$

and

Sample	With $\not{E}_T$ Cut	Without $\not{E}_T$ Cut
other $t\bar{t}$	0.59 pb	0.52 pb
W+jets	2.23 pb	1.96 pb
single top	0.66 pb	0.58 pb
QCD fake leptons	0.39 pb	1.15 pb
QCD non-prompts	1.29 pb	1.59 pb
$(\Delta\sigma)_{\mathrm{MC,b}}$	2.75 pb	2.88 pb

Table 6.4: Contributions to the total systematic uncertainty of the cross section due to the impact of the limited statistics of the Monte Carlo samples on the background selection efficiencies.

$$(\Delta\sigma)_{\mathrm{MC,b}} = \frac{\partial\sigma}{\partial\varepsilon_{\mathrm{b}}}\Delta\varepsilon_{\mathrm{b}} = \frac{\sigma_{\mathrm{b}}}{\varepsilon_{\mathrm{s}}}\Delta\varepsilon_{\mathrm{b}} \tag{6.12}$$

which gives for the analysis with the cut on missing transverse energy $(\Delta\sigma)_{\mathrm{MC,s}} = 1.16$ pb and $(\Delta\sigma)_{\mathrm{MC,b}} = 2.75$ pb. For the calculation of the latter value the contributions from the individual background samples have been added quadratically. The analysis without the $\not{E}_T$ cut yields $(\Delta\sigma)_{\mathrm{MC,s}} = 1.12$ pb and $(\Delta\sigma)_{\mathrm{MC,b}} = 2.88$ pb. Table 6.4 lists the separate contributions of the individual backgrounds to the error due to the Monte Carlo statistics according to equation 6.12.

The uncertainty associated with the background cross section propagates into the signal cross section according to

$$(\Delta\sigma)_{\mathrm{CS}} = \frac{\partial\sigma}{\partial\sigma_{\mathrm{b}}}\Delta\sigma_{\mathrm{b}} = \frac{\varepsilon_{\mathrm{b}}}{\varepsilon_{\mathrm{s}}}\Delta\sigma_{\mathrm{b}} \tag{6.13}$$

As the errors on the cross section in Section 5.2 do not include the uncertainties on the parton density functions here uncertainties of 10% are assumed as estimated for the W+jets background [54]. Only for the QCD background 20% uncertainty has been chosen, as obtained at the D0 experiment for the fake and non-prompt electrons [55]. The promising estimate of the achievable statistical precision for the QCD normalisation in Section 6.2.1 did not include systematic uncertainties which are supposed to dominate. These assumptions yield $(\Delta\sigma)_{\mathrm{CS}} = 29.8$ pb for the complete analysis. This time the errors have been linearly added as the cross sections are possibly positively correlated due to the contributions of the parton density functions. The result for the analysis without the cut on missing transverse energy is $(\Delta\sigma)_{\mathrm{CS}} = 87.2$ pb with the main contribution originating from the QCD background. As without the $\not{E}_T$ cut the QCD dominates, see e.g. Figure 5.17, small background uncertainties propagate into considerable relative errors of the signal for the usual 10^{-3} fake electron probability assumption. Table 6.5 lists the contributions of the individual backgrounds to the error on the background cross section.

Since the error ΔS_{JES} on the significance S due to the uncertainty on the jet energy scale is reflected in the cross section according to

$$(\Delta S)_{\mathrm{JES}} = \left(\Delta\left(\frac{\sigma}{\Delta\sigma}\right)\right)_{\mathrm{JES}} = \frac{(\Delta\sigma)_{\mathrm{JES}}}{(\Delta\sigma)_{\mathrm{stat}}} \tag{6.14}$$

the contribution of the jet energy variation to the systematic error is

Sample	With $\not{E}_T$ Cut	Without $\not{E}_T$ Cut
other $t\bar{t}$	4.93 pb	4.61 pb
W+jets	11.13 pb	11.00 pb
single top	2.28 pb	2.32 pb
QCD fake leptons	11.08 pb	68.32 pb
QCD non-prompts	0.41 pb	0.96 pb
$(\Delta\sigma)_{\mathrm{CS}}$	29.83 pb	87.21 pb

Table 6.5: Contributions to the total systematic uncertainty of the cross section due to the individual background samples.

$$(\Delta\sigma)_{\mathrm{JES}} = (\Delta S)_{\mathrm{JES}} \cdot (\Delta\sigma)_{\mathrm{stat}} \tag{6.15}$$

For the expected 5% knowledge of the jet energy scale this gives $(\Delta\sigma)_{\mathrm{JES}} = 5.2$ pb for the analysis including the $\not{E}_T$ cut and $(\Delta\sigma)_{\mathrm{JES}} = 2.8$ pb for the reduced selection.

The error due to the integrated luminosity is calculated with

$$(\Delta\sigma)_{\mathrm{lumi}} = \frac{\partial\sigma}{\partial L}\Delta L = \frac{N}{\varepsilon_S L^2}\Delta L \tag{6.16}$$

and yields for the complete list of cuts an error of $(\Delta\sigma)_{\mathrm{lumi}} = 24.0$ pb at a precision for the integrated luminosity of 5% as expected for the first year of ATLAS [41]. Without cutting on missing transverse energy $(\Delta\sigma)_{\mathrm{lumi}}$ increases to 38.4 pb.

Table 6.6 summarises the contributions to the total error of the cross section measurement. The quadratic addition of the systematic errors yields

$$\Delta\sigma = \pm 0.5(\mathrm{stat}) \pm 30.4(\mathrm{syst}) \pm 24.0(\mathrm{lumi})\,\mathrm{pb} \tag{6.17}$$

for the complete analysis. For the analysis without the cut on $\not{E}_T$ the estimate is

$$\Delta\sigma = \pm 0.6(\mathrm{stat}) \pm 87.3(\mathrm{syst}) \pm 38.4(\mathrm{lumi})\,\mathrm{pb} \tag{6.18}$$

For a cross section of 242 pb this translates into a relative error of 16.0% and 39.4%, respectively. One has to keep in mind that the systematic error is just an estimate of the expected order of magnitude and depends mainly on the knowledge of the QCD background obtained from data. Nevertheless the analysis will be dominated by systematic uncertainties right from the first days as Figure 6.21 shows for the complete analysis. Even in a quite optimistic scenario with a combined 5% error due to systematics and the luminosity, which might be achievable with the improved understanding of the backgrounds after comparisons with real data, the systematic error already dominates after $15\,\mathrm{pb}^{-1}$. And even if the systematic uncertainties could be reduced to 1% the statistical error becomes insignificant after $400\,\mathrm{pb}^{-1}$. So a good understanding of systematic uncertainties will be crucial for the cross-section measurement, although they are small already. The contributions due to the finite Monte Carlo statistics can be reduced with more generated events. For the reduction of the uncertainty on the background cross section, however, the background

Error	With $\not{E}_T$ Cut	Without $\not{E}_T$ Cut
$(\Delta\sigma)_{\text{stat}}$	0.47 pb	0.57 pb
$(\Delta\sigma)_{\text{MC,s}}$	1.16 pb	1.12 pb
$(\Delta\sigma)_{\text{MC,b}}$	2.75 pb	2.88 pb
$(\Delta\sigma)_{\text{CS}}$	29.8 pb	87.2 pb
$(\Delta\sigma)_{\text{JES}}$	5.2 pb	2.8 pb
$(\Delta\sigma)_{\text{lumi}}$	24.0 pb	38.4 pb

Table 6.6: Summary of the statistical and systematic errors for the analysis with and without the cut on missing transverse energy for an integrated luminosity of $10\,\text{fb}^{-1}$ and a fake electron rate of 10^{-3}.
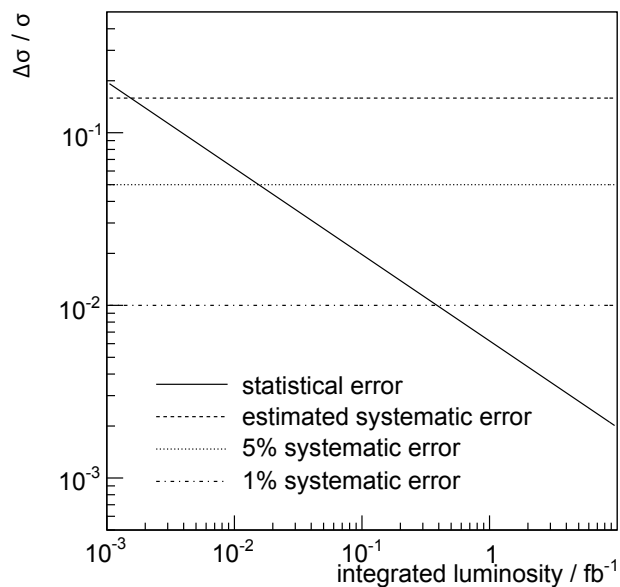
Figure 6.21: Evolution of the statistical error and three scenarios for the systematic uncertainty, including the luminosity error. In any case the precision will soon be dominated by systematic errors. With $10\,\text{fb}^{-1}$ integrated luminosity the horizontal axis covers about the first nominal year of the LHC.

shapes must be well understood in order to allow comparisons with real data. Here progress on both experimental and theoretical aspects is needed.

6.7 Potential for Analysis Improvements

Apart from efforts to obtain a better understanding of the background shapes and cross sections, the impact of the remaining errors could be improved by better identification of the signal events. In the previous analysis it was assumed that no b-jet identification was available. However, as soon as the Inner Detector is calibrated and aligned this should change. As in particular the W+jets and QCD backgrounds contain fewer b-quarks than the other samples the main sources of systematic error could be suppressed by implementing b-tagging. Figure 6.22 depicts the number of reconstructed b-jets for events after all the previous analysis cuts. The b-jet identification probability
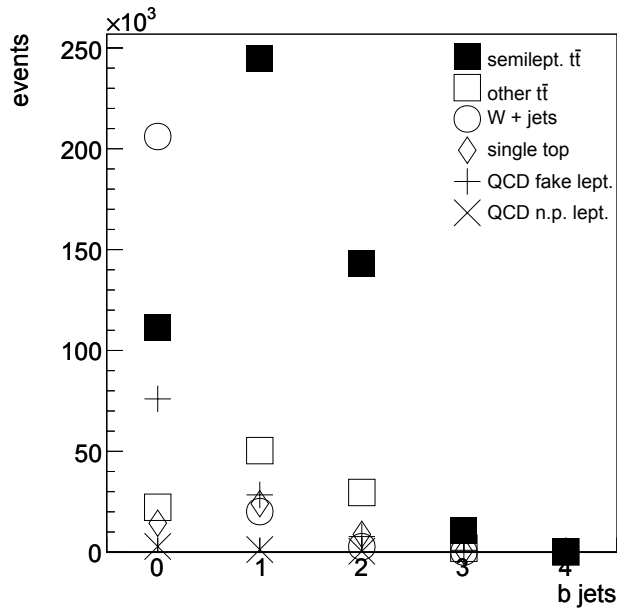
Figure 6.22: The number of identified b-jets per event after the standard analysis selection. The numbers are normalised to $10\,\mathrm{fb}^{-1}$ integrated luminosity. For the QCD background 10^{-3} fake probability was assumed.

amounts to 60%. For the $t\bar{t}$ signal and the backgrounds containing top quarks mostly one b-jet can be identified, often even both b-jets in the $t\bar{t}$ events. In case of W+jets and QCD the detection of zero b-jets is most probable. A rejection of events with no recognised b-jets increases the analysis significance from 508 to 525 and hence improves the statistical error. More importantly, the systematic uncertainty decreases due to the low selection efficiencies for W+jets and QCD events. With the additional cut on the b-jet multiplicity the estimate for the precision of the analysis ends at

$$\Delta\sigma = \pm 0.5(\text{stat}) \pm 14.0(\text{syst}) \pm 17.5(\text{lumi}) \tag{6.19}$$

which corresponds to a total relative error on the cross section of 9.3%, assuming negligible additional systematics from the b-jet identification.

Apart from the inclusion of b-jet identification in the analysis, progress can also be achieved by means of more effective event selections than just the presented cuts. For example a kinematic fit might decrease the number of selected background events and hence improve the systematics. Other techniques such as application of a neural network to discriminate between signal and background are also conceivable.

Part III

The Dileptonic Decay Channel

Chapter 7

Dileptonic Top Pair Analysis

The semileptonic channel is considered to be the golden channel when measuring $t\bar{t}$ properties, as it combines a good signature with the second largest branching ratio after the all hadronic decays. The dileptonic channel compensates its relatively small branching ratio of only about 5% with a clear final state signature involving two charged leptons, two jets which might even be b-tagged, plus missing transverse energy. In contrast to the semileptonic mode the event kinematics are not completely reconstructible as $\not{E}_T$ now originates from two neutrinos. This chapter examines the precision of a cross section measurement in the dileptonic channel studied by means of a cut based selection suitable for first data.

7.1 Signal and Backgrounds

As for the semileptonic channel a study of the dileptonic $t\bar{t}$ final states needs Monte Carlo samples for the various background which will be introduced here. All samples used have been centrally produced by the ATLAS collaboration with more details given in Appendix C.

7.1.1 Top Pairs Sample

As for the previous analysis the $t\bar{t}$ simulation with MC@NLO [8], not including all hadronic $t\bar{t}$ decays, has been used. As outlined in Section 5.2.1 13% of the events in this sample carry a negative weight. This time the sample was divided into events with dileptonic decays and the remainder with semileptonic and τ lepton decays, which is treated as background. The predicted cross sections are $38.3^{+2.4}_{-1.8}$ pb for the dileptonic channel and $411.5^{+25.6}_{-19.2}$ pb for the other $t\bar{t}$ events [1, 14]. The statistics of the individual decay types are listed in Table 7.1, not considering weights.

7.1.2 Z+Jets Background

Z bosons decaying into a pair of charged leptons contribute the main background for the dileptonic $t\bar{t}$ channel as the final state may contain the same number of charged leptons and jets as the signal events, see Figure 7.1. But, in contrast to dileptonic top pairs, no neutrino is expected among the decay products. So for Z decays into electrons or muons the missing transverse energy must originate from the finite detector resolution. Only in the case where the Z bosons decay to τ

83

Decay Type	Events	Cross Section [pb]
semileptonic	292 703	242.6
tau lepton(s)	207 480	168.9
dileptonic	48 327	38.3
undefined	40	

Table 7.1: The number of events (without considering weights) in the $t\bar{t}$ sample without all-hadronic decays, separated according to the decay type.
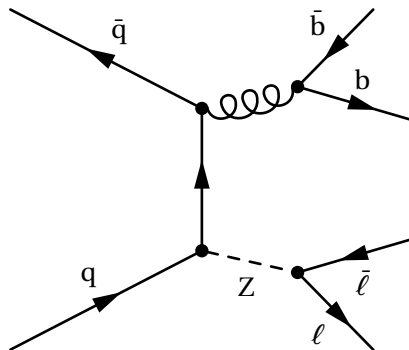
Figure 7.1: Z boson decay into a final state with two charged leptons and two (b)-jets from initial state radiation.

leptons with subsequent decays of the taus into electrons or muons plus the associated neutrinos does the final state have the same signature as the $t\bar{t}$ signal. In this case the final state can in principle only be distinguished kinematically from the signal. The Z+jets samples have been produced with PYTHIA [3] which gave the cross section and dataset statistics as listed in Table 7.2. As PYTHIA calculates to leading order the table includes a correction factor of 1.2 to reach the NLO cross section given in [56]. The uncertainty on the cross section, including the PDFs, is about 10% [54].

7.1.3 Diboson Background

Another source of background may be interactions in which two vector bosons are produced. A variety of final states exists as for W and Z bosons both leptonic and hadronic decays are possible and combinatorics plus the possibility of initial state radiation allows for events which resemble a dileptonic top pair decay. Figure 7.2 shows two possible ZZ background events with two charged leptons and two jets in the final state. In one case all particles stem from the Z decays and missing transverse energy arises from the finite detector resolution. Such events may be difficult to

Channel	Events	Cross Section [pb]
$Z \to ee$	481 300	2015
$Z \to \mu\mu$	185 400	2015
$Z \to \tau\tau$	176 300	1972

Table 7.2: The number of events in the Z+jets samples plus the cross section including the branching ratio. A next-to-leading order correction factor of 1.2 was applied.
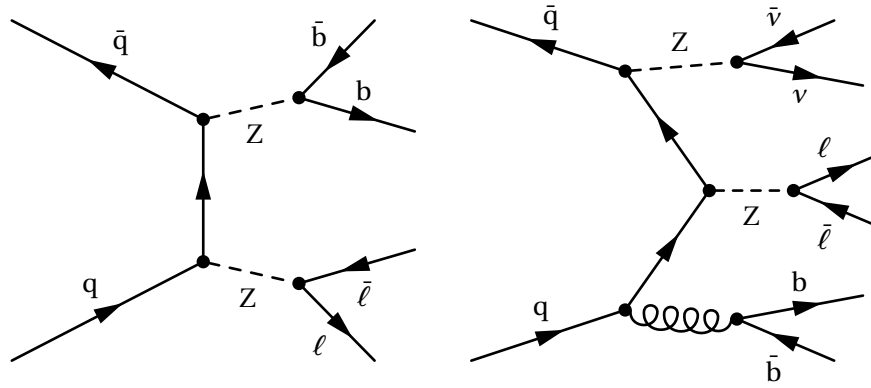
Figure 7.2: The left diagram shows a ZZ final state with the same final state particles as for the dileptonic t$\bar{\text{t}}$ decay except the neutrino. The process depicted in the right diagram is irreducible on single event basis as the composition is the same as for the dileptonic t$\bar{\text{t}}$ signal.
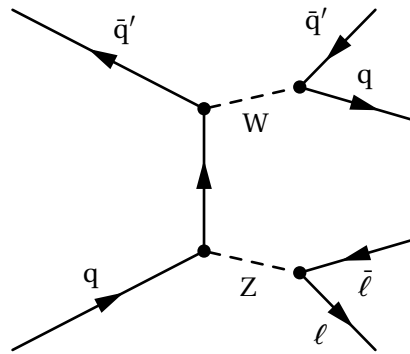

Figure 7.3: With $\not{E}_T$ from the limited detector resolution this WZ process can contribute a background to the dileptonic top pair decays.

distinguish from dileptonic t$\bar{\text{t}}$ decays. Another possibility is that the two jets originate from gluon radiation and real $\not{E}_T$ occurs due to a Z boson decay into a pair of neutrinos whilst the other Z decay contributes two charged leptons.

WZ events are also a source of background. Figure 7.3 presents a final state with two charged leptons produced by the Z boson decay and two jets originating from the W boson. Missing transverse energy may occur here as a detector effect.

The remaining diboson background is two W bosons which decay leptonically plus two jets from initial state radiation as shown in Figure 7.4. These events are good candidates for the diboson background in the dileptonic t$\bar{\text{t}}$ analysis as real missing transverse energy occurs and the leptons originate from different bosons. Furthermore the production cross section for WW events is the highest of all diboson branches as no anti-quarks, which only occur as sea quarks inside the protons, are needed for the production.

The samples for all three channels have been produced with HERWIG [4]. To reduce the number of events to be produced at least one electron or muon with $p_T > 10\,\text{GeV}$ was required at the truth level in the final state [57]. The resulting effective cross sections plus the available sample statistics are given in Table 7.3.
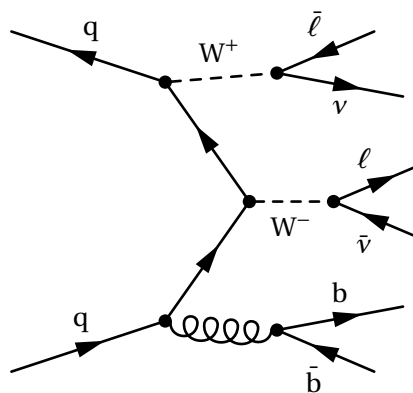
Figure 7.4: The sketched WW process is another source of dibosonic background events in the dileptonic t$\bar{\text{t}}$ decay channel.

Channel	Events	Cross Section [pb]
ZZ	29 800	2.1
WZ	31 150	7.8
WW	16 250	24.5

Table 7.3: The number of events in the diboson samples plus the expected production cross section including the efficiency of a generator level filter which demanded at least one reconstructed electron or muon.

7.1.4   W+Jets Background

Just as fake and non-prompt electrons contributed background in the semileptonic channel they also could be non-negligible when measuring the dileptonic states. For fake probabilities on the order of 10^{-3} the contribution from pure QCD events to the dileptonic analysis is negligible as QCD events are very unlikely to produce two fakes at the same time, which compensates for the high QCD cross section. But events which already have a true lepton in the final state might be confused with dileptonic t$\bar{\text{t}}$ production if an associated jet gives an additional fake lepton. W+jets events are candidates for such a background[1]. Even though W+jets samples are available with the full detector simulation applied, the statistics of the samples are too low to see clear shapes in the distributions when selecting events with two leptons. When the fake rate is assumed, however, it is possible to model the W+jets background in the way the QCD background was modelled in Section 5.2.4. Unfortunately, the original samples are supposed to include a fraction of fake electrons already. As, to include the non-prompts, the samples are used twice, once with and once without modelled fakes, a double counting of the fakes electrons occurs. In principle it would be possible to identify and remove events with fakes in the original samples via comparisons with the Monte Carlo truth information. But, as the dileptonic analysis will reveal a practically negligible contribution from W+jets events to the background for the expected order of the fake probability, the double counting remains uncorrected.

Table 7.4 shows the cross sections of the W+jets samples produced with PYTHIA [3]. In contrast to the W+jets samples introduced for the semileptonic analysis in Section 5.2.2 no cut on he number of true jets was applied at the generator level, hence the higher cross sections although a filter requiring one final lepton on truth level was applied. Due to this cut the τ fraction has a smaller

---

[1]Also the single tops might contribute but the production cross section is considerably lower than for the W+jets events.

Channel	Events	Cross Section [pb]
$W \rightarrow e\nu + \text{jets}$	483 750	10 900
$W \rightarrow \mu\nu + \text{jets}$	214 700	11 946
$W \rightarrow \tau\nu + \text{jets}$	141 000	3 400

Table 7.4: The number of events in the W+jets samples plus the effective cross sections with a lepton filter applied at the truth level which requires a minimum lepton p_T of 10 GeV for the electron sample and 5 GeV for the other two.

Sample	σ [pb]	$\langle n_{jets} \rangle$	σ_{eff} [pb]
$W \rightarrow e\nu + \text{jets}$	10 900	1.025	11.2
$W \rightarrow \mu\nu + \text{jets}$	11 946	0.719	8.6
$W \rightarrow \tau\nu + \text{jets}$	3 400	0.899	3.1

Table 7.5: Expected effective cross section of the W+jets samples with jets falsely reconstructed as electrons for $P(j \rightarrow e) = 10^{-3}$.

effective value as hadronic decays are not part of the sample.

As for the QCD in the semileptonic channel, the effective cross sections must be corrected according to

$$\sigma_{\text{eff}} = \sigma \cdot P(j \rightarrow e) \cdot \langle n_{\text{jets}} \rangle \tag{7.1}$$

with the average number of jets $\langle n_{\text{jets}} \rangle$ per event, taken from Figure 7.5, and the fake electron probability $P(j \rightarrow e)$ which again was set to 10^{-3}. The results are listed in Table 7.5. As the following dileptonic analysis cuts on the lepton charge the fake electrons are assigned a random charge of ± 1.

7.2 Cut Based Signal Selection

As for the semileptonic channel the dileptonic analysis will also be cut based and thus more appropriate for the first data than complex methods using e.g. likelihoods or neural networks. As two neutrinos appear in the final state the kinematics can not be reconstructed completely, especially the top and W masses are not directly reconstructible. However, as the reconstructible hadronic top masses did not improve the semileptonic selection significance, here the observable event kinematics should also allow for a satisfactory background suppression.

7.2.1 Trigger Stage

As before only lepton triggers will be used for the analysis as they will not be prescaled and can be more easily tested with real data than jet triggers. Since both charged leptons have a chance to activate the trigger an efficiency higher than that in the dileptonic channel is expected. Again muons must have a transverse momentum above 20 GeV and electrons are required be isolated and must lie above 25 GeV. In Figure 7.6 the trigger efficiencies for the signal and all backgrounds except the W+jets after the three trigger levels is given. The precise values are listed in Table 7.6. With
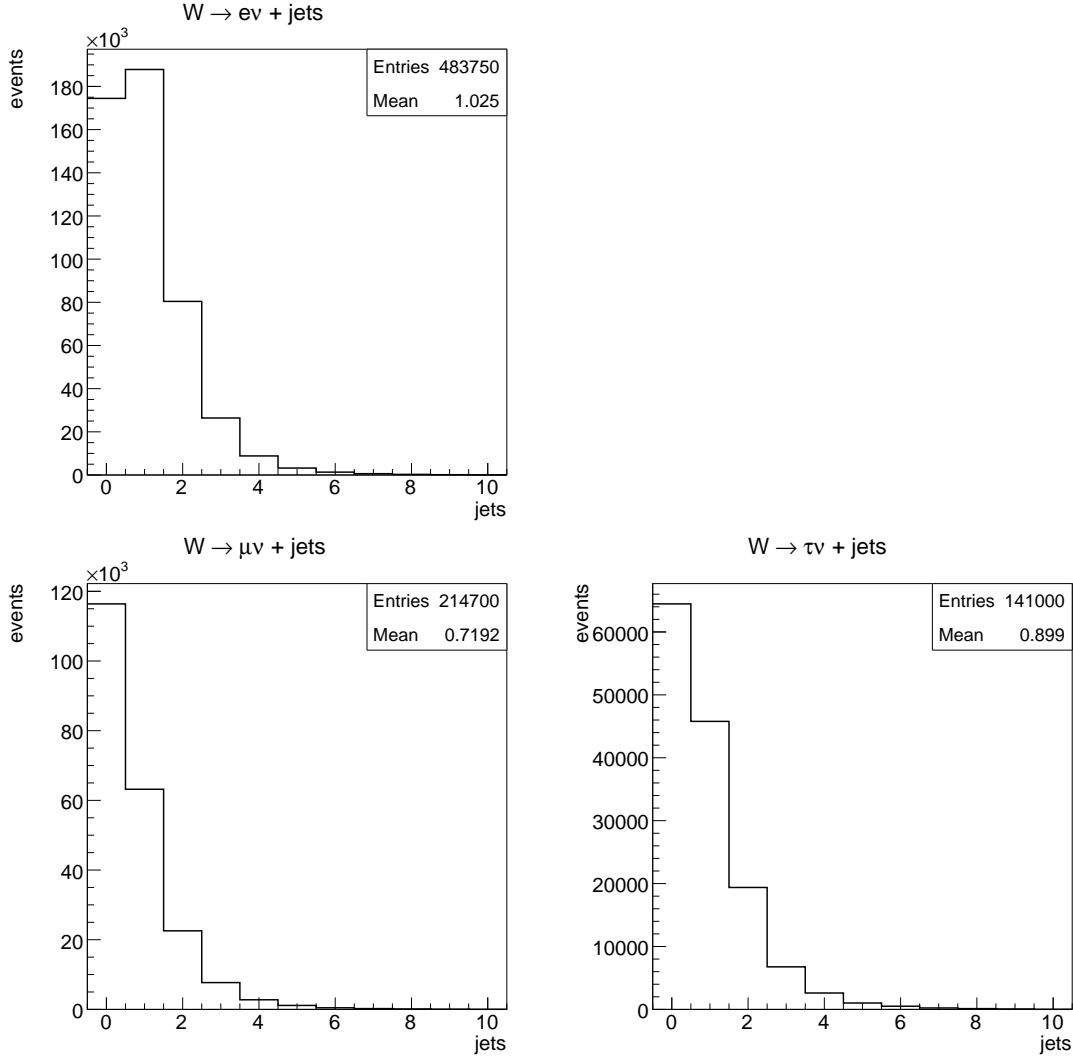
Figure 7.5: The number of jets per event in the W+jets samples for the three different leptonic W boson decays.

81% probability the signal events are most likely to be kept followed by the diboson and Z+jets backgrounds with 58% and the other $t\bar{t}$ decays with 43% chance. The main reason for the lower background efficiencies is the fraction of τ decays, as explained in the semileptonic trigger study in Section 5.4.1. For W+jets the trigger simulation is replaced by a parametrisation where reconstructed muons above 20 GeV have an event weight w_μ of 0.78 and reconstructed (fake) electrons over 25 GeV have a weight w_e of 0.87. The weights are those obtained in Section 5.4.1 for the trigger plateau regions. For events with more than one reconstructed lepton above the thresholds the weights are combined to the total event weight w according to

$$w = 1 - \prod_i (1 - w_i) \tag{7.2}$$

where w_i is the weight or probability of the ith reconstructed lepton to be triggered. For W+jets with fake electrons this results in an overall trigger probability of about 60% whereas the original
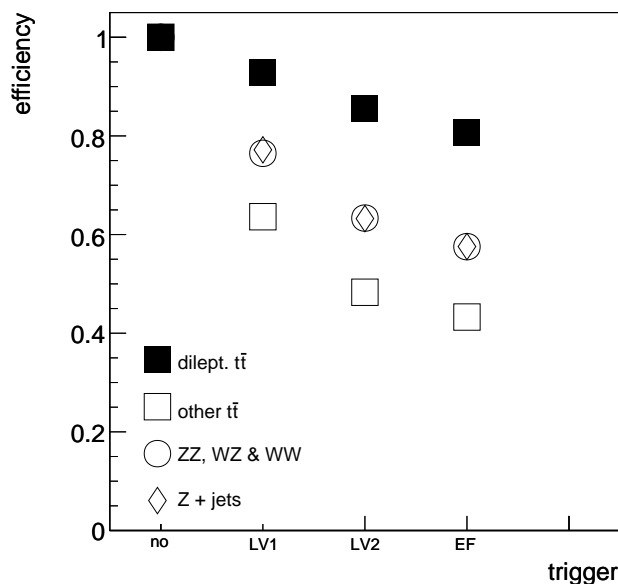
Figure 7.6: The efficiency after the Level 1 (LV1), Level 2 (LV2) and Event Filter (EF) trigger stages.

Sample	Level 1	Level 2	Event Filter
dileptonic $t\bar{t}$	0.929 ± 0.007	0.856 ± 0.007	0.807 ± 0.006
other $t\bar{t}$	0.636 ± 0.002	0.483 ± 0.001	0.432 ± 0.001
dibosons	0.765 ± 0.007	0.633 ± 0.006	0.575 ± 0.005
Z+jets	0.772 ± 0.001	0.632 ± 0.001	0.576 ± 0.001

Table 7.6: Trigger efficiency values for signal and background samples.

W+jets samples have a trigger probability of 42% due to the lower fraction of leptons.

7.2.2 Lepton Selection Criteria

Again not all leptons kept by the TOPVIEW overlap removal are taken for the analysis. In addition to the preselection, demanding $|\eta| < 2.5$, $p_T > 20\,\text{GeV}$, all leptons must lie outside the cones of reconstructed jets and as before electrons in the EC transition region $1.37 < |\eta| < 1.52$ are rejected. To avoid the trigger turn-on region all leptons with $p_T < 30\,\text{GeV}$ are vetoed as well. Exactly two leptons passing this preselection are required for the subsequent analysis.

For an improved lepton selection the reconstructed transverse momenta are histogrammed, without the additional 30 GeV cut, in Figure 7.7 for the highest and second highest energetic lepton. Apparently for both a cut above the peak of the Z+jets background, which is due to the Z boson origin, would yield the best selection improvement. However, as the Z mass veto later in the selection will remove this structure, no further cuts on the lepton transverse momenta are applied.

Also the lepton $|\eta|$ distributions in Figure 7.8 are not suitable to be cut on, as only the W+jets samples show a considerably flatter curve than the signal but will ultimately contribute an almost
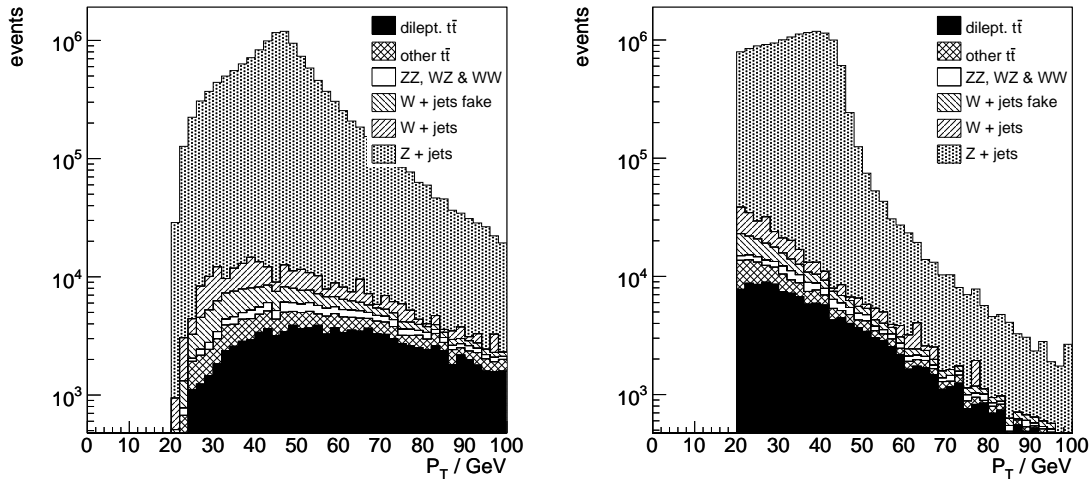
Figure 7.7: Stacked transverse momentum distribution of the leading lepton (left) and the second leading lepton (right) for events with at least 2 leptons above 20 GeV which passed the trigger, normalised to an integrated luminosity of $10\,\text{fb}^{-1}$. The maximum observed in the Z+jets background is a result of the momentum obtained from the Z boson decay.

negligible background. Hence only the preselection cuts on the jet direction are used.

With this lepton selection the statistical significance obtained amounts to 30 for $10\,\text{fb}^{-1}$ integrated luminosity. The additional requirement of two opposite lepton charges reduces the W+jets background, as will be seen in the cut flow in Section 7.3, since the fake electrons have a random charge. However, due to the dominating Z+jets background the significance remains at a value of 30 for $10\,\text{fb}^{-1}$ integrated luminosity.
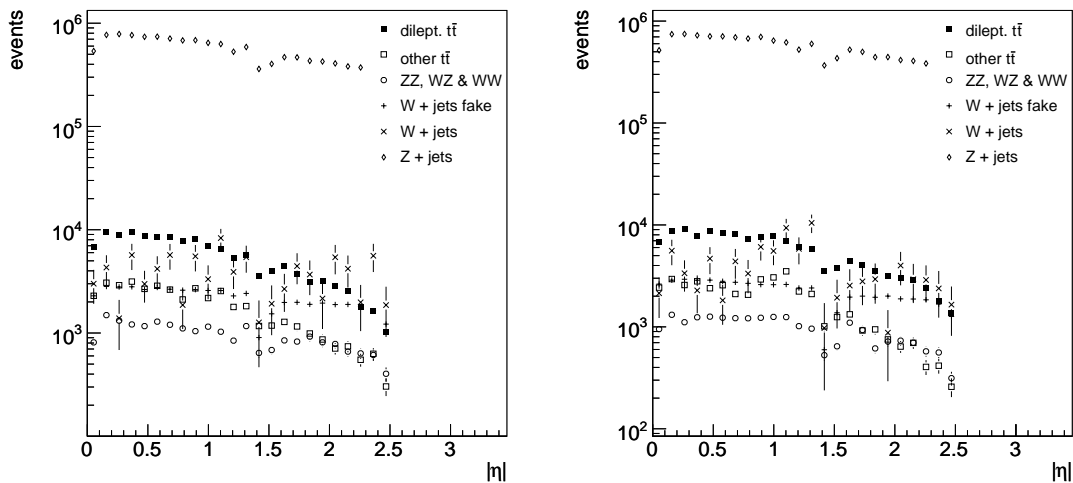
Figure 7.8: Distributions of $|\eta|$ for the leading lepton (left) and the second leading lepton (right) for events with at least 2 leptons above 20 GeV which passed the trigger. The number of events corresponds to an integrated luminosity of $10\,\text{fb}^{-1}$.
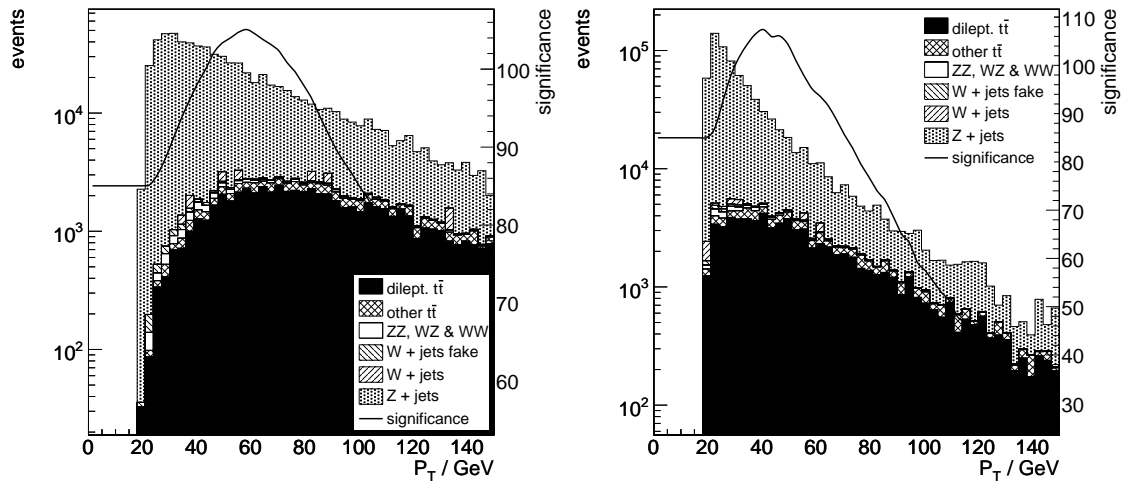
Figure 7.9: Stacked transverse momentum distributions of the leading jet (left) and the second leading jet (right) for events which passed the lepton selection. The normalisation corresponds to an integrated luminosity of $10\,\mathrm{fb}^{-1}$. The solid lines indicate the selection significance for a cut applied at this value.

7.2.3 Particle Jet Properties

TOPVIEW required a minimum transverse momentum of $20\,\mathrm{GeV}$ for the jet preselection. As the dileptonic final state contains two b-quarks at least two preselected jets are required before a closer inspection of the jet properties. Figure 7.9 shows the distribution of the transverse momentum of the two most highly energetic jets. Also indicated is the selection significance obtained for a cut on this jet only. The optimum for the leading jet is a threshold at $55\,\mathrm{GeV}$, resulting in a significance of 105 for $10\,\mathrm{fb}^{-1}$ integrated luminosity. A selection based on the second jet yields an optimum cut at $40\,\mathrm{GeV}$ and a significance of 107. A combination of both cuts raises the significance to 108 for $10\,\mathrm{fb}^{-1}$ integrated luminosity. So the events with a low leading jet p_T also tend to have a low second leading jet p_T. To disentangle this correlation Figure 7.10 shows the selection significance as a function of both jet transverse momenta. However, even when considering the correlation the best cuts remain at $55\,\mathrm{GeV}$ and $40\,\mathrm{GeV}$.

The distributions of the pseudorapidities for the two leading jets are depicted in Figure 7.11. Even though, due to the high masses involved, the $t\bar{t}$ system should be less boosted than the rest frames of the background processes, the jets are only slightly more central and no cut to improve the selection was found, besides the TOPVIEW preselection of $|\eta| < 2.5$.

7.2.4 Z Boson Mass Veto

The main background are the Z+jets events for which the invariant two lepton mass should peak at the Z boson mass with the exception of the τ decays. Here in the all leptonic case, which contributes the background from this channel, momentum originating from the Z boson mass is carried away by neutrinos. The dibosonic background should also benefit from a veto on the Z mass as also here two leptons stemming from the same Z boson may occur.

Figure 7.12 depicts the distribution of the invariant dilepton mass $m_{\ell\ell}$ defined by
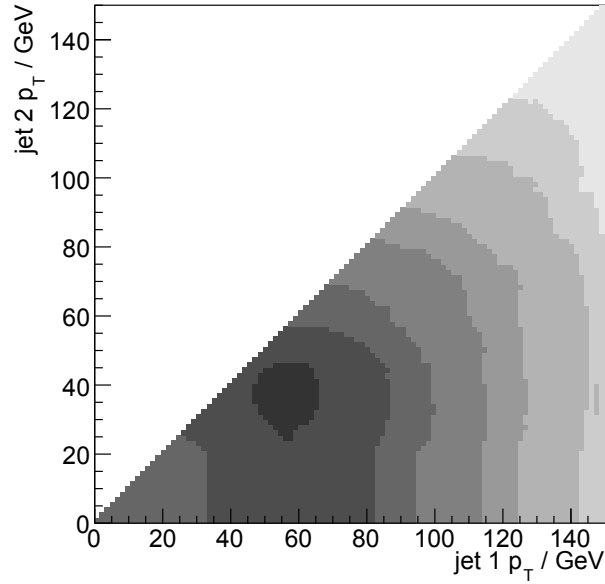
Figure 7.10: The significance as a function of the cuts on the leading jet p_T and the second leading jet p_T. The darker the shade the higher the significance. The best choice remains the same (55 GeV and 40 GeV) as obtained for the individual distributions in Figure 7.9.
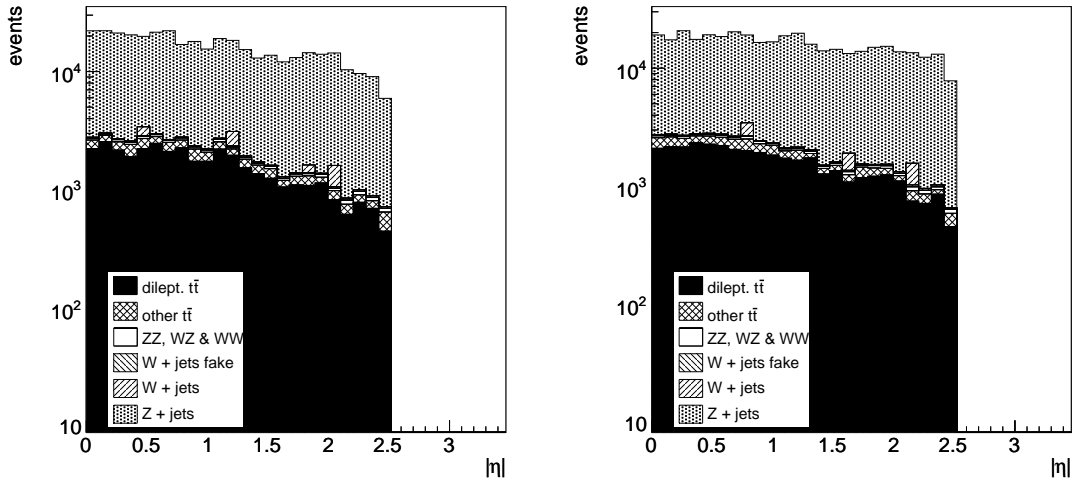
Figure 7.11: Stacked distributions of $|\eta|$ for the leading jet (left) and the second leading jet (right) for events which passed the lepton selection. The number of events corresponds to an integrated luminosity of $10\,\mathrm{fb}^{-1}$.

$$m_{\ell\ell} = \sqrt{(E_1 + E_2)^2 - (p_{x,1} + p_{x,2})^2 - (p_{y,1} + p_{y,2})^2 - (p_{y,1} + p_{y,2})^2}$$ (7.3)

The Z mass peak is prominent and permits a cut for leptons of the same type, i.e. two electrons or two muons, removing such events with $80\,\mathrm{GeV} < m_{\ell\ell} < 100\,\mathrm{GeV}$. Also the region below $m_{\ell\ell} =$
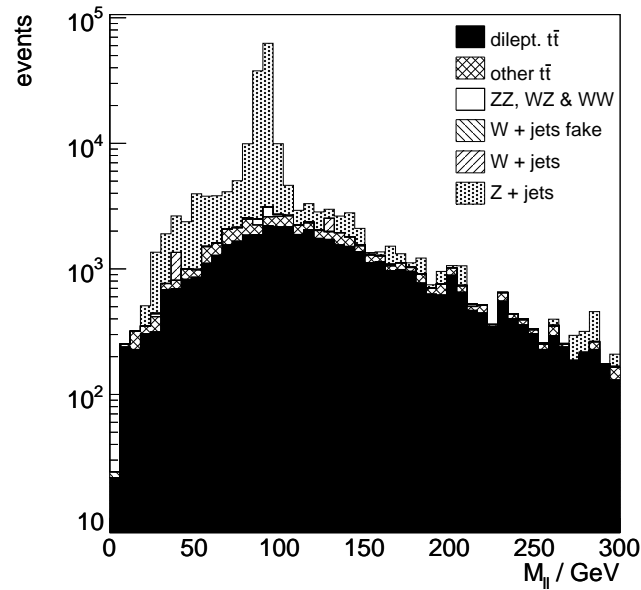
Figure 7.12: Stacked distribution of the invariant mass calculated for the two leading leptons, normalised for an integrated luminosity of $10\,\text{fb}^{-1}$. The Z peak is clearly visible for the Z+jets background.

60 GeV is rejected for all events as the Z sample used applied this threshold after event generation. With this combination the significance of the selection is raised to 150 for $10\,\text{fb}^{-1}$ integrated luminosity. Of course later in experiment the Z mass window has to be set according to the achieved Z mass resolution and may be chosen differently for electrons and muons.

7.2.5 Missing Transverse Energy

A further observable to distinguish the dileptonic $t\bar{t}$ events from the Z+jets background is the missing transverse energy which is expected to occur for the signal as the two neutrinos in the final state rarely balance out. For the Z+jets missing transverse energy originating from neutrinos and not from a detector resolution effect only appears in the leptonic τ decays. Hence $\not{E}_T$, unless affected by large systematic uncertainties, should be a good background discriminant. Figure 7.13 shows the missing transverse energy distribution after the previous cut on the dilepton mass. As expected a clear difference between signal and background is visible. Application of the optimum cut at 25 GeV raises the significance to 159 for $10\,\text{fb}^{-1}$ integrated luminosity. The remaining Z+jets background consists of 20% electron, 30% muon and 50% tau events. Although the diboson background is almost negligible it should be mentioned that this background is also reduced by requiring $\not{E}_T$ as some of its final states do not contain neutrinos.

7.3 Selection Efficiency and Cut Flow

To conclude the individual selections from the previous section the cut flow will be summarised at this point before systematic influences are studied. The selection efficiencies after the single
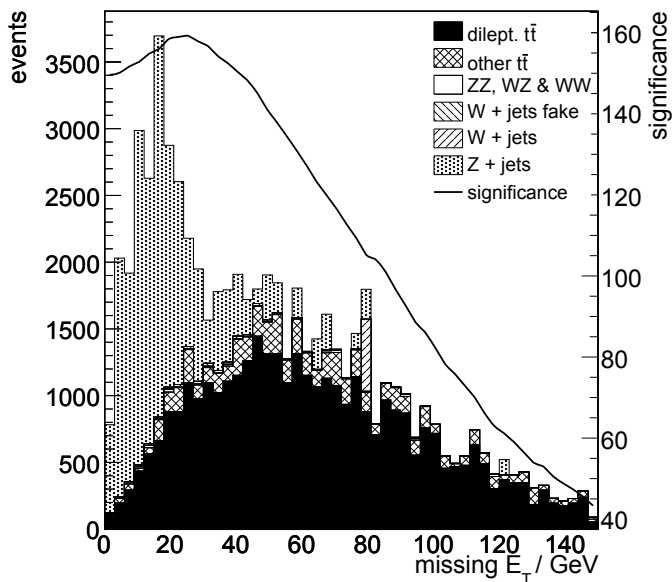
Figure 7.13: Stacked missing transverse energy distributions, normalised for an integrated luminosity of $10\,\mathrm{fb}^{-1}$. The solid line indicates the selection significance for a cut at this value.

cuts are given in Figure 7.14 and Table 7.7. The latter also includes the uncertainties due to the limited number of events in the used Monte Carlo samples, calculated as derived in Appendix B. For backgrounds consisting of several samples the individual errors have been added after being multiplied with the scaling factor of the sample. The signal survives the complete selection with a probability of about 9%. Background events are selected with a chance of around $0.1\% - 0.01\%$ and a steady enhancement of the signal is visible throughout the selection. After all analysis cuts the uncertainties remain about one order of magnitude below the mean values except for the original W+jets sample with an error of the same size as the expectation value. Because the signal has the largest selection efficiency is also has the smallest error due to the Monte Carlo statistics.

Figure 5.22 and Table 5.11 contain the number of events resulting for an integrated luminosity of $10\,\mathrm{fb}^{-1}$ and 10^{-3} misidentification probability for the W+jets fake electron sample. Apparently the lepton selection helps in particular to reduce the original W+jets events and the background from the other $t\bar{t}$ events. The strongest barrier for the Z+jets background is the jet selection. With the final cuts on the dilepton mass and the missing transverse energy the final number of background events is considerably lower than the final number of dileptonic $t\bar{t}$ events.
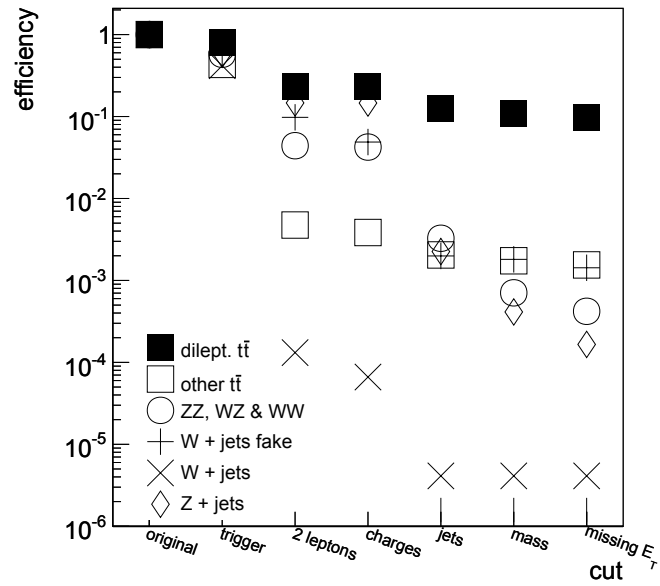
Figure 7.14: Accumulated efficiencies after each analysis cut. The uncertainties on the efficiencies are not drawn but are listed in Table 7.7 instead.
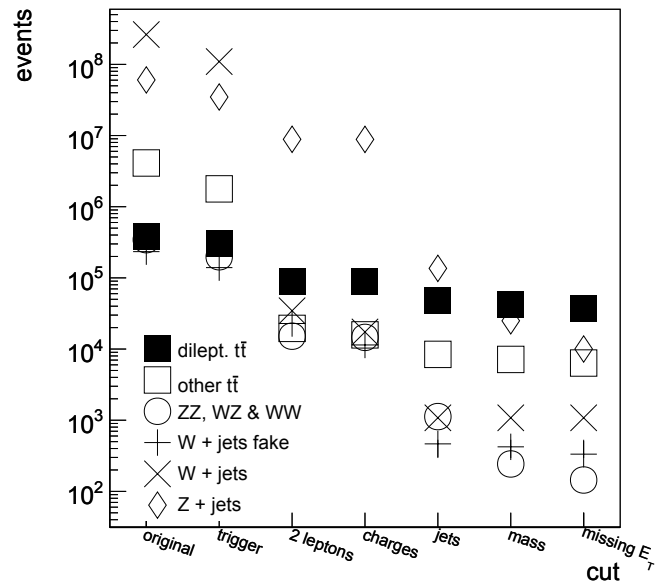
Figure 7.15: The number of events remaining after the analysis cuts for a fake electron probability of 10^{-3} and $10\,\text{fb}^{-1}$ integrated luminosity.

Sample	Cut 1: Trigger	Cut 2: Leptons
dileptonic t$\bar{\text{t}}$	0.8069 ± 0.0025	0.2344 ± 0.0026
other t$\bar{\text{t}}$	0.4328 ± 0.0010	0.0047 ± 0.0001
dibosons	0.5755 ± 0.0028	0.0441 ± 0.0010
W+jets fake	0.5963 ± 0.0005	0.0978 ± 0.0004
W+jets	0.4171 ± 0.0006	$13 \cdot 10^{-5} \pm 2 \cdot 10^{-5}$
Z+jets	0.5757 ± 0.0006	0.1465 ± 0.0004

Sample	Cut 3: Charges	Cut 4: Jets
dileptonic t$\bar{\text{t}}$	0.2330 ± 0.0026	0.1242 ± 0.0021
other t$\bar{\text{t}}$	0.0038 ± 0.0001	0.0020 ± 0.0001
dibosons	0.0424 ± 0.0010	0.0033 ± 0.0002
W+jets fake	0.0488 ± 0.0003	0.0020 ± 0.0001
W+jets	$7 \cdot 10^{-5} \pm 1 \cdot 10^{-5}$	$4 \cdot 10^{-6} \pm 3 \cdot 10^{-6}$
Z+jets	0.1461 ± 0.0004	0.0023 ± 0.0001

Sample	Cut 5: Mass	Cut 6: Missing E_T
dileptonic t$\bar{\text{t}}$	0.1013 ± 0.0019	0.0899 ± 0.0018
other t$\bar{\text{t}}$	0.0016 ± 0.0001	0.0014 ± 0.0001
dibosons	0.0007 ± 0.0001	0.0004 ± 0.0001
W+jets fake	0.0017 ± 0.0001	0.0013 ± 0.0001
W+jets	$2 \cdot 10^{-6} \pm 2 \cdot 10^{-6}$	$2 \cdot 10^{-6} \pm 2 \cdot 10^{-6}$
Z+jets	$34 \cdot 10^{-5} \pm 2 \cdot 10^{-5}$	$10 \cdot 10^{-5} \pm 1 \cdot 10^{-5}$

Table 7.7: Accumulated efficiencies after the analysis cuts.

Sample	Original	Cut 1: Trigger	Cut 2: Leptons
dileptonic t$\bar{\text{t}}$	383 000	309 029	89 790
other t$\bar{\text{t}}$	4 115 000	1 780 890	19 512
dibosons	344 000	197 960	15 157
W+jets fake	233 800	139 421	22 855
W+jets	262 460 000	109 462 000	34 528
Z+jets	60 450 000	34 800 600	8 858 860
significance	21.1	25.5	29.8

Sample	Cut 3: Charges	Cut 4: Jets
dileptonic t$\bar{\text{t}}$	89 235	47 564
other t$\bar{\text{t}}$	15 815	8 419
dibosons	14 585	1 124
W+jets fake	11 418	465
W+jets	17 379	1081
Z+jets	8 829 790	136 064
significance	29.8	107.8

Sample	Cut 5: Mass	Cut 6: Missing E_T
dileptonic t$\bar{\text{t}}$	38 812	34 431
other t$\bar{\text{t}}$	6 609	5 890
dibosons	240	141
W+jets fake	393	311
W+jets	540	540
Z+jets	20 698	5 782
significance	149.6	158.7

Table 7.8: Remaining events after the analysis cuts for a fake electron probability of 10^{-3} and $10\,\text{fb}^{-1}$ integrated luminosity.

Chapter 8

Systematic Uncertainties in the Dileptonic Channel

Like the semileptonic also the dileptonic channel will be affected by systematic uncertainties. Unlike for the QCD fake electron background in the semileptonic analysis no discussion of equivalent detail for the W+jets fake electron events will be realised here as the final contribution turned out to be marginal anyway. As the applied methods are the same as in Chapter 6 mainly the results obtained for the dileptonic analysis are given, to avoid repeating the details.

8.1 Impact of a Reduced Detector Resolution

As in Section 6.3 the influence of a reduced detector resolution for the particle jets is studied. Again the jet energies are smeared on the basis of a Gaussian distribution with a width of

$$\sigma_E = c \cdot \sqrt{E} \tag{8.1}$$

while the jet directions remain constant. The impact on the total jet energy resolution from such a smearing with the parameter c in the range between $0/\sqrt{\text{MeV}}$ and $50/\sqrt{\text{MeV}}$ was depicted in Figures 6.10 and 6.11, concluding that $c = 35/\sqrt{\text{MeV}}$ corresponds to an additional smearing of about the same amount as the originally simulated resolution.

Figure 8.1 shows the jet selection significance as a function of the cuts applied on the two leading jets, once with the smearing as obtained from the detector simulation and as an example also for an additional contribution according to equation 8.1 with $c = 35/\sqrt{\text{MeV}}$. Over the whole c variation interval from $0/\sqrt{\text{MeV}}$ to $50/\sqrt{\text{MeV}}$ the optimum remains close to the original optimum of a minimum transverse momentum of $55\,\text{GeV}$ for the leading jet and $40\,\text{GeV}$ for the second. Hence the jet selection can be kept even in case of a reduced jet energy resolution.

As for the semileptonic analysis a smearing of the jet energies will also affect the measured missing transverse energy. To study the impact of the smearing on the $\not{E}_T$ cut the reconstructed missing transverse energy has been corrected for the additional smearing as explained in Section 6.3. Figure 8.2 compares the original $\not{E}_T$ distribution, which is cut on after the Z mass veto, to the result obtained for a smearing with $c = 35/\sqrt{\text{MeV}}$. The position of the best cut remains about constant, only the significance of the best cut drops from 159 to 153 for $10\,\text{fb}^{-1}$ integrated luminosity. For

99
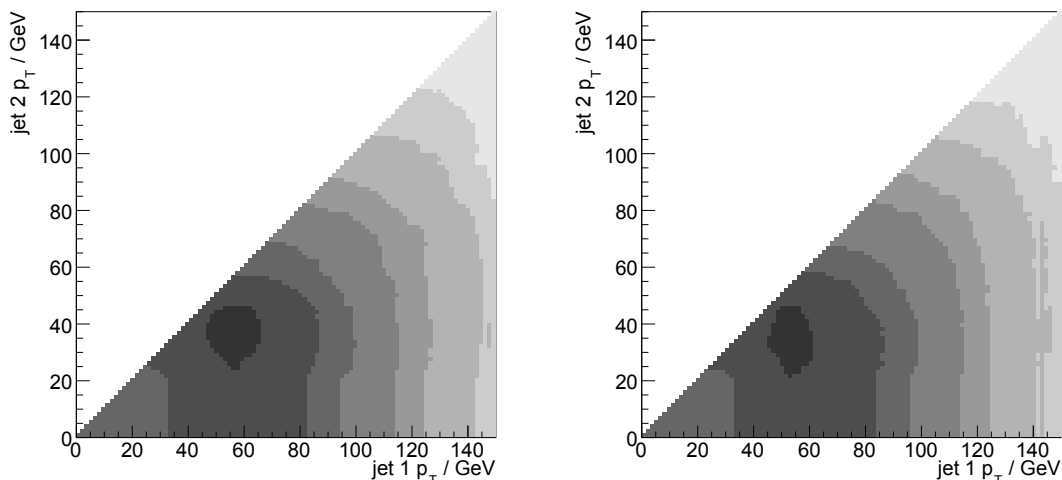
Figure 8.1: The significance as a function of the cuts on the leading jet p_T and the second leading jet p_T. The darker the shade the higher the significance. The left plot is the result without an additional jet energy smearing whereas for the right plot a smearing of $c = 35/\sqrt{\text{MeV}}$ was applied. The best selection cut remains in the region of 55 GeV for the leading and 40 GeV for the second jet.

other choices of c the impact on the selection significance is depicted in Figure 8.3 for the standard analysis with a $\not{E}_T$ cut at 25 GeV, the analysis without the final cut on missing transverse energy, and the analysis with the $\not{E}_T$ cut optimised for the additional smearing. As the optimum threshold remains approximately constant[1] no improvement by means of such an optimisation could be observed. A reduced detector resolution propagates into the significance of the selection but the relative impact is smaller than observed in Figure 6.13 for the semileptonic analysis.

8.2 Jet Energy Scale Uncertainty

The influence of a jet energy scale variation on the dileptonic $t\bar{t}$ channel was studied, assuming a constant factor for the deviation from the correct energies. In the early phase of ATLAS this factor is expected to be of the order of 5%. Figure 8.4 shows the influence of a variation of the jet energy scale on the significance of the dileptonic analysis with and without the cut on $\not{E}_T$. Considered is the interval between 0.9 and 1.1 with data points at $\pm 2.5\%$, $\pm 5\%$ and $\pm 10\%$. In contrast to the results for the semileptonic channel this time the significance even increases for scale factors above one. Apparently due to correlations with the cut on the Z mass, the best choice for the jet p_T cuts slightly shifts to lower values. As the energy spectrum of the jets is afflicted with systematic uncertainties anyway the previous thresholds are kept nevertheless.

The changes of significance translate into systematic errors due to the jet energy scale according to Table 8.1. Not to state asymmetric errors and as a conservative estimate only the deviations for scale factors below 1.0 are considered. As in the semileptonic analysis the systematic error due to the jet energy scale is larger for the selection using missing transverse energy.

---

[1]The optimum $\not{E}_T$ threshold fluctuates between 21 and 26 GeV with no obvious trend.
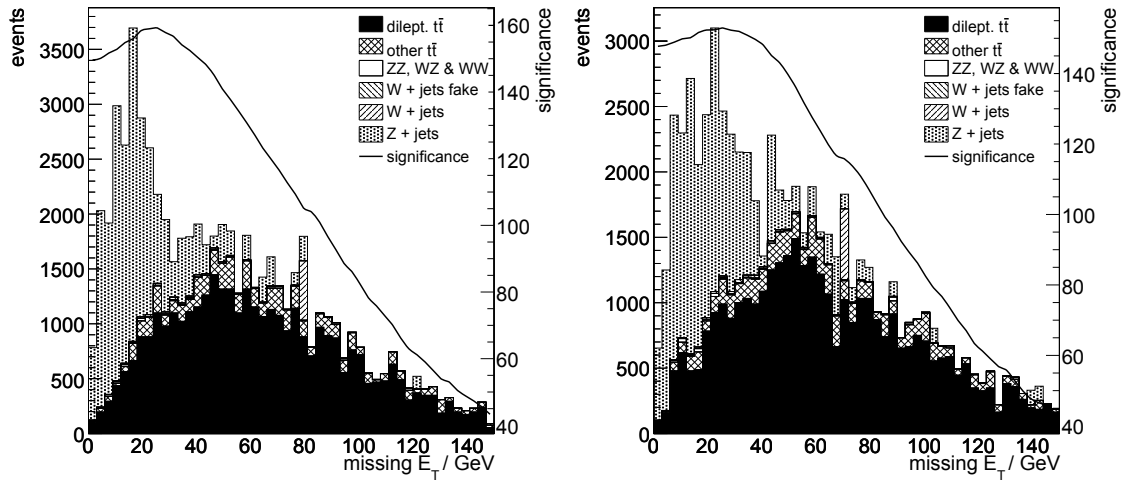
Figure 8.2: The original missing transverse energy distributions after the jet selection (left) in comparison to the same distribution after an additional smearing according to equation 8.1 with $c = 35/\sqrt{\text{MeV}}$ (right). As usual the line indicates the significance of a cut and the histograms are normalised to a constant fake electron probability of 10^{-3} and $10\,\text{fb}^{-1}$ integrated luminosity.
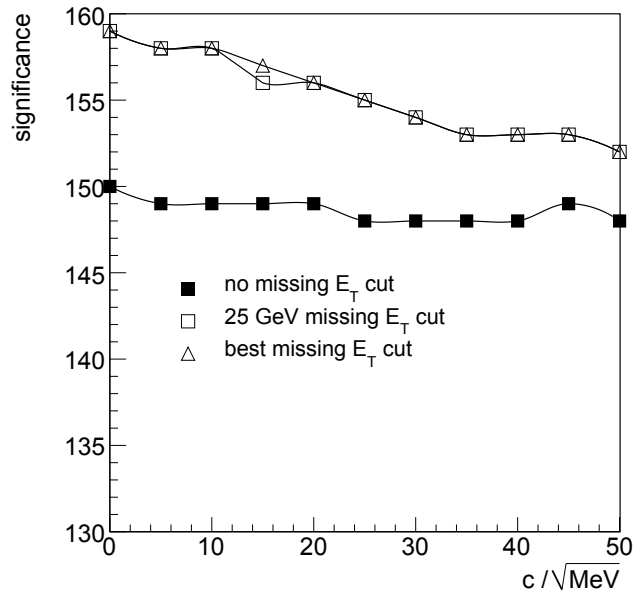
Figure 8.3: The selection significance without the cut on $\not{E}_T$, the selection significance including the cut on $\not{E}_T$, and a significance using the optimum $\not{E}_T$ cut. All graphs are plotted as functions of the smearing constant c.

8.3 Estimated Cross Section Precision

For the dileptonic channel the same errors are considered as for the semileptonic decays in Section 6.6, namely the statistical precision due to the integrated luminosity, the systematic errors due to
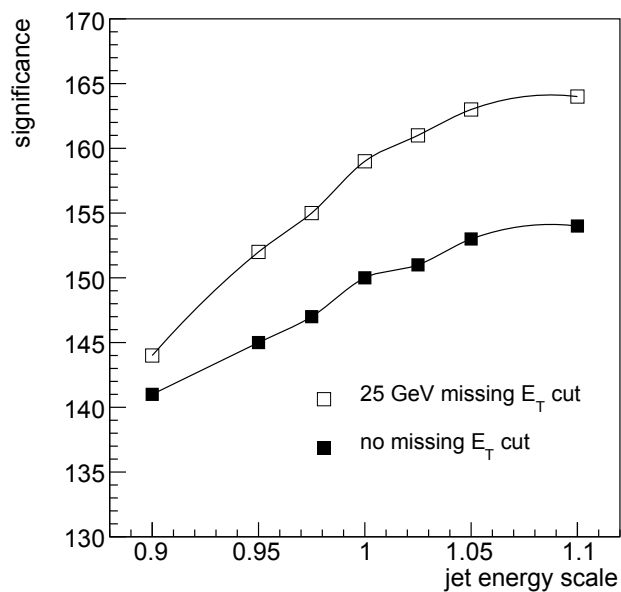
Figure 8.4: The impact of the jet energy scale factor on the significance of the complete analysis selection and a selection without the cut on $\not{E}_T$. As before the values are calculated for a constant fake electron probability of 10^{-3} and $10\,\text{fb}^{-1}$ integrated luminosity.

Scale Uncertainty	±2.5%	±5%	±10%
Error Contribution with $\not{E}_T$ Cut	2.5%	4.4%	9.4%
Error Contribution without $\not{E}_T$ Cut	2.0%	3.3%	6.0%

Table 8.1: Translation of the relative jet energy scale uncertainty to the relative uncertainty of the selection significance. The absolute uncertainty on the values is about 0.6%.

Sample	With $\not{E}_T$ Cut	Without $\not{E}_T$ Cut
other t$\bar{\text{t}}$	0.46 pb	0.41 pb
dibosons	0.04 pb	0.03 pb
W+jets fake	0.03 pb	0.02 pb
W+jets	0.58 pb	0.52 pb
Z+jets	0.67 pb	1.18 pb
$(\Delta\sigma)_{\text{MC,b}}$	1.00 pb	1.36 pb

Table 8.2: Contributions to the total systematic uncertainty of the cross section due to the impact of the limited statistics of the Monte Carlo samples on the background selection efficiencies.

Sample	With $\not{E}_T$ Cut	Without $\not{E}_T$ Cut
other t$\bar{\text{t}}$	0.64 pb	0.65 pb
diboson	0.02 pb	0.02 pb
W+jets fake	0.03 pb	0.04 pb
W+jets	0.06 pb	0.05 pb
Z+jets	0.67 pb	2.01 pb
$(\Delta\sigma)_{\text{CS}}$	1.4 pb	2.8 pb

Table 8.3: Contributions to the total systematic uncertainty of the cross section due to the individual background samples.

the finite Monte Carlo statistics, the cross section uncertainties, and the jet energy scale plus the uncertainty of the luminosity. To avoid repetition the formulas for the error calculation (equations 6.10 ff.) are not given here again.

For an integrated luminosity of $10\,\text{fb}^{-1}$, corresponding to the first nominal year of ATLAS, the statistical error on the cross section, which is expected to be 38.3 pb, amounts to $(\Delta\sigma)_{\text{stat}} = 0.24\,\text{pb}$ for the complete analysis and $(\Delta\sigma)_{\text{stat}} = 0.26\,\text{pb}$ without the $\not{E}_T$ cut.

The systematic errors originating from the finite statistics of the available Monte Carlo samples for the analysis including the $\not{E}_T$ cut are $(\Delta\sigma)_{\text{MC,s}} = 0.77\,\text{pb}$ for the signal and $(\Delta\sigma)_{\text{MC,b}} = 1.00\,\text{pb}$ for the background samples. The analysis without the final cut on missing transverse energy achieves $(\Delta\sigma)_{\text{MC,s}} = 0.72\,\text{pb}$ and $(\Delta\sigma)_{\text{MC,b}} = 1.36\,\text{pb}$. For the background uncertainties the individual errors of the samples, as given in Table 8.2, have been summed quadratically.

For the background cross section again an uncertainty of 10% has been assumed as estimated for the Z+jets and W+jets samples in reference [54]. As for the background in the semileptonic channel the individual fractions, listed in Table 8.3, are added linearly due to possible positive correlations caused by the parton density functions, to attain a conservative estimate. For the complete analysis the result is $(\Delta\sigma)_{\text{CS}} = 1.4\,\text{pb}$ and $(\Delta\sigma)_{\text{CS}} = 2.8\,\text{pb}$ in case $\not{E}_T$ is not reliable at the beginning of the ATLAS data taking.

The errors on the significance due to the expected jet energy scale uncertainty of 5% for the first nominal year propagate into $\Delta S_{\text{JES}} = 1.7\,\text{pb}$ when cutting on missing transverse energy and $\Delta S_{\text{JES}} = 1.3\,\text{pb}$ otherwise. And finally the expected 5% accuracy for the luminosity measurement gives rise to an error of $(\Delta\sigma)_{\text{lumi}} = 2.6\,\text{pb}$ for the total selection and $(\Delta\sigma)_{\text{lumi}} = 3.3\,\text{pb}$ when dropping the $\not{E}_T$ cut.

Error	With E_T Cut	Without E_T Cut
$(\Delta\sigma)_{\text{stat}}$	0.24 pb	0.26 pb
$(\Delta\sigma)_{\text{MC,s}}$	0.77 pb	0.72 pb
$(\Delta\sigma)_{\text{MC,b}}$	1.00 pb	1.36 pb
$(\Delta\sigma)_{\text{CS}}$	1.4 pb	2.8 pb
$(\Delta\sigma)_{\text{JES}}$	1.7 pb	1.3 pb
$(\Delta\sigma)_{\text{lumi}}$	2.6 pb	3.3 pb

Table 8.4: Summary of the statistical and systematic errors for the analysis with and without the cut on missing transverse energy for an integrated luminosity of $10\,\text{fb}^{-1}$ and a fake electron rate of 10^{-3}.

Table 8.4 presents an overview of the individual error contributions. Quadratic addition of the systematic errors yields

$$\Delta\sigma = \pm 0.2(\text{stat}) \pm 2.5(\text{syst}) \pm 2.6(\text{lumi})\,\text{pb} \tag{8.2}$$

for the complete analysis and

$$\Delta\sigma = \pm 0.3(\text{stat}) \pm 3.4(\text{syst}) \pm 3.3(\text{lumi})\,\text{pb} \tag{8.3}$$

for the analysis without the cut on E_T. For a cross section of 38.3 pb this translates into relative precisions of 9.5% and 12.4%. In contrast to the semileptonic channel the contributions from the background cross section and the luminosity no longer dominate. The errors due to the Monte Carlo statistics can be reduced with the production of larger Monte Carlo samples and also the precision of the jet energy scale should improve after real data are analysed, e.g. in connection with a kinematic fit in the semileptonic channel. Also the knowledge of the Z+jets background should improve soon after the first data arrive. Figure 8.5 shows the decrease of the statistical uncertainty as a function of the integrated luminosity. For a scenario where the systematic errors are of the same order as those estimated here the analysis does not benefit from higher statistics after $40\,\text{pb}^{-1}$ integrated luminosity. For a more advanced scenario with systematic uncertainties of 5% the statistical error becomes insignificant after a little less than $200\,\text{pb}^{-1}$, and to benefit from the statistics of the complete first nominal year of ATLAS, corresponding to $10\,\text{fb}^{-1}$ integrated luminosity, the combined error due to systematics and luminosity had to drop below 1% for the selection presented in this thesis.

8.4 B-Tagging Prospects

Parallel to the improvement possible in the semileptonic analysis, as soon as the tagging of b-jets works reliably one might expect a similar increase in significance for the dileptonic selection. Figure 8.6 pictures the number of b-jets per event after all standard analysis cuts at a tagging probability of 60%. In particular the dominant Z+jets background peaks at zero identified b-jets whereas the signal normally has one. However, a cut demanding one or more b-tags does not improve the selection significance but instead reduces it from 159 to 152 for $10\,\text{fb}^{-1}$ integrated luminosity. Nevertheless, b-tagging might become interesting if available before the missing transverse energy measurement is well understood or if the systematics for the cut on the number of b-jets are more
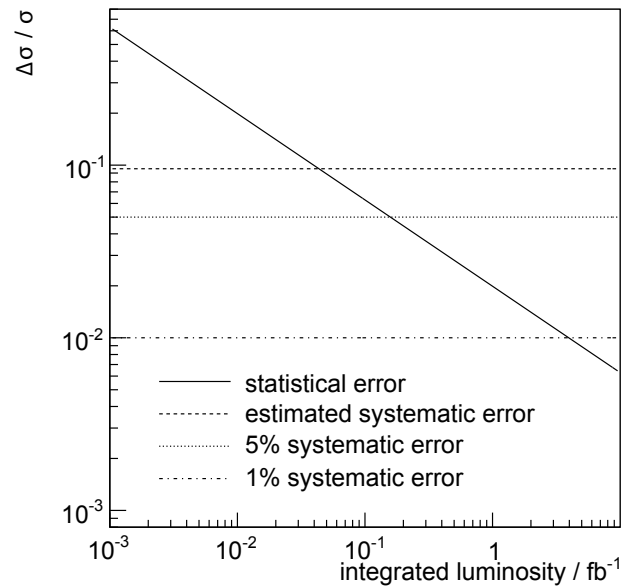
Figure 8.5: Evolution of the statistical error and three scenarios for the systematic uncertainty, including the luminosity error. In any case the precision will be dominated by systematic errors within the first nominal month as with $10\,\mathrm{fb}^{-1}$ integrated luminosity the horizontal axis covers about the first nominal year of the LHC.

precise than the background normalisations. In such cases one might want to reject the events without identified b-jets in spite of the lower significance in exchange for a gain in systematic precision.
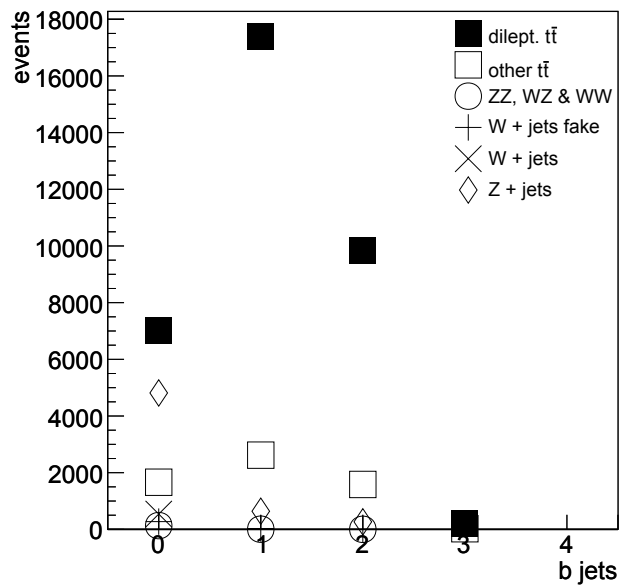
Figure 8.6: The number of identified b-jets per event after the previous analysis selection. The numbers are normalised to $10\,\text{fb}^{-1}$ integrated luminosity. For the W+jets fake background 10^{-3} fake electron probability was assumed.

Part IV

The Cross Section Ratio Measurement

Chapter 9

Decay Ratio Measurement

In this chapter the precision for a measurement of the cross-section ratios for the dileptonic and semileptonic $t\bar{t}$ decay channels is estimated. As a consequence of correlations between both analyses systematic errors partially cancel.

9.1   Advantages of a Cross-Section Ratio Measurement

According to the Standard Model the top quark must decay into a quark, virtually always a b-quark, and a W boson. Indeed, there are scenarios for physics beyond the Standard Model, such as Supersymmetry, where for certain parameters alternative decays are possible. Supersymmetry for instance would give rise to a charged Higgs boson, which, if lighter than the top quark, could induce alternative top decays like $t \rightarrow H^{\pm} + b$. Possible subsequent decays of the charged Higgs are $H^{\pm} \rightarrow cs$, $H^{\pm} \rightarrow \tau\nu$, depending on the Supersymmetry parameters. A direct search for the decay products of a light charged Higgs will be affected by the large number of top background events and be sensitive to background and luminosity uncertainties. Apart from such direct observation, top decays to $H^{\pm}$ should also modify the ratio of the measured cross sections for the dileptonic and semileptonic decay channels as the number of electrons or muons in the final states would be reduced and thus also the ratio.

The ratio measurement is expected to be less prone to systematic uncertainties than individual measurements, as some errors are expected to be strongly correlated between numerator and denominator and will partially cancel. Such uncertainties may be of experimental or theoretical origin.

9.2   Ratio of Semileptonic and Dileptonic Top Pair Decays

In case of the $t\bar{t}$ cross section measurement the ratio $R_{\ell\ell/\ell}$ between the dileptonic and semileptonic channel is expected to amount about $1/6$ or, more precisely, $38.3\,\text{pb}/242.2\,\text{pb}$. At the Tevatron this ratio could be measured with a precision of 22% at D0 [58] and 57% at CDF [59]. The cross-section ratio can be written as

$$R_{\ell\ell/\ell} = \frac{\sigma_{\ell\ell}}{\sigma_{\ell}} = \frac{(N_{\ell\ell} - \varepsilon_{\text{b},\ell\ell}\sigma_{\text{b},\ell\ell}L) \cdot \varepsilon_{\text{s},\ell}}{(N_{\ell} - \varepsilon_{\text{b},\ell}\sigma_{\text{b},\ell}L) \cdot \varepsilon_{\text{s},\ell\ell}} \tag{9.1}$$

The statistical precision for this ratio consists of the statistical errors of the individual cross section analyses[1] according to

$$\left(\frac{\Delta R_{\ell\ell/\ell}}{R_{\ell\ell/\ell}}\right)_{\text{stat}} = \sqrt{\left(\frac{1}{S_{\ell\ell}}\right)^2 + \left(\frac{1}{S_\ell}\right)^2} = \sqrt{\left(\frac{1}{159}\right)^2 + \left(\frac{1}{509}\right)^2} = 0.66\% \tag{9.2}$$

The errors caused by the limited Monte Carlo statistics are also uncorrelated as different samples were used for both analyses except for the $t\bar{t}$ sample. The event selections for both channels do not overlap because exactly one or exactly two good leptons were required, so these events are uncorrelated. Hence for the cross-section ratio the respective relative errors, already combined for signal and background, of 4.0% for the dileptonic and 1.3% for the semileptonic analysis have to be added quadratically, yielding a relative error for the ratio of

$$\left(\frac{\Delta R_{\ell\ell/\ell}}{R_{\ell\ell/\ell}}\right)_{\text{MC}} = \sqrt{(4.0\%)^2 + (1.3\%)^2} = 4.2\% \tag{9.3}$$

The errors from the background cross section uncertainties are assumed to be correlated as the main sources of uncertainty are the PDFs, which contribute to all samples. But also the predictions of pure cross sections may not be independent due to common scales and cut-offs used. A perfect correlation is assumed here, although more detailed studies with systematically altered parton density functions must be done plus a careful inspection of interdependences of the cross section uncertainties.

A simultaneous variation of the products $\varepsilon_{b,\ell\ell}\sigma_{b,\ell\ell}$ and $\varepsilon_{b,\ell}\sigma_{b,\ell}$ in equation 9.1 of $\pm10\%$ as expected for most of the backgrounds gives rise to a relative error due to the cross sections of

$$\left(\frac{\Delta R_{\ell\ell/\ell}}{R_{\ell\ell/\ell}}\right)_{\text{CS}} = 6.0\% \tag{9.4}$$

Errors due to the jet energy scale will also be correlated. Calculation of the ratio in equation 9.1 for the respective values once for +5% variation and once for −5% results in a relative change of the ratio of +0.6% and −2.5%.

The relative error due to the uncertainty on the integrated luminosity according to equation 9.1 is given by

$$\left(\frac{\Delta R_{\ell\ell/\ell}}{R_{\ell\ell/\ell}}\right)_{\text{lumi}} = \frac{\partial R_{\ell\ell/\ell}}{\partial L} \cdot \frac{\Delta L}{R_{\ell\ell/\ell}} = \frac{\varepsilon_{s,\ell}}{\varepsilon_{s,\ell\ell}} \cdot \frac{N_{\ell\ell}\varepsilon_{b,\ell}\sigma_{b,\ell} - N_\ell\varepsilon_{b,\ell\ell}\sigma_{b,\ell\ell}}{(N_\ell - \varepsilon_{b,\ell}\sigma_{b,\ell}L)^2} \cdot \frac{\Delta L}{R_{\ell\ell/\ell}} \tag{9.5}$$

With the numbers obtained for the individual channels this results in a relative error on the ratio of

$$\left(\frac{\Delta R_{\ell\ell/\ell}}{R_{\ell\ell/\ell}}\right)_{\text{lumi}} = 3.1\% \tag{9.6}$$

which is less than the 7–10% relative precision due to the luminosity for the individual measurements.

Table 9.1 summarises the individual error contributions. The quadratic addition yields a precision for the ratio after the first nominal year ($10\,\text{fb}^{-1}$) of

---

[1]Only the complete analyses with the $\rlap{/}{E}_T$ cuts are considered here.

| Error	Contribution
$(\Delta\sigma)_{\text{stat}}$	0.66%
$(\Delta\sigma)_{\text{MC}}$	4.2%
$(\Delta\sigma)_{\text{CS}}$	6.0%
$(\Delta\sigma)_{\text{JES}}$	2.5%
$(\Delta\sigma)_{\text{lumi}}$	3.1%

Table 9.1: Summary of the relative errors, both statistical and and systematic, for an integrated luminosity of $10\,\text{fb}^{-1}$ and a fake electron rate of 10^{-3}.

$$\left(\frac{\Delta R_{\ell\ell/\ell}}{R_{\ell\ell/\ell}}\right) = 0.7\%(\text{stat}) \pm 7.7\%(\text{sys}) \pm 3.1\%(\text{lumi}) \tag{9.7}$$

or 8.4% in total, which is better than the relative errors on the individual cross sections which were 16.0% for the semileptonic and 9.5% for the dileptonic analysis. The precision of 22% achieved by the $t\bar{t}$ cross-section ratio measurement at D0 will be exceeded. As for the individual $t\bar{t}$ analyses, the precision is mainly limited by the systematic uncertainties on the background cross section. Progress can thus be expected if the background normalisation can be extracted from measured data. If the ratio of signal and background events $R_{\text{S/B}}$ in both channels is known, i.e. the individual cross section can be measured according to

$$\sigma = \frac{R_{\text{S/B}} \cdot N}{\varepsilon_{\text{s}} L} \tag{9.8}$$

and ceases to rely on the theoretical cross sections, the cross-section ratio will benefit from this as the integrated luminosity then cancels completely and the errors on the background cross sections will be replaced by the perhaps better understood uncertainties on the background shapes. Figure 9.1 shows the evolution of the statistical error of the cross-section ratio measurement as a function of the integrated luminosity plus horizontal lines for a systematic error of 8.4% as estimated here as well as scenarios where the systematic uncertainties could be reduced to 5% or even 1%. For the estimate in this thesis even in the ratio the systematic error will dominate for more than $65\,\text{pb}^{-1}$ integrated luminosity. With 5% systematic error, which might be achievable when the background can be normalised to data, $200\,\text{pb}^{-1}$ of data suffice. So in order to benefit from the statistics available after the first nominal year of ATLAS the systematic error must be pushed below 1% for which, according to equation 9.8, a very good understanding of the signal to background ratios and of the signal selection efficiencies will be necessary.
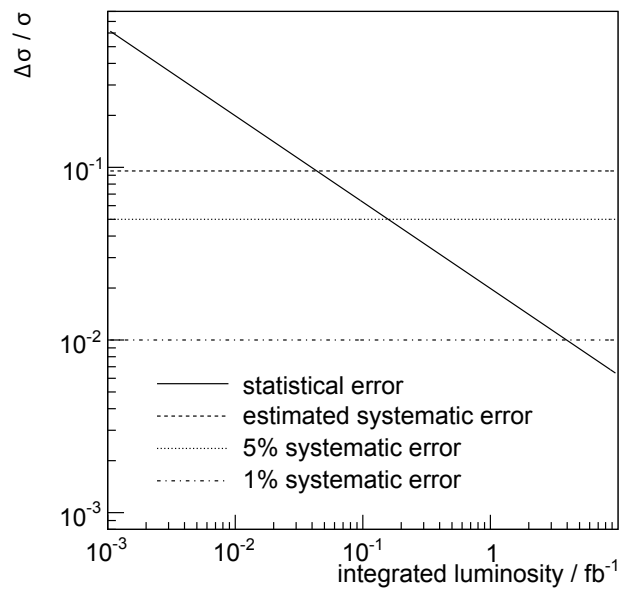
Figure 9.1: Evolution of the statistical error and three scenarios for the systematic uncertainty, including the luminosity error. In any case the precision will be dominated by systematic errors within the first nominal year since the horizontal axis extends to $10\,\mathrm{fb}^{-1}$ integrated luminosity.

Part V

Conclusion

Chapter 10

Summary and Outlook

The Large Hadron Collider at CERN is scheduled to start operation in 2008 and to collide protons with a centre-of-mass energy of 14 TeV. During the first year an instantaneous luminosity of $10^{33}\,\mathrm{cm^{-2}s^{-1}}$ is aimed for. The ATLAS detector is one of the four large experiments at the LHC, designed to precisely measure a broad spectrum of scenarios for new physics as well as Standard Model processes.

With an estimated cross section of 830 pb more than eight million top anti-top pairs are expected to be produced during the first nominal year of LHC and ATLAS, corresponding to an integrated luminosity of $10\,\mathrm{fb^{-1}}$. Hence, the LHC can be considered a "top factory", allowing for measurements of top quark properties with high statistical precision.

In this thesis the precision for a determination of the $t\bar{t}$ cross section using cut based analyses, applicable to the first data, was estimated by relying mainly on Monte Carlo predictions for the expected backgrounds. It was assumed that in this early phase a well understood b-jet identification will not be available. The analysis of the semileptonic decay focused in particular on the study of background from QCD events either with leptons from semileptonic hadron decays or from hadrons falsely identified as leptons by the calorimeter. For the first $10\,\mathrm{fb^{-1}}$ and assuming a fake electron probability of 10^{-3} a precision for the cross section times the branching ratio of

$$\Delta\left(\sigma_{t\bar{t}} \cdot B(t\bar{t} \to b q \bar{q}'\,\bar{b}\ell\bar{\nu})\right) = \pm 0.5(\text{stat}) \pm 30.4(\text{syst}) \pm 24.0(\text{lumi})\,\text{pb}$$

has been estimated, corresponding to a relative precision of 16% for the theoretically predicted cross section times branching ratio of about 240 pb. The analysis in the dileptonic channel achieves a precision of

$$\Delta\left(\sigma_{t\bar{t}} \cdot B(t\bar{t} \to b\bar{\ell}\nu\,\bar{b}\ell\bar{\nu})\right) = \pm 0.2(\text{stat}) \pm 2.5(\text{syst}) \pm 2.6(\text{lumi})\,\text{pb}$$

which translates into a relative error of 10% for the cross section times branching ratio of around 38 pb. The errors for both the semileptonic and the dileptonic channel are expected to improve as progress is made on the luminosity determination and knowledge of the backgrounds is increased by comparisons with measured data.

A measurement of the cross-section ratio between the dileptonic and semileptonic channel is sensitive to scenarios of new phenomena with competitive top quark decay modes such as decays

115

involving a charged Higgs boson. In the last part of this thesis it has been estimated that such a ratio could be measured with a relative precision of

$$\frac{\Delta R_{\ell\ell/\ell}}{R_{\ell\ell/\ell}} = \pm 0.7\%(\text{stat}) \pm 7.7\%(\text{sys}) \pm 3.1\%(\text{lumi})$$

in the first year of ATLAS data-taking. This is an improvement with respect to the precision of 22% achieved by the Tevatron experiments [58], which had several years to increase understanding of their detectors. Even though the systematic errors partially cancel in such a ratio the total uncertainty is still around 8% as long as the background estimates rely on theoretical predictions. This limit on the achievable precision will also improve as soon as the models can be tested against measured data. In addition, further progress can be expected after the b-jet identification is reliable.

At the LHC the measurement of top quark properties will be more than an obligatory exercise as a precise knowledge of top properties, in particular the cross section, is crucial for many searches for physics beyond the Standard Model. Tests of the predictions themselves are important consistency checks and might reveal previously unknown effects. The achievable precision will depend on the understanding of the backgrounds even during the early stages of data-taking. Hence, only measured data can provide substantial progress.

Appendix A

Event Shape Variables Unused in the Semileptonic Analysis

For the semileptonic top pair decay channel a number of variables have been useful for analysis e.g. at the Tevatron [49, 50] or for other studies [60, 61]. However, for the analysis presented in this thesis, which is optimised for best signal significance and includes the QCD background, the following variables could not contribute any further improvements. These variables may contribute eventually in more sophisticated approaches like topological likelihood, optimal observables, or neural networks.

Topological variables as introduced in the following are keys to the event shapes and sensitive to the Lorentz boost of the centre-of-mass frame and thus to the masses of the produced particles in relation to the collision energy. The $t\bar{t}$ spin correlation may also be reflected in the event geometry.
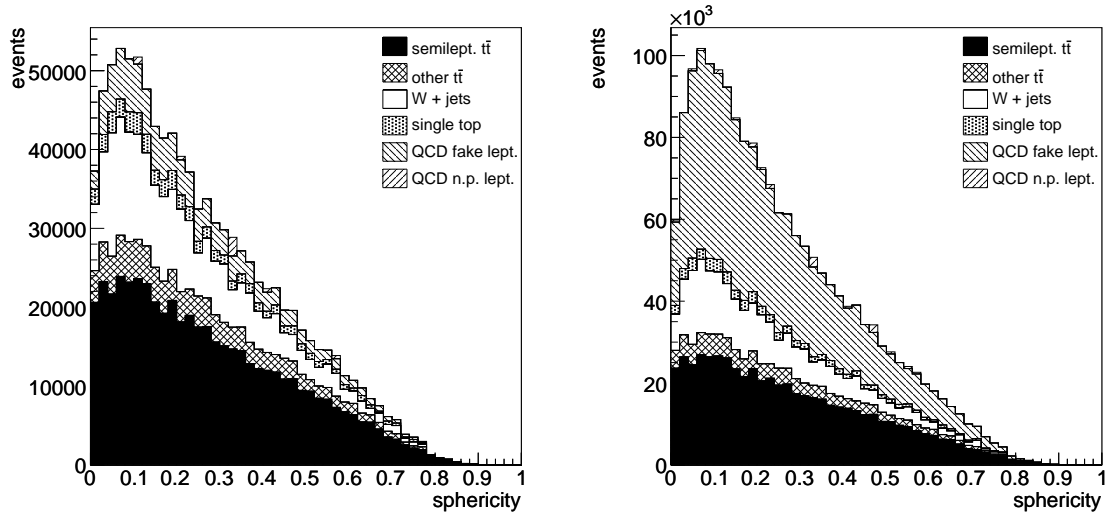
A.1 Sphericity

The sphericity S quantifies the isotropy of a final state in the detector frame. The normalised momentum tensor M is defined as

$$M_{jk} = \frac{\sum_i p_j^i p_k^i}{\sum_i |\vec{p}^{\,i}|^2} \tag{A.1}$$

where $\vec{p}^{\,i}$ is the momentum vector of a reconstructed object and both j and k are Cartesian coordinates. Diagonalising M the three eigenvalues $\lambda_1 \geq \lambda_2 \geq \lambda_3$, with $\lambda_1 + \lambda_2 + \lambda_3 = 1$, are obtained. The sphericity is now defined as

$$S = \frac{3}{2}(\lambda_2 + \lambda_3) \tag{A.2}$$

A perfectly isotropic event yields $1/3$ for all eigenvalues and hence a sphericity of $S = 1$. An ideally planar event would have $\lambda_1 = \lambda_2 = 1/2$ and $\lambda_3 = 0$. In this case the sphericity were $S = 1/2$. In the remaining extreme example, a linear event, λ_2 and λ_3 were zero and also the sphericity. Figure A.1 shows the stacked sphericity distributions for the semileptonic $t\bar{t}$ analysis, once with and

Figure A.1: Stacked sphericity distributions for events after all semileptonic analysis cuts (left) and when omitting the cut on missing transverse energy (right). The plots apply a fake electron probability of 10^{-3} and $10\,\mathrm{fb}^{-1}$ integrated luminosity.

once without the cut on missing transverse energy. In both cases the shapes for the signal and background are too similar to allow for a cut.

A.2 Planarity

The planarity P is also derived from the eigenvalues $\lambda_1 \geq \lambda_2 \geq \lambda_3$ of the normalised momentum tensor M. It is defined by

$$P = \lambda_2 - \lambda_3 \tag{A.3}$$

A completely planar event would have $\lambda_1 = \lambda_2 = 1/2$ and $\lambda_3 = 0$ and hence a planarity of $P = 1/2$. For an isotropic event λ_2 and λ_3 would have the same values and the planarity were $P = 0$. Figure A.2 shows the stacked planarity distributions for the semileptonic t$\bar{\text{t}}$ analysis, again once with and once without the cut on missing transverse energy. As before, the shapes for the signal and background are too similar to enhance top quarks over background events by a simple cut.
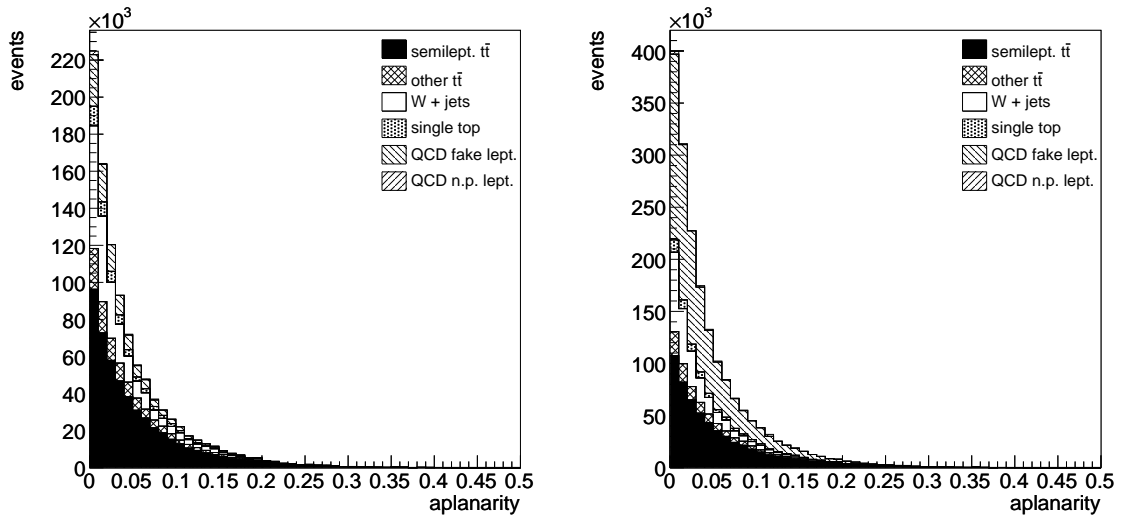
A.3 Aplanarity

The aplanarity A is a further quantity defined from the eigenvalues $\lambda_1 \geq \lambda_2 \geq \lambda_3$ of the normalised momentum tensor M according to

$$A = \frac{3}{2}\lambda_3 \tag{A.4}$$
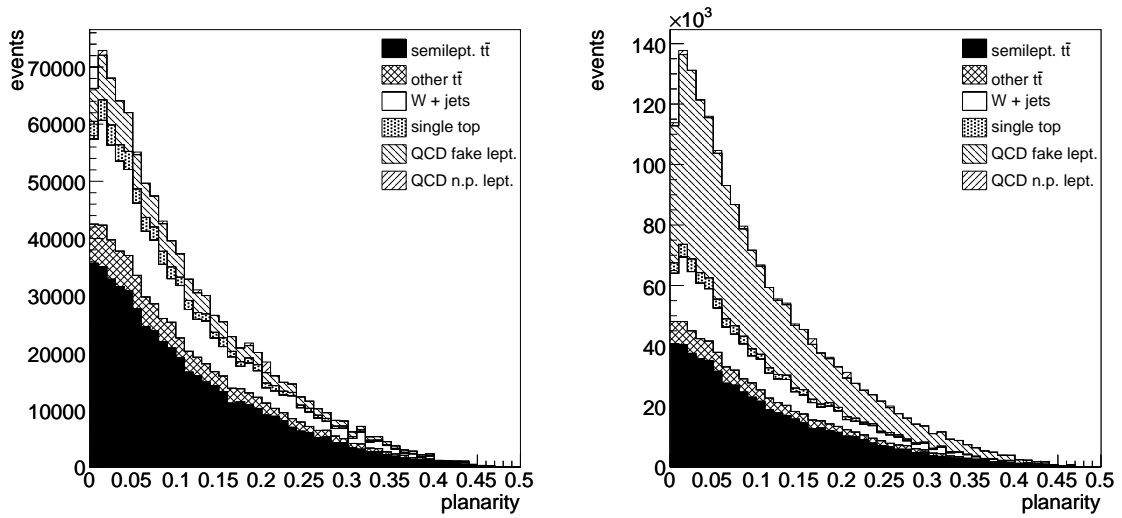
Figure A.2: Stacked planarity distributions for events after all semileptonic analysis cuts (left) and when omitting the cut on missing transverse energy (right). The plots apply a fake electron probability of 10^{-3} and $10\,\text{fb}^{-1}$ integrated luminosity.

As λ_3 cannot be larger than $1/3$ the aplanarity is $A = 1/2$ for an isotropic event. Planar events, including linear ones, yield $A = 0$. In principle the aplanarity does not contribute additional information to sphericity and planarity, as the ratios between the three eigenvectors contain two free parameters only. Nevertheless the aplanarity is useful as it gives a handle on the correlation between the previous two topological variables. Figure A.3 shows the stacked aplanarity distributions, as before once with and once without the cut on missing transverse energy. Again, no improving cut exists.
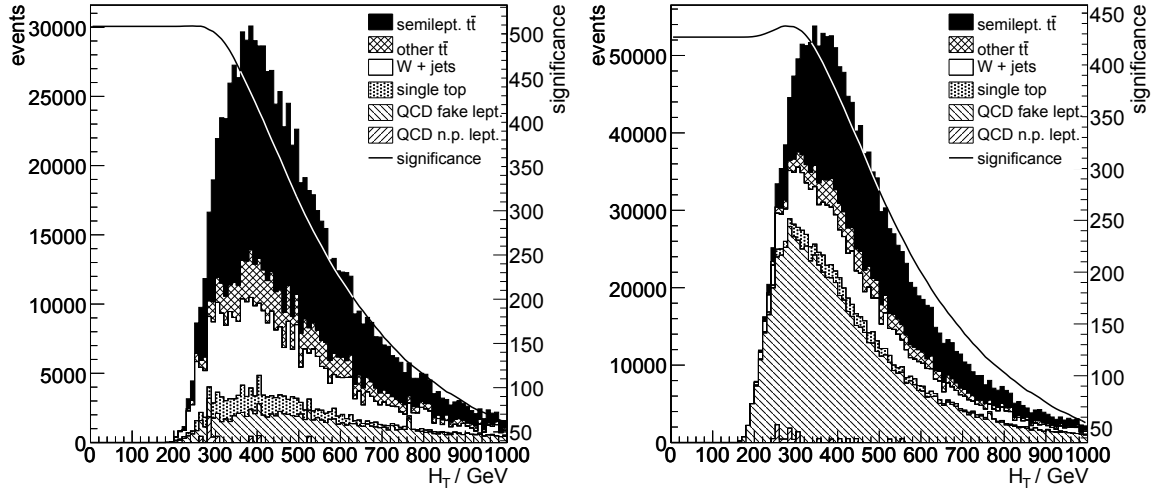

Figure A.3: Stacked aplanarity distributions for events after all semileptonic analysis cuts (left) and when omitting the cut on missing transverse energy (right). The plots apply a fake electron probability of 10^{-3} and $10\,\text{fb}^{-1}$ integrated luminosity.

Figure A.4: Stacked H_T distributions for events after all semileptonic analysis cuts (left) and when omitting the cut on missing transverse energy (right). The plots apply a fake electron probability of 10^{-3} and $10\,\text{fb}^{-1}$ integrated luminosity.

A.4   Scalar Sum of Transverse Momenta

The scalar sum of transverse momenta H_T is a measure for the energy released by the decay of the produced particles. In principle one could calculate this sum from all reconstructed particles but here only the four leading jets are considered as this was done for the analysis in [50]. Figure A.4 shows the stacked H_T distributions obtained, again once with and once without the cut on missing transverse energy. The solid line shows the selection significance when applying a lower cut. In case of the distribution with the complete list of previous analysis cuts applied again no improvement can be seen, except for the case without the cut on missing transverse energy where the selection could slightly be improved by cutting at $H_T = 270\,\text{GeV}$. This would raise the significance from 427 to 438 for a fake electron probability of 10^{-3} and $10\,\text{fb}^{-1}$ integrated luminosity. Even though H_T is not used in the semileptonic analysis the left edge of the distribution might be appropriate to estimate in particular the QCD background from data.

A.5   Centrality

The centrality C is the scalar sum of transverse momenta of the four leading jets normalised to their total energy H, defined as

$$C = \frac{H_T}{H} \tag{A.5}$$

Events with a low Lorentz boost deposit most of their energy in transverse form, yielding a centrality close to 1. From a geometrical point of view $C = 1$ means that the jets lie in the central region of the detector. Strongly boosted events have large longitudinal energy components and thus a low centrality around zero. This variable was quite powerful at the Tevatron where the $t\bar{t}$ system was
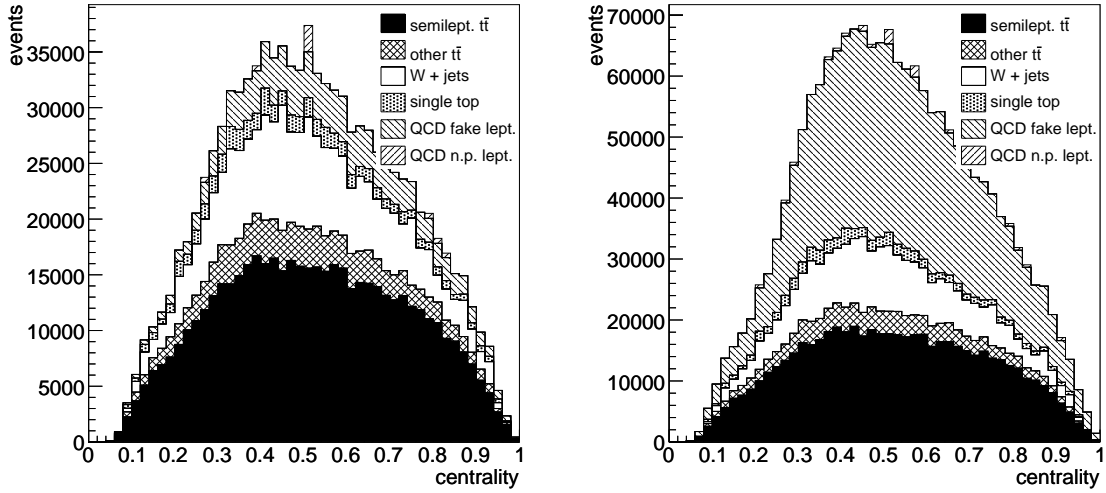
Figure A.5: Stacked centrality distributions for events after all semileptonic analysis cuts (left) and when omitting the cut on missing transverse energy (right). The plots apply a fake electron probability of 10^{-3} and $10\,\text{fb}^{-1}$ integrated luminosity.

produced almost at rest in the detector frame. At the LHC the centrality cannot help to enhance the signal significance, as Figure A.5 reveals: here the signal events are only slightly more central than the background. Nevertheless the distributions should still give some access to the W + jets and QCD from data.
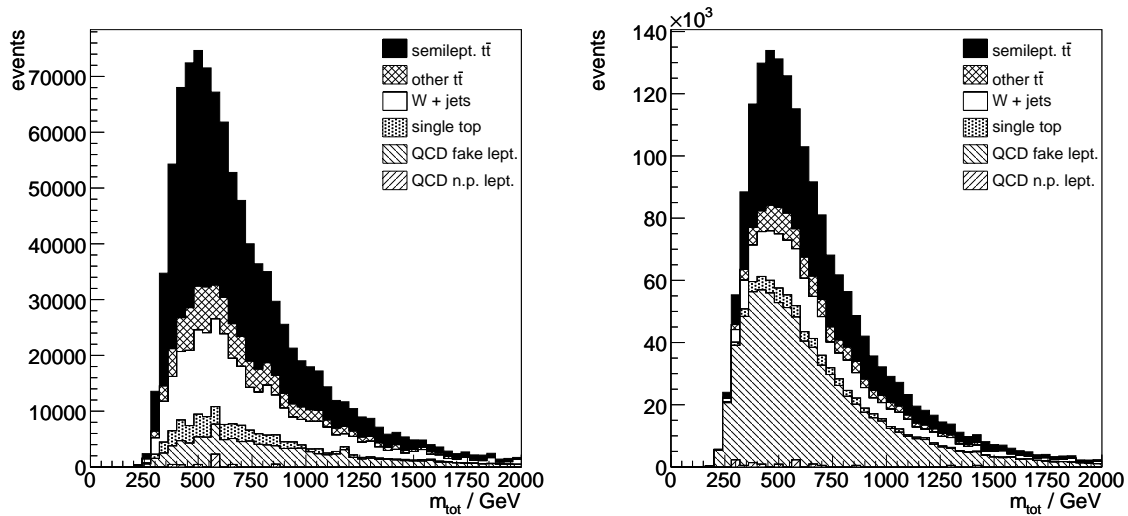
A.6 Total Mass

The total mass of an event is calculated in analogy to the top mass calculation (equation 5.5 in Section 5.5). The four-vectors of all preselected jets, the lepton and the neutrino, are utilised, although the z-component of the neutrino momentum (as reconstructed by equation 5.7 in Section 5.5.2) is neglected in order to avoid a dependence on the transverse missing energy. Figure A.6 shows the distributions obtained from this calculation for the total mass, both with and without a previous cut on $\not{E}_T$. In both cases no cut exists which improves the selection.

A.7 Jet Angles in the Rest Frame

In the centre-of-mass frame of the decay the angles θ^* between the z-axis as defined in Section 3.2.1 and the jet axes might represent variables useful in discriminating between $t\bar{t}$ signal and background events [60, 61]. To calculate these angles the measured jet 4-vectors have to be corrected for the Lorentz boost of the transition from the centre-of-mass frame (primed components) to the detector frame according to

$$\begin{pmatrix} E' \\ p'_z \end{pmatrix} = \begin{pmatrix} \gamma & -\gamma\beta \\ -\gamma\beta & \gamma \end{pmatrix} \begin{pmatrix} E \\ p_z \end{pmatrix} \qquad \text{and} \qquad p'_T = p_T \qquad\qquad \text{(A.6)}$$

Figure A.6: Stacked total mass distributions for events after all semileptonic analysis cuts (left) and when omitting the cut on missing transverse energy (right). The plots apply a fake electron probability of 10^{-3} and $10\,\mathrm{fb}^{-1}$ integrated luminosity.

For this the 4-vectors of all reconstructed objects, summed including the neutrino with its z-component reconstructed as described in Section 5.5.2, are used to reverse the Lorentz boost. The cosines of the angles θ^* obtained for the four leading jets are plotted in Figure A.7. The stacked distributions show a background which rises more strongly for values around $\cos\theta^* = 1$ than the signal. Although the differences do not suffice to improve the selection significance these distributions might be helpful when obtaining the background ratio from real data, especially before a cut on missing transverse energy, see Figure A.8.
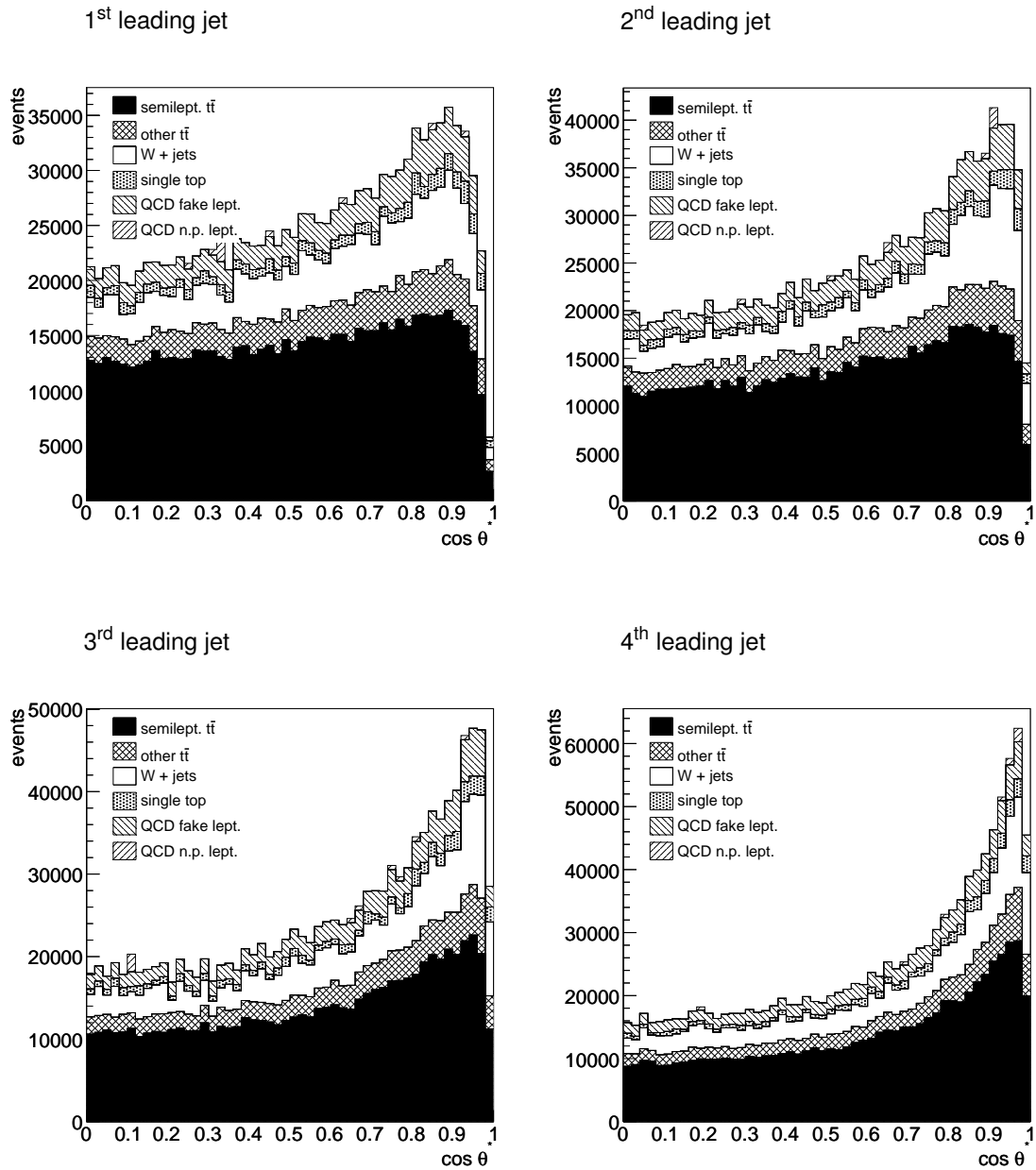
Figure A.7: Stacked distributions of $\cos\theta^*$ for the four leading jets after all semileptonic analysis cuts. The plots apply a fake electron probability of 10^{-3} and $10\,\mathrm{fb}^{-1}$ integrated luminosity.
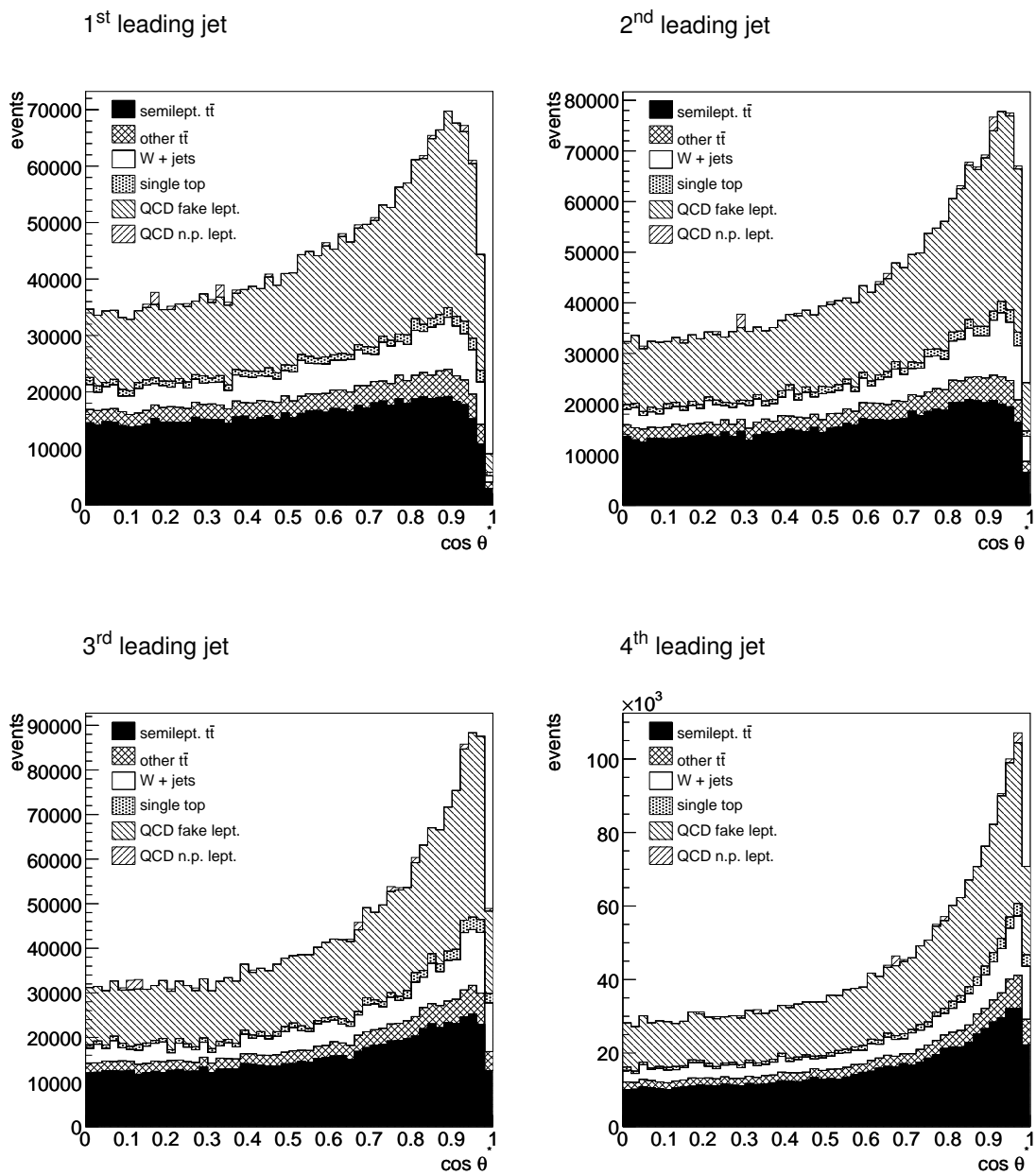
Figure A.8: Stacked distributions of $\cos \theta^*$ for the four leading jets after all semileptonic analysis cuts except the one on $\not{E}_T$. The plots apply a fake electron probability of 10^{-3} and $10\,\mathrm{fb}^{-1}$ integrated luminosity.

Appendix B

Efficiency Calculation

The efficiencies of the sub-samples with positive or negative event weights only, all of absolute value 1, are defined as

$$\varepsilon_+ = \frac{n_+}{N_+} = \frac{n_+}{n_+ + \bar{n}_+} \qquad \text{and} \qquad \varepsilon_- = \frac{n_-}{N_-} = \frac{n_-}{n_- + \bar{n}_-} \tag{B.1}$$

where the numbers of original events N_+ and N_- are composed of the numbers of selected events n_+ and n_- plus the numbers of refused events $\bar{n}_+$ and $\bar{n}_-$. The total efficiency of a sample including both positive and negative weights is

$$\varepsilon = \frac{n_+ - n_-}{N_+ - N_-} = \frac{n_+ - n_-}{n_+ + \bar{n}_+ - n_- - \bar{n}_-} \tag{B.2}$$

According to Gaussian error propagation the uncertainty of the efficiency $\Delta\varepsilon$ is calculated via

$$
\begin{aligned}
(\Delta\varepsilon)^2 &= \left(\frac{\partial\varepsilon}{\partial n_+}\right)^2 (\Delta n_+)^2 + \left(\frac{\partial\varepsilon}{\partial\bar{n}_+}\right)^2 (\Delta\bar{n}_+)^2 + \left(\frac{\partial\varepsilon}{\partial n_-}\right)^2 (\Delta n_-)^2 + \left(\frac{\partial\varepsilon}{\partial\bar{n}_-}\right)^2 (\Delta\bar{n}_-)^2 \\
&= \left(\frac{\bar{n}_+ - \bar{n}_-}{(N_+ - N_-)^2}\right)^2 (\Delta n_+)^2 + \left(\frac{n_+ - n_-}{(N_+ - N_-)^2}\right)^2 (\Delta\bar{n}_+)^2 \\
&\quad + \left(\frac{\bar{n}_+ - \bar{n}_-}{(N_+ - N_-)^2}\right)^2 (\Delta n_-)^2 + \left(\frac{n_+ - n_-}{(N_+ - N_-)^2}\right)^2 (\Delta\bar{n}_-)^2
\end{aligned}
\tag{B.3}
$$

With $(\Delta n_+)^2 = n_+$, $(\Delta\bar{n}_+)^2 = \bar{n}_+$, $(\Delta n_-)^2 = n_-$, $(\Delta\bar{n}_-)^2 = \bar{n}_-$, and the definition of ε_+ and ε_- as in B.1 follows

$$
\begin{aligned}
\Delta\varepsilon &= \frac{1}{(N_+ - N_-)^2} \Big([(1 - \varepsilon_+)N_+ - (1 - \varepsilon_-)N_-]^2 \cdot (\varepsilon_+ N_+ + \varepsilon_- N_-) \\
&\quad + (\varepsilon_+ N_+ - \varepsilon_- N_-)^2 \cdot [(1 - \varepsilon_+)N_+ - (1 - \varepsilon_-)N_-] \Big)^{\frac{1}{2}}
\end{aligned}
\tag{B.4}
$$

As expected for a binomial distribution with positive weights only [1], the case $N_- = 0$ results in the usual equation

$$\Delta\epsilon = \sqrt{\frac{\varepsilon_+(1-\varepsilon_+)}{N_+}} \tag{B.5}$$

Appendix C

Datasets Used from Central Production

In the following all datasets from the central production that are used in this thesis are listed, which are all but the QCD samples. Specified are the ATLAS wide dataset four-digit identification numbers, a short description of the simulated process and the generator(s) used. Given as simulation result is the cross section as calculated by the generator plus a scaling factor to correct for the theoretical/NLO prediction, if available. Furthermore the number of generated events and the normalisation factor needed to scale to $10\,\mathrm{fb}^{-1}$ (in consideration of weights if applicable) and further optional comments are listed, e.g. samples are marked that do not use the standard GEANT4 step width of $30\,\mu\mathrm{m}$ and were corrected later [62].

C.1 Top Pairs

ID	5200
Description	fully and semi-leptonic $t\bar{t}$ decays incl. taus
Generator	MC@NLO + HERWIG
Generated cross section	461 pb
Cross section scaling factor	0.98
Number of events	548 550
Normalisation factor for $10\,\mathrm{fb}^{-1}$	11.3
Comments	175 GeV top mass

C.2 Single Top

ID	5500
Description	single top, Wt-channel, semileptonic
Generator	ACERMC + PYTHIA
Generated cross section	25.5 pb
Cross section scaling factor	1.14
Number of events	15 200
Normalisation factor for $10\,\mathrm{fb}^{-1}$	20.0
Comments	175 GeV top mass

ID	5501
Description	single top, s-channel, leptonic
Generator	ACERMC + PYTHIA
Generated cross section	2.3 pb
Cross section scaling factor	1.5
Number of events	9 750
Normalisation factor for 10 fb^{-1}	5.1
Comments	175 GeV top mass

ID	5502
Description	single top, t-channel, leptonic
Generator	ACERMC + PYTHIA
Generated cross section	81.3 pb
Cross section scaling factor	0.98
Number of events	18 500
Normalisation factor for 10 fb^{-1}	49.0
Comments	175 GeV top mass

C.3   W+Jets (exclusive)

ID	8240
Description	W → eν + 2 partons, 3 jets $p_T > 30$ GeV, 1 lepton
Generator	ALPGEN + HERWIG
Generated cross section	214 pb
Cross section scaling factor	1.15
Number of events	21 950
Normalisation factor for 10 fb^{-1}	112.1
Comments	1 mm GEANT4 fix

ID	8241
Description	W → eν + 3 partons, 3 jets $p_T > 30$ GeV, 1 lepton
Generator	ALPGEN + HERWIG
Generated cross section	124 pb
Cross section scaling factor	1.15
Number of events	11 250
Normalisation factor for 10 fb^{-1}	112.1
Comments	1 mm GEANT4 fix

ID	8242
Description	W $\rightarrow$ eν + 4 partons, 3 jets $p_T > 30$ GeV, 1 lepton
Generator	ALPGEN + HERWIG

Generated cross section	54 pb
Cross section scaling factor	1.15
Number of events	6 000
Normalisation factor for 10 fb^{-1}	102.9
Comments	1 mm GEANT4 fix

ID	8243
Description	W $\rightarrow$ eν + 5 partons, 3 jets $p_T > 30$ GeV, 1 lepton
Generator	ALPGEN + HERWIG

Generated cross section	22 pb
Cross section scaling factor	1.15
Number of events	4 950
Normalisation factor for 10 fb^{-1}	51.9
Comments	1 mm GEANT4 fix

ID	8244
Description	W $\rightarrow$ $\mu\nu$ + 2 partons, 3 jets $p_T > 30$ GeV, 1 lepton
Generator	ALPGEN + HERWIG

Generated cross section	16 pb
Cross section scaling factor	1.15
Number of events	7 000
Normalisation factor for 10 fb^{-1}	26.8
Comments	1 mm GEANT4 fix

ID	8245
Description	W $\rightarrow$ $\mu\nu$ + 3 partons, 3 jets $p_T > 30$ GeV, 1 lepton
Generator	ALPGEN + HERWIG

Generated cross section	65 pb
Cross section scaling factor	1.15
Number of events	12 500
Normalisation factor for 10 fb^{-1}	59.5
Comments	

ID	8246
Description	$W \to \mu\nu$ + 4 partons, 3 jets $p_T > 30$ GeV, 1 lepton
Generator	ALPGEN + HERWIG

Generated cross section	36 pb
Cross section scaling factor	1.15
Number of events	3 200
Normalisation factor for 10 fb^{-1}	129.4
Comments	

ID	8247
Description	$W \to \mu\nu$ + 5 partons, 3 jets $p_T > 30$ GeV, 1 lepton
Generator	ALPGEN + HERWIG

Generated cross section	20 pb
Cross section scaling factor	1.15
Number of events	2 750
Normalisation factor for 10 fb^{-1}	84.4
Comments	

ID	8248
Description	$W \to \tau\nu$ + 2 partons, 3 jets $p_T > 30$ GeV, 1 lepton
Generator	ALPGEN + HERWIG

Generated cross section	88 pb
Cross section scaling factor	1.15
Number of events	19 700
Normalisation factor for 10 fb^{-1}	51.2
Comments	

ID	8249
Description	$W \to \tau\nu$ + 3 partons, 3 jets $p_T > 30$ GeV, 1 lepton
Generator	ALPGEN + HERWIG

Generated cross section	87 pb
Cross section scaling factor	1.15
Number of events	13 000
Normalisation factor for 10 fb^{-1}	77.1
Comments	

ID	8250
Description	W $\rightarrow \tau \nu$ + 5 partons, 3 jets $p_T > 30\,$GeV, 1 lepton
Generator	ALPGEN + HERWIG

Generated cross section	46 pb
Cross section scaling factor	1.15
Number of events	5 750
Normalisation factor for $10\,\text{fb}^{-1}$	91.8
Comments	

ID	8251
Description	W $\rightarrow \tau \nu$ + 5 partons, 3 jets $p_T > 30\,$GeV, 1 lepton
Generator	ALPGEN + HERWIG

Generated cross section	21 pb
Cross section scaling factor	1.15
Number of events	550
Normalisation factor for $10\,\text{fb}^{-1}$	434.9
Comments	1 mm GEANT4 fix

ID	6280
Description	Wbb + 0 partons, 3 jets $p_T > 30\,$GeV, 1 lepton
Generator	ALPGEN + HERWIG

Generated cross section	6.26 pb
Cross section scaling factor	1.15
Number of events	6 250
Normalisation factor for $10\,\text{fb}^{-1}$	11.5
Comments	

ID	6281
Description	Wbb + 1 partons, 3 jets $p_T > 30\,$GeV, 1 lepton
Generator	ALPGEN + HERWIG

Generated cross section	6.97 pb
Cross section scaling factor	1.15
Number of events	7 200
Normalisation factor for $10\,\text{fb}^{-1}$	11.1
Comments	

ID	6282
Description	Wbb + 2 partons, 3 jets $p_T > 30\,\text{GeV}$, 1 lepton
Generator	ALPGEN + HERWIG

Generated cross section	3.92 pb
Cross section scaling factor	1.15
Number of events	4 000
Normalisation factor for $10\,\text{fb}^{-1}$	11.3
Comments	

ID	6283
Description	Wbb + 3 partons, 3 jets $p_T > 30\,\text{GeV}$, 1 lepton
Generator	ALPGEN + HERWIG

Generated cross section	2.77 pb
Cross section scaling factor	1.15
Number of events	3 000
Normalisation factor for $10\,\text{fb}^{-1}$	10.6
Comments	

C.4 W+Jets (inclusive)

ID	5104
Description	$W \to e\nu$, 1 lepton
Generator	PYTHIA

Generated cross section	10 900 pb
Cross section scaling factor	
Number of events	483 750
Normalisation factor for $10\,\text{fb}^{-1}$	225.3
Comments	

ID	5105
Description	$W \to \mu\nu$, 1 lepton
Generator	PYTHIA

Generated cross section	11 946 pb
Cross section scaling factor	
Number of events	214 700
Normalisation factor for $10\,\text{fb}^{-1}$	556.4
Comments	

ID	5106
Description	$W \to \tau \nu$, 1 lepton
Generator	PYTHIA

Generated cross section	3 400 pb
Cross section scaling factor	
Number of events	141 000
Normalisation factor for 10 fb^{-1}	241.1
Comments	

C.5 Z+Jets

ID	5144
Description	$Z \to ee + X$, dilepton mass > 60 GeV
Generator	PYTHIA

Generated cross section	1 675 pb
Cross section scaling factor	1.2
Number of events	481 300
Normalisation factor for 10 fb^{-1}	41.9
Comments	

ID	5145
Description	$Z \to \mu\mu + X$, dilepton mass > 60 GeV
Generator	PYTHIA

Generated cross section	1 675 pb
Cross section scaling factor	1.2
Number of events	185 400
Normalisation factor for 10 fb^{-1}	108.7
Comments	

ID	5146
Description	$Z \to \tau\tau + X$, dilepton mass > 60 GeV
Generator	PYTHIA

Generated cross section	1 639 pb
Cross section scaling factor	1.2
Number of events	176 300
Normalisation factor for 10 fb^{-1}	111.9
Comments	

C.6 Dibosons

ID	5985
Description	WW, 1 lepton
Generator	HERWIG

Generated cross section	24.5 pb
Cross section scaling factor	
Number of events	16 250
Normalisation factor for $10\,\mathrm{fb}^{-1}$	15.1
Comments	1 mm GEANT4 fix

ID	5986
Description	ZZ, 1 lepton
Generator	HERWIG

Generated cross section	2.1 pb
Cross section scaling factor	
Number of events	29 800
Normalisation factor for $10\,\mathrm{fb}^{-1}$	0.7
Comments	1 mm GEANT4 fix

ID	5987
Description	WZ, 1 lepton
Generator	HERWIG

Generated cross section	7.8 pb
Cross section scaling factor	
Number of events	31 150
Normalisation factor for $10\,\mathrm{fb}^{-1}$	2.5
Comments	1 mm GEANT4 fix

Bibliography

[1] W. M. Yao et al. Review of particle physics. *J. Phys.*, G33:1–1232, 2006.

[2] P. W. Higgs. Broken symmetries, massless particles and gauge fields. *Phys. Lett.*, 12:132–133, 1964.

[3] T. Sjostrand, S. Mrenna, and P. Skands. PYTHIA 6.4 physics and manual. *JHEP*, 05:026, 2006, hep-ph/0603175.

[4] G. Marchesini et al. HERWIG: A Monte Carlo event generator for simulating hadron emission reactions with interfering gluons. Version 5.1 - April 1991. *Comput. Phys. Commun.*, 67:465–508, 1992.

[5] G. Altarelli and G. Parisi. Asymptotic freedom in parton language. *Nucl. Phys.*, B126:298, 1977.

[6] J. Pumplin et al. New generation of parton distributions with uncertainties from global QCD analysis. *JHEP*, 07:012, 2002, hep-ph/0201195.

[7] M. A. Dobbs et al. Les Houches guidebook to Monte Carlo generators for hadron collider physics. 2004, hep-ph/0403045.

[8] S. Frixione and B. R. Webber. The MC@NLO 3.3 event generator. 2006, hep-ph/0612272.

[9] M. L. Mangano, M. Moretti, F. Piccinini, R. Pittau, and A. D. Polosa. ALPGEN, a generator for hard multiparton processes in hadronic collisions. *JHEP*, 07:001, 2003, hep-ph/0206293.

[10] S. W. Herb et al. Observation of a dimuon resonance at 9.5-GeV in 400-GeV proton - nucleus collisions. *Phys. Rev. Lett.*, 39:252–255, 1977.

[11] J. R. Ellis and G. L. Fogli. The mass of the top quark from electroweak radiative corrections. *Phys. Lett.*, B213:526, 1988.

[12] F. Abe et al. Observation of top quark production in $\bar{p}p$ collisions. *Phys. Rev. Lett.*, 74:2626–2631, 1995, hep-ex/9503002.

[13] S. Abachi et al. Observation of the top quark. *Phys. Rev. Lett.*, 74:2632–2637, 1995, hep-ex/9503003.

[14] R. Bonciani, S. Catani, M. L. Mangano, and P. Nason. NLL resummation of the heavy-quark hadroproduction cross- section. *Nucl. Phys.*, B529:424–450, 1998, hep-ph/9801375.

[15] The Tevatron Electroweak Working Group. Combination of CDF and D0 Results on the Mass of the Top Quark. FERMILAB-TM-2403-E, 2008.

[16] O. Bruning (Ed.) et al. LHC design report. Vol. I: The LHC main ring. CERN-2004-003-V-1.

[17] ATLAS Collaboration. ATLAS: Detector and physics performance technical design report. Volume 1. CERN-LHCC-99-14.

[18] ATLAS Collaboration. The ATLAS experiment at the CERN Large Hadron Collider. `https://twiki.cern.ch/twiki/bin/view/Atlas/AtlasTechnicalPaper`, 2007.

[19] ATLAS Collaboration. ATLAS inner detector: Technical design report. vol. 1. CERN-LHCC-97-16.

[20] A. Airapetian et al. ATLAS calorimeter performance. CERN-LHCC-96-40.

[21] ATLAS Collaboration. ATLAS muon spectrometer: Technical design report. CERN-LHCC-97-22.

[22] ATLAS Collaboration. ATLAS high-level trigger, data acquisition and controls: Technical design report. CERN-LHCC-2003-022.

[23] The Gaudi Collaboration. `http://proj-gaudi.web.cern.ch/`, 2007.

[24] G. Duckeck (ed.) et al. ATLAS computing: Technical design report. CERN-LHCC-2005-022.

[25] S. Agostinelli et al. Geant4: A simulation toolkit. *Nucl. Instrum. Meth.*, A506:250–303, 2003.

[26] K. Cranmer, A. Farbin, and A. Shibata. EventView - The Design Behind an Analysis Framework. *ATLAS Communications*, ATL-COM-SOFT-2007-012, 2007.

[27] A. Shibata. TopView - ATLAS top physics analysis package. *ATLAS Public Note*, ATL-SOFT-PUB-2007-002, 2007.

[28] R. Brun and F. Rademakers. ROOT - An Object Oriented Data Analysis Framework. Proceedings AIHENP'96 Workshop, Lausanne, Sep. 1996, Nucl. Inst. and Meth. in Phys. Res. A 389 (1997) 81-86. See also `http://root.cern.ch/`.

[29] S. Dean and P. Sherwood. ATLFAST - the ATLAS Fast Simulation Package. `http://www.hep.ucl.ac.uk/atlas/atlfast/`, 2007.

[30] F. Derue et al. Electron Reconstruction. `https://twiki.cern.ch/twiki/bin/view/Atlas/ElectronReconstruction`, 2007.

[31] J.F. Laporte and the Saclay muon software group. Combined muon track reconstruction with STACO. `http://atlas-samusog.web.cern.ch/atlas-samusog/muonboy/DocPublishedTexts/phytdr.staco.pdf`, 2007.

[32] D. Levin et al. Muon RecoPedia. `https://twiki.cern.ch/twiki/bin/view/Atlas/MuonRecoPedia`, 2007.

[33] Gerald C. Blazey et al. Run ii Jet Physics: Proceedings of the Run II QCD and Weak Boson Physics Workshop. 2000, hep-ex/0005012.

[34] D. Cavalli et al. Jet Reconstruction in ATLAS. `https://twiki.cern.ch/twiki/bin/view/Atlas/JetS`, 2007.

[35] A. Hamilton et al. EtMiss. `https://twiki.cern.ch/twiki/bin/view/Atlas/EtMiss`, 2007.

[36] F. Derue et al. Photon Reconstruction. `https://twiki.cern.ch/twiki/bin/view/Atlas/PhotonReconstruction`, 2007.

[37] A.-C. LeBihan et al. Identification of hadronic tau decays with ATLAS detector. *ATLAS Communication*, ATL-COM-PHYS-2007-066, 2007.

[38] A. Shibata et al. Object Selection for CSC Physics Analyses. `https://twiki.cern.ch/twiki/bin/view/Atlas/CSCObjectSelection`, 2007.

[39] A. Shibata. Full and Fast Simulation Performance in Top Events. *ATLAS Communication*, ATL-COM-PHYS-2007-061, 2007.

[40] P. Ferrari et al. Top CSC Samples. `https://twiki.cern.ch/twiki/bin/view/Atlas/TopCSC`, 2007.

[41] D. Charlton et al. CSC Note Recommendations. `https://twiki.cern.ch/twiki/bin/view/Atlas/CSCNotesList`, 2007.

[42] Z. Sullivan. Understanding single-top-quark production and jets at hadron colliders. *Phys. Rev. D*, 70(11):114012, Dec 2004.

[43] J. Campbell and F. Tramontano. Next-to-leading order corrections to Wt production and decay. *Nucl. Phys.*, B726:109–130, 2005, hep-ph/0506289.

[44] B. P. Kersevan and E. Richter-Was. The Monte Carlo event generator AcerMC version 2.0 with interfaces to PYTHIA 6.2 and HERWIG 6.5. 2004, hep-ph/0405247.

[45] M. Lambacher, O. Biebel, and F. Fiedler. Generation of QCD multijet background events with ALPGEN version 2.03 and ATLFAST version 11.0.41. *ATLAS Communication*, ATL-PHYS-INT-2007-007, 2007.

[46] F. Fiedler. private communication, 2006.

[47] S. Bentvelsen and M. Cobal. Top studies for the ATLAS Detector Commissioning. *ATLAS Public Note*, ATL-PHYS-PUB-2005-024, 2005.

[48] W. Verkerke and I. van Vulpen. Commissioning ATLAS using top-quark pair production. *ATLAS Communication*, ATL-COM-PHYS-2007-023, 2007.

[49] C. Clement, C. Gerber, G. Otero, M. A. Pleier, E. Shabalina, and J.-R. Vlimant. Measurement of the $t\bar{t}$ production cross-section at $\sqrt{s} = 1.96\,\mathrm{TeV}$ in the electron+jets final state using a topological method. `http://atlas.physics.arizona.edu/~johns/teaching/phys586/s06/xsec_ejets_topo_note.pdf`, 2005.

[50] P. Schieferdecker. *Measurement of the Top Quark Mass at D0 Run II with the Matrix Element Method in the Lepton+Jets Final State*. PhD thesis, Ludwig-Maximilians-Universität, Munich, Germany, 2005.

[51] A. Doxiadis and M. Kayl. Estimating the isolated lepton rate in multi-jet events. *ATLAS Communication*, ATL-COM-PHYS-2008-004, 2008.

[52] E. Barberis et al. The Matrix Method and its Error Calculation. *D0-Note*, 4564, 2004.

[53] R. Ströhmer. private communication, 2007.

[54] M. Schumacher. Updates on MC cross-sections. `http://indico.cern.ch/conferenceDisplay.py?confId=17537`, 2007.

[55] V. M. Abazov et al. Measurement of the $t\bar{t}$ production cross section in $p\bar{p}$ collisions at $\sqrt{s} =$ 1.96 TeV using kinematic characteristics of lepton + jets events. *Phys. Rev.*, D76, 2007.

[56] T. Petersen et al. W and Z samples from Pythia with decays to e, mu, and tau. `https://twiki.cern.ch/twiki/bin/view/Atlas/WZPythiaSample`, 2005.

[57] A. Barr, W. Vandelli, et al. Gauge boson pairs with HERWIG. `https://twiki.cern.ch/twiki/bin/view/Atlas/GaugeBosonPairs`, 2007.

[58] The D0 Collaboration. Measurement of the Cross Section Ratio $\sigma(\mathrm{p\bar{p}} \to \mathrm{t\bar{t}})_{\ell+\mathrm{jets}}/\sigma(\mathrm{p\bar{p}} \to \mathrm{t\bar{t}})_{\ell\ell}$ with the D0 Detector at $\sqrt{s} =$ 1.96 TeV in the Run II Data. 5466-CONF, 2007.

[59] K. Bloom. Top physics: CDF results. FERMILAB-CONF-04-071-E, 2004, hep-ph/0405020.

[60] M. Cobal, S. Leone, and H. Grassmann. Exploiting the single lepton event structure in the search for the top quark. *Nuovo Cim.*, A107:75–84, 1994.

[61] B. Acharya, A. Belhouari, M. Cobal, and M. Horoub. Kinematical selection and systematics of top events. `http://indico.cern.ch/getFile.py/access?contribId=0&resId=1&materialId=slides&confId=13093`, 2007.

[62] A. Shibata et al. 1mm bug and AOD level fix. `https://twiki.cern.ch/twiki/bin/view/Atlas/TopViewAnalysis1mmBug`, 2007.

Acknowledgements

Curriculum Vitae

Raphael Mameghani
LMU Fakultät für Physik
Am Coulombwall 1
85748 Garching
Email: Raphael.Mameghani@physik.uni-muenchen.de

Personal Information

Place of birth	Neuss
Date of birth	1st August 1978
Nationality	German
Parents	Dr. Farhad Mameghani and Jutta Mameghani, née Pfister
Siblings	2 sisters and 3 brothers

Education

1984 – 1988	Gemeinschaftsgrundschule Büttgen, Kaarst
1988 – 1997	Georg-Büchner-Gymnasium, Kaarst
27th May 1997	Abitur (secondary school diploma)
1997 – 2004	Study of physics at the RWTH Aachen
6th October 1999	Vordiplom (intermediate diploma)
2003 – 2004	Diploma thesis at the CMS experiment: Analysis of cosmic muons measured in CMS drift chambers
14th September 2004	Diploma
Since 2004	Doctorate at the Ludwig-Maximilians-Universität München
2004 – 2007	Scholarship by the DFG (German Research Foundation)
September 2005	Maria Laach summer school of particle physics

Working Experience

1999 – 2001	Tutor of practical exercises for students of science and engineering at the RWTH Aachen
2001 – 2004	Tutor for undergraduate students at the RWTH Aachen
2005 – 2006	Tutor for undergraduate students at the LMU München

Memberships

2003 – 2004	CMS collaboration
Since 2004	ATLAS collaboration
Since 2004	Graduiertenkolleg: particle physics at the energy frontier of new phenomena
Since 2005	International Max Planck research school (IMPRS) on elementary particle physics

Compulsory Social Service

1998 – 2004	Technisches Hilfswerk (Agency for Technical Relief), OV Aachen